ISSN 2367-7570

Workshop "Solar Influences on the Magnetosphere, Ionosphere and Atmosphere"

Book of Proceedings

Seventh Workshop

Sunny Beach, Bulgaria, 1-5 June 2015

Organized by:

Space Research and Technologies Institute

Bulgarian Academy of Sciences

Scientific Organizing Committee

Editors: **Katya Georgieva, Boian Kirov, Dimitar Danov**

ISSN 2367-7570

CONTENT

Sun and Solar Activity

I. M. Podgorny, A. I. Podgorny **Solar Cosmic Ray Acceleration and Propagation** 01

A. I. Podgorny, I. M. Podgorny **Solar flare model, MHD simulations and comparison with observations** 07

N.N. Kalinichenko, A.A. Konovalenko1 A.I.Brazhenko, V.V. Solov'ev **CME in the interplanetary medium by observations of IPS at the decameter wavelengths** 15

Aleksander Stanislavsky, Aleksander Konovalenko, Artem Koval, Yaroslav Volvach **CMEs and frequency cut-off of solar bursts** 19

I.N. Bubnov, A.A. Stanislavsky, A.A. Konovalenko, S. Yerin, A.A. Gridin, A.A. Koval **Advances in solar bursts observations by the low-frequency radio telescopes of a new age** 23

Krasimira Yankova **Analysis of the Nonlinear Behavior of the Accretion Flows** 25

Solar Wind-Magnetosphere Interactions

Jacobi Ch, Unglaub C, Schmidtke, G, Pfeifer M, Schafer R, Brunner R, Woods T, Jakowski N. **Delayed response of global TEC to ionization variations seen from combined SolACES-SDO/EVE solar EUV spectra** 29

Feygin F.Z., Malysheva L.M., Kleimenova N.G., Khabazin Yu.G. **Geomagnetic Pc1 Pulsation Behavior Depending on Solar Activity** 33

Crisan Demetrescu, Venera Dobrica, Cristiana Stefan, Razvan Greculeasa **Geophysically Induced Currents, a space weather hazard. Case study - Europe under intense geomagnetic storms of the solar cycle 23** 37

Diana Beşliu-Ionescu, Marilena Mierla, Georgeta Maris Muntean **The Influence of Apr 10, 2001 CME on the Magnetosphere** 41

N.G. Kleimenova **Post-Storm High-Latitude Geomagnetic Pc5 Pulsations and VLF Emissions as a Result of Solar Wind Disturbances** 45

I.V. Despirak, A.A. Lubchich, N.G. Kleimenova **Comparison of substorms during two solar cycles maximum: (1999-2000 and 2012-2013)** 49

V. Guineva, I.V. Despirak, B.V. Kozelov **Substorms observations during two strongly disturbed periods - in March 2012 and March 2015** 53

CONTENT

Solar Influences on the Lower Atmosphere and Climate

Harry D. Kambezidis, Basil E. Psiloglou, Kosmas A. Kavadias, Athanasios G. Paliatsos, Aristides Bartzokas **Development of a Greek solar map based on solar model estimations** 57

Famil Mustafa, Ali Kilcik, Elchin Babayev, Atila Ozguc **Cosmic Ray Intensity and Solar Activity Variations Possible Effects on the Rainfall in Turkey and Azerbaijan and Caspian Sea Level Changes** 63

Peter Tonev **Estimation of Solar Activity Influence on Vertical Extent of Sprites** 69

Zbyšek Mošna, Petra Koucka Knížová, Kateřina Potužníková **Coherent structures in the Es layer and neutral middle atmosphere** 73

Boris Komitov, Peter Duchlev, Daniela Kirilova, Georgi Byandov, Nadya Kiskinova **Annual Tree Rings Widths and the "Sun-Climate" Relationship** 77

Data Proccessing and Modelling

Koucká Knížová, P., Mošna, Z., Kouba, D., Potužníková, K., Boška, J. **Tropospheric systems influence on the ionospheric plasma** 80

R. Werner, D. Valev, D. Danov, V. Guineva, A. Kirillov **The Atlantic multidecadal oscillation influence on temperatures and on structural changes** 84

Kirillov A.S., Werner R., Guineva V. **Kinetics of electronically excited O_2 molecules in the mixture of CO_2, CO, N_2, O_2 gases** 88

Solar Effects in the Biosphere

S.N. Samsonov, N.G. Kleimenova, P.G. Petrova **Geomagnetic activity influence on the season variations of myocardial infarction in subauroral (Yakutia) and low latitudes (Bulgaria)** 92

Gromozova E., Rudenchik E., Ragulskaya M., Obridko V., Hramova E. **The relative role of space weather factors in Chizhevsky Velkhover effect** 96

Instrumentation for Space Weather Monitoring

Shagimuratov I., Chernouss S., Efishov I., Cherniak I., Zakharenkova I., Tepenitsyna N. **Development of the GPS TEC fluctuations at the high latitude ionosphere during geomagnetic storm** 99

R. Werner, B. Petkov, A. Atanassov, D. Valev, V. Guineva, E. Roumenina, A. Kirillov **GUV 2511 instrument installation in Stara Zagora and first results** 104

Solar Cosmic Ray Acceleration and Propagation

I. M. Podgorny[1], *A. I. Podgorny*[2]

[1] Institute for Astronomy RAS, Moscow, Russia,
[2] Lebedev Physical Institute RAS, Moscow, Russia
E-mail: podgorny@inasan.ru

Abstract.

The GOES data for the flare proton energies of 10 - 100 MeV are analyzed. Proton fluxes ~ 10^{32} acceleration takes at the current sheet decay. Proton acceleration of in a flare occurs along a singular line of the current sheet by the Lorentz electric field, as in the pinch gas discharge. The pulse of protons duration is by 2 - 3 orders of magnitude longer than the duration of flares. The high-energy proton flow from the flares that appear on the Western part of the solar disk arrive to Earth with the time of flight. These particles propagate along magnetic lines of the Archimedes spiral connecting the flare with the Earth. Protons from the flare on the Eastern part of the solar disk begin to register with a delay of more than three hours. Such particles cannot get on the magnetic field line connecting the flare with the Earth. These protons reach the Earth, moving across the interplanetary magnetic field. The particles captured by the magnetic field of the solar wind are transported with solar wind and due to diffusion across the magnetic field. The patterns of solar cosmic rays generation demonstrated in this report are not detected during the small ($\Phi \le 1$ см$^{-2}$ с$^{-1}$ стер$^{-1}$) proton events.

Introduction

About 30% of big flares (class X and even less class M) are accompanied by a flux of relativistic protons. Part of these protons hits the Sun and causes nuclear reactions. The other part of the protons propagates into the interplanetary medium. Despite decades of the effort, the relativistic flare protons remain the least studied manifestation of the flare [1]. The energy of the charged particles in the interplanetary plasma can change only due to the emission or movement along the electric field $Md\mathbf{V}/dt = e\mathbf{E} + e[\mathbf{V}\times\mathbf{B}]/c$. The change of the energy of a particle moving in the field is $dW = eE_r dr$. The electric field may be of different origin: the field of another charged particle (at a collision), space charge field, in particular due to polarization of charges in the plasma, the field induction dB/dt, etc. At the scattering by inhomogeneities of the magnetic field the particle can change the energy only due to motion in the electric field associated with a magnetic field fluctuation. This was clearly articulated in the well known work of Berezhko E. G., and Krymsky G. F. [2]: "Possibility of charged particles acceleration in the plasma in the related electric fields." The change of the energy at scattering by a magnetic fluctuation is determined by the magnitude and spatial scale of the electric field in such fluctuations

Two possibilities of solar cosmic rays generation are discussed in the literature:

a). Proton acceleration in the Lorentz electric field $\mathbf{E}_{rec} = -\mathbf{V}_{rec}\times\mathbf{B}_{cs}/c$ along the singular lines (in particular the line B=0) in the current sheet during magnetic reconnection [3, 4]. Here, $\mathbf{V}_{rec}$ – the velocity of magnetic reconnection, $\mathbf{B}_{cs}$ – the magnetic field of the decaying current sheet. The scheme of proton acceleration in a flare current sheet is shown in fig. 1. The maximum energy of the protons accelerated in the current sheet of a solar flare can be estimated as follows. At a typical velocity of reconnection in a flare is $V_{rec} = 2\times10^7$ cm/s, the magnetic field in the current sheet is $B_{cs} = 100$ G, and the length of the sheet is $L \sim 10^9$ cm the maximum energy of protons accelerated in the current sheet, can be estimated as $W = L\, V_{rec}B_{cs}/c \sim 20$ GeV. This estimation is corresponded to the maximum energy of protons measured at a flare by neutron monitors [5 - 7].

b). Fermi acceleration by the Lorentz electric field $\mathbf{E}_{shock} = -\mathbf{V}_{shock}\times\mathbf{B}_{shock}/c$, in a shock wave, contained the magnetic field. Here, $\mathbf{V}_{shock}$ and $\mathbf{B}_{shock}$ - the velocity and the magnetic field of

the shock wave. The scheme of Fermi acceleration is shown in fig. 2a. Getting to area of a magnetic cloud (shock) that moving towards with the velocity V, the particle moves along a part of the Larmor circle and gains the energy $\delta W = 2\rho Ee$ in the Lorentz electric field. Here, ρ is the Larmor radius. As a result of reflection, the particle velocity increases on $2V_{shock}$. If the particle is captured between two moving to each other magnetic clouds, such particle gains energy at each reflection.

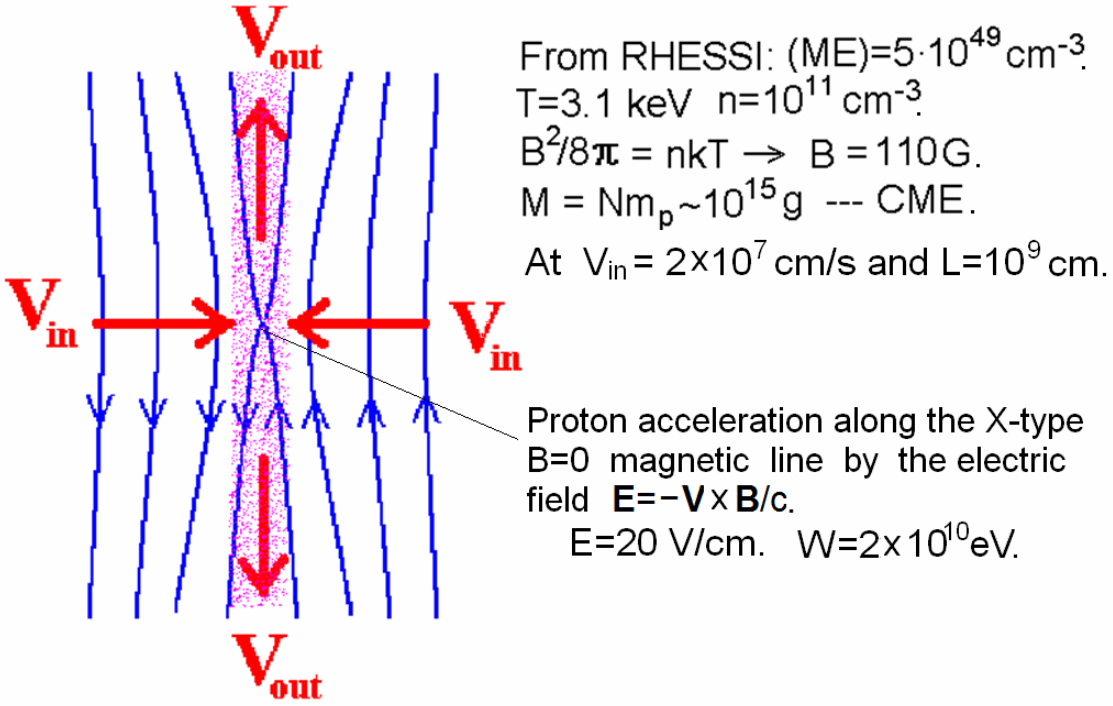

Fig. 1. The plasma velocity vectors and magnetic field lines in the current sheet at reconnection. The electric field -V×B/c is directed perpendicular to the figure plane .

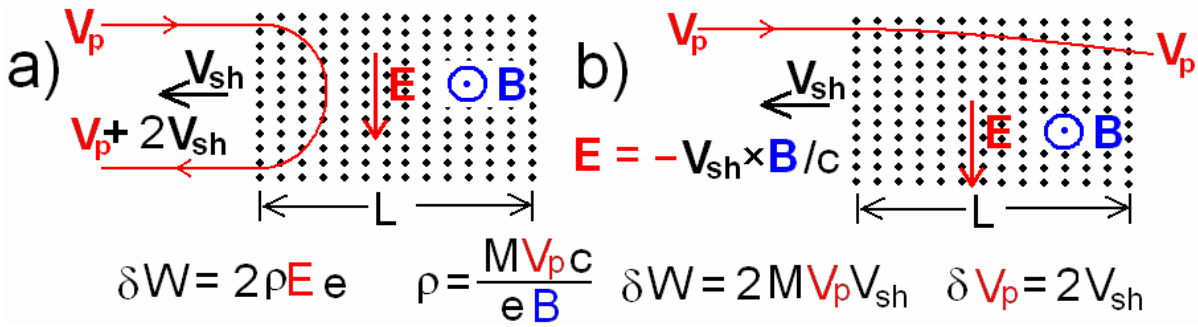

Fig. 2. a). The scheme of the Fermi acceleration of the first type.
b). Drift is impossible for particles, if the Larmor radius has the larger size than magnetic cloud. The particle crosses the shock wave.

The maximum energy attainable at acceleration by the Fermi mechanism corresponds to the condition of equality of the Larmor radius to the size of the magnetic plasma cloud. At higher energy the proton drift in the magnetic field is impossible, and the particle crosses the magnetic cloud. It cannot be accelerated in the field of Lorentz field to the large energy (Fig. 2b). For a typical shock wave in the interplanetary space the magnetic field $B_{shock} = 10^{-4}$ G and the proton energy maximum ~20 GeV, the Larmor radius is $\rho = R/300B \sim 10^{12}$ cm, which is several orders of magnitude higher than the thickness of the observed shock wave. Here R (GV) is the relativistic proton rigidity. Thus, the shock wave in the interplanetary space cannot be a source of the observed relativistic protons after the flare.

According to [2] the proton under certain condition can be captured in the strong magnetic field of a shock wave B_{shock} and gain energy due to the gradient drift, moving along the electric field $E_{shock} = -V_{shock} B_{shock}/c$. The conservation of the proton adiabatic invariant in the shock front is supposed, as shown in Fig. 3, taken from [2]. To explain the acceleration of protons to high energies the authors of [2] consider the possibility of multiple returns of the particles in the acceleration area inside the front due to scattering at magnetic fluctuations. However, such mechanism of proton acceleration also requires the Larmor radius to be smaller than the shock front.

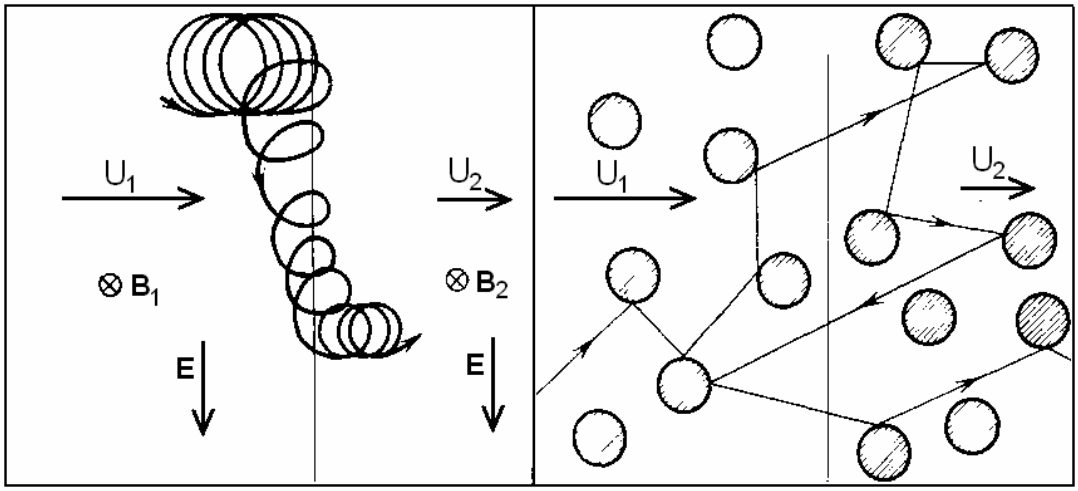

Fig. 3. The drift trajectory of a proton in the shock front. The proton returns inside the front due to scattering on the magnetic field inhomogeneities.

For understanding the mechanism of particle acceleration in a shock front, let us consider the behavior of a particle in the coordinate system associated with the plasma environment in which the particle moves and the shock wave spreads. Two cases are possible:

1. The particle is captured by the front of the shock wave moving in the same direction (Fig. 4a). The particle is decelerated in the Lorentz electric field drifting upward in the area of the magnetic field gradient. The Lorentz electric field is caused by the shock wave movement. The gradient drift is imposed on the drift in the electric field. The resulting drift causes the displacement of the particles along the front. As a result particle acceleration takes place.
2. The particle meets the shock wave front moving to toward (Fig. 4b). The particle is captured in the region of the magnetic field gradient and drifts downward, decelerating in the Lorentz electric field. So, instead of acceleration upon reflection from a magnetic cloud, as shown in figure 2, the gradient drift of the trapped particles leads in such a case to deceleration.

Large fluxes of solar cosmic rays.

Only a part of the X class flares (~30%) and some M class flare accompanied with the great flux $\Phi \geq 1$ cm^{-2} s^{-1} ster^{-1} of relativistic protons are reached the Earth orbit. The spectrum of the proton extends up to 20 GeV [5 - 7]. The average duration of the protons pulse is order of 3 days, while the flare duration, determined from soft and hard x-ray radiation measurements, is order of 20 minutes. The same duration is observed for pulses of γ-radiation (mainly 2.222 MeV) produced by nuclear reactions in the Sun after getting the accelerated protons. That is the duration of the emission of protons is not much different from the flare duration.

Analysis of long-term measurements shows that the parameters of the large relativistic protons flux ($\Phi \geq 1$ cm^{-2} s^{-1} ster^{-1}) reaching the Earth orbit strongly depends on the flare

position on the Solar disk. Typical examples of a single emission of large proton fluxes from the Western and Eastern flares are shown in Fig. 5.

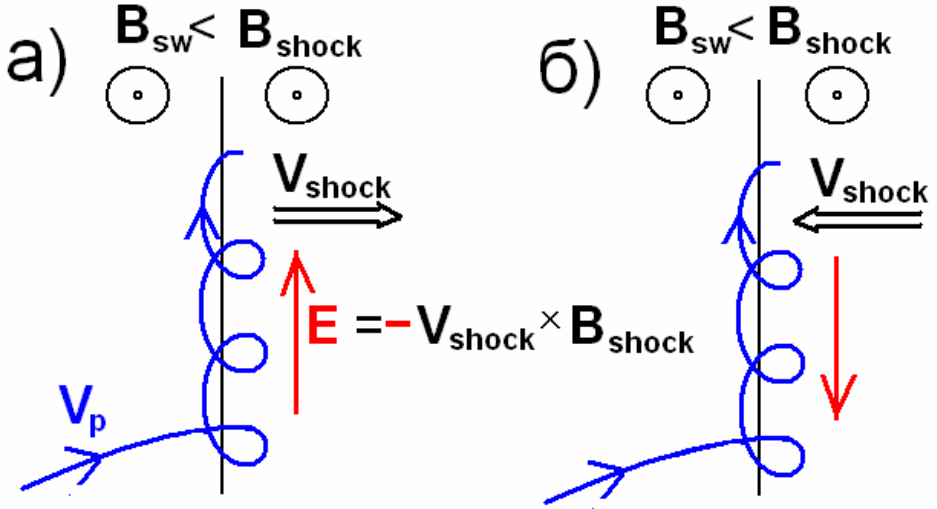

Fig. 4. The trajectory of charged particles entering the shock front. (a) The particle overtakes the shock front. b) The particle moves towards the front.

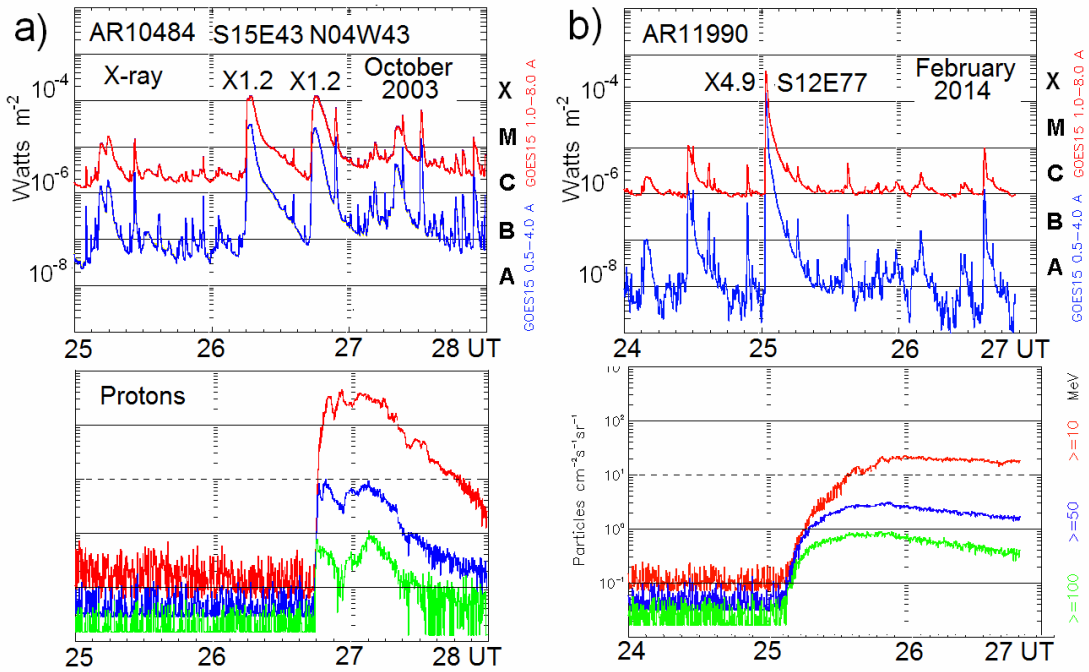

Fig. 5. At the top, a) X-ray emission from the Western proton flare. b) X-ray emission from the Eastern proton flare. Below are the typical large proton fluxes from these flares according to GOES measurements.

The proton flow from a flare that occurred in the West of the Sun has a steep front with duration of about 10 min. The proton flow from this flare comes to the Earth with a delay about 30 min relative to the beginning of the flare. So, the delay is determined by the time of the particle passage from the Sun to the Earth without collisions, apparently along the Arhimed magnetic line. The velocity vector of the particle in the flow front from Western flares is directed, apparently, along magnetic field line. The duration of the proton flow is usually ~3 days. It is equal to the drift time of the protons from the Sun to the Earth with the solar wind velocity (3×10^7 cm/s). At the end of the proton pulse, registered with GOES, particles have arrived that has not been captured by a field line connecting the flare and the Earth. These particles drift across the magnetic field. They propagate in the interplanetary

medium with the solar wind velocity. Some particles can arrive earlier, apparently, propagating a part time along a field line, but the other time they drift across the field. The proton propagation faster than the solar wind could be due to diffusion across the magnetic field at scattering by the magnetic inhomogeneities. In rare cases, the shape of the proton pulse from a Western flare is different from the events shown in Fig. 5a. Sometimes the front of the proton flux is prolonged up to several hours. This happens when the proton flare occurred immediately after other large flares and coronal mass emissions. The helical structure of the interplanetary magnetic field in such a case should be distorted. A unique series consisting of 6 large proton events observed during 10 days from 27.10.2003 on 6.11.2003. Apparently, the interplanetary field was heavily distorted, and the duration the front of the proton flux of the giant Western flare X19 was 10 hours.

Unlike Western proton flares, the protons from Eastern flares and flares that occurred near the central meridian are beginning to register with the delay relative to the beginning of the flare in a few hours. The proton flow front from the Eastern flare is never steep (Fig. 5b). Protons from the Eastern flare are not able to come to the Earth along an Archimed spiral line. They can be transported by the solar wind, and the front can expand by diffusion across the field lines due scattering with the magnetic fluctuations.

Small fluxes of solar cosmic rays.

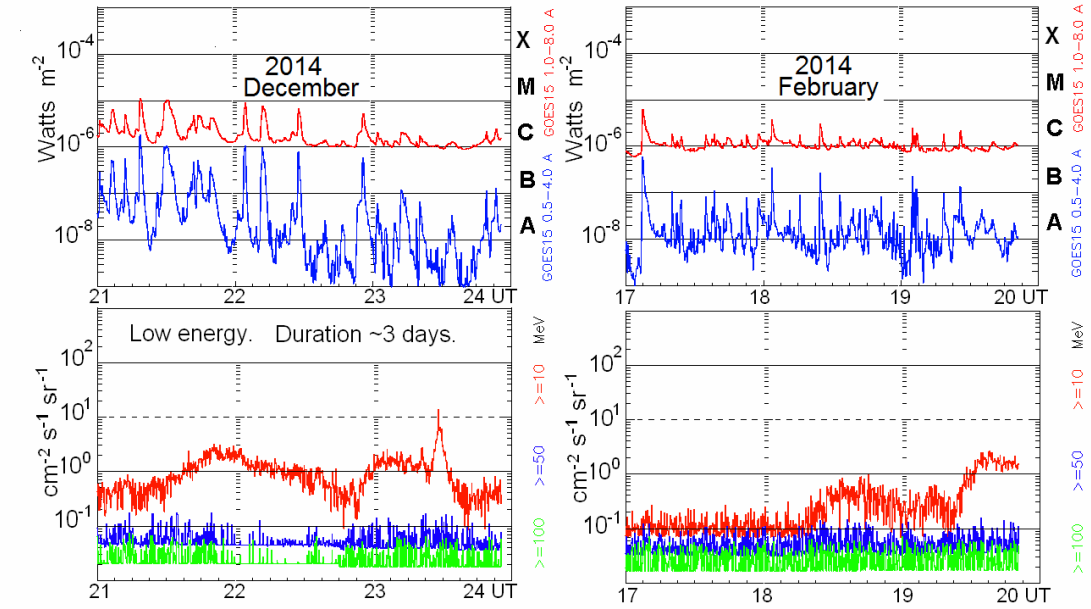

Fig. 6. Above - x-ray emission from flares. Below - a typical small flow of protons according to the GOES measurements.

Small flares ($\Phi \leq 1$ cm^{-2} s^{-1} ster^{-1}) of accelerated protons appear with approximately the same frequency as the large ones ($\Phi \geq 1$ cm^{-2} s^{-1} ster^{-1}). In contrast to the large proton events, the small proton events do not reveal a clear relation to any specific flare. Two examples of small proton events and X-ray pulses of the flares are shown in Fig. 6. Pulses of small proton streams appeared on the background of a number of small flares, mainly of the C class; however, any correlations of proton events with a specific flare are not detected. The duration of small proton events, as the large ones, are observed by days, but their structure is purely individual. No spatial characteristic of small events is observed. The lack of correlation of small proton events with a specific flare observed on the solar disk, apparently, indicates the generation of these events on the back side of the Sun. The protons can arrive along helical magnetic field lines from the night side.

Conclusions.

1. Analysis of the measurement with neutron monitors and GOES suggests that the large proton event is generated by the current sheet during a flare. A clear correlation of small proton events with specific flares is not observed. Apparently, small events are generated by the flares on the back side of the Sun.
2. To accelerate protons in the shock waves it is necessary that the Larmor radius of the particles does not exceed the thickness of the shock front. This condition is impossible in the interplanetary plasma for particles with the energy order of 10 GeV.
3. The proton fluxes of solar cosmic rays reveal four characteristic time scale:
   a). A typical duration of accelerated proton generation is equal to the duration of the flare t_{SF} ~ 20 - 30 min
   b). A typical duration of the accelerated protons flux measured at the Earth orbit is equal to the propagation time of the solar wind t_{SW} = 1a.u./V_{SW} ~ 3 days. This means that the most delayed protons have been captured by the magnetic field of the solar wind and come to the Earth orbit across the magnetic field with the solar wind velocity.
   c). The delay of the steep flux front of relativistic protons generated by the West flare t_F = 15 - 20 min is determined by the time flight of a proton to the Earth orbit along the lines of the Archimedean spiral ~1.5 a.u./c. Collisionless flow of protons along helical magnetic field lines carries information about the spectrum of protons, which according to the neutron monitors data possess the exponential form.
   d). The front of the proton flux from Eastern flares is never being steep. The flux of relativistic protons from the Eastern flare arrives to the Earth with the delay of t_D ~ 3 – 5 hours. The flux increases very slow (~1 day). Such propagation may be associated with the diffusion across the magnetic field lines due to scattering of protons with magnetic inhomogeneities.

Acknowledgments. This work was supported by RFBR grant №13-02-00064.

References

1. Mirishnichenko L.I., Solar Cosmic Rays. *Kluwer. Acad Pabl*., 2001.
2. Berezhko E.G., Krymsky G.F., *Physics-Uspechi.*, **154**, 49 – 90 (1988).
3. Podgorny A.I., Podgorny I.M., *Geomagn. Aeron.*, **52**, 150 – 161 (2012).
4. Podgorny A.I., Podgorny I.M., *Geomagn. Aeron.*, **52**, 162 – 175 (2012).
5. Balabin Yu.V., Vashenuk E.M., Podgorny A.I., Podgorny I.M., *Astron. Reports*, **49**, 837 – 846 (2005).
6. Podgorny I.M., Balabin Yu.V., Vashenuk E.M., Podgorny A.I., *Astron. Reports*, **54**, 645 – 656 (2010).
7. Podgorny I.M., Balabin Yu.V., Podgorny A.I., Vashenyuk E.V., *J. Atm. Solar-Ter. Phys.* **72**, 988 – 991 (2010).

Solar flare model, MHD simulations and comparison with observations

A. I. Podgorny[1], *I. M. Podgorny*[2]

[1] Lebedev Physical Institute RAS, Moscow, Russia,
[2] Institute for Astronomy RAS, Moscow, Russia

Abstract.

The solar flare model is based on the accumulation of magnetic energy in the current sheet, which is formed above an active region. Fast magnetic energy release occurs at the transition of the current sheet in an unstable state. Numerical MHD simulation shows creation of a current sheet in the corona. According to the solar flare electrodynamical model a source of thermal X-ray emission situates in the current sheet. Plasma heating in the sheet occurs due to magnetic energy dissipation. In the numerical simulation no assumptions about the flare mechanism have been done. Due to complexity of the magnetic field, it is necessary to develop the special method of current sheet search in the calculated magnetic field. The method of search is based on the property of the current sheet, according to which the local maximum of the current density is located in the current sheet center. In order to determine whether a given point of the current density maximum corresponds to the current sheet center, the program permits to build the magnetic field configuration. The current sheet is the most clearly presented in the plane, which is perpendicular to magnetic field vector. The search system is used now for study of the solar flares physics. The found current sheet position coincides with the observed position of the X-ray source for the flare 27, 2003 02:53 in the active region NOAA 10365. This coincidence can be considered as a direct indication on the correctness of flare theory based on current sheet creation in the corona.

Introduction. Clarification of the flare mechanism.

It is now established that the solar flare energy is released in the corona above the active regions having a complex distribution of the magnetic field of several kG [1]. Various authors have considered several mechanisms of solar flares production. In [2] is assumed the ejection of the magnetic flux tube with a current (magnetic rope) from the active region, in [3] is examined the possibility of injection of the twisted magnetic field lines (helicity) into the corona and in [4] flare appears due to the sharp change of the current in a magnetic arch above an active region.

All such approaches are based on the assumption of some unstable magnetic configuration existence with the accumulated magnetic energy in the corona or in the chromosphere, which can fast decay heating and accelerating the plasma, and creating beams of high-energy particles. At the same time such approach completely ignores the possibility of the formation of this unstable magnetic system due to observed evolution of the fields and plasma flows in the pre-flare state.

Only the analytical solutions of the MHD equations or the numerical simulation allow us to calculate the magnetic field above an active region and to find out how the energy accumulation for the flare takes place in the corona. To set the initial and boundary conditions it is necessary to use the observed behavior of the active region before the flare. For quick energy release of the accumulated magnetic energy the magnetic configuration must be transferred in an unstable condition and cause flare energy release. The flare mechanism should not be postulates in the numerical experiments, but must be obtained from the results of calculation using real observations in the active region that has produced the flare.

Independently of assumption about the physical mechanism that is responsible for a flare, numerical simulations process should be performed at the initial and boundary conditions taken from the observed state of an active region before a real flare. The flare mechanism should be obtained by simulation results rather than artificially introduced during the setting

of conditions of the numerical simulation. A flare can appear after the magnetic energy ($B^2/8\pi$) accumulation in the magnetic field of a stable configuration, and this energy rapidly dissipates and transfers into the heat and energy of accelerated particles. The process of slow evolution should be replaced by the explosive phase due to instability development.

The criterion of the numerical simulation correctness of pre-flare state of the magnetic field and the plasma above the active region is simple: dissipation of the stored magnetic energy after the development of the instability should provide the main flare manifestations:

1. The energy release over the active region, which is registered by RHESSI measuring the thermal x-ray emission of the dense plasma above an active region.
2. The acceleration of electron beams precipitating on the surface of the Sun, which is registered by the hard x-ray radiation.
3. The creation of the fast plasma flow into the interplanetary space (CME).
4. Generation of relativistic protons.

The modern developed methods for numerical solution of the MHD equations allow determining the magnetic field distribution above the active region before the flare, i.e. to find out what is the configuration of the magnetic field that provides the magnetic energy accumulation for a real flare. The matching thus obtained configuration fields with the results of flare observation, performed by various methods, make it possible to build a model of the flare, without introducing any artificial assumptions about flare nature.

In the present work for the first time we determine the magnetic field configuration before the flare above the active region using only data from the photospheric measurements. No assumptions about the mechanism of energy storage are introduced. It is shown that energy accumulation occurs in the current sheet magnetic field. Current sheet decay in the corona must produce the development of the main processes observed in the flare. The flare development can be described by electrodynamical model of the solar flare.

Methods and conditions of MHD simulation

Simulations [5] show, that to take into account all singularities of magnetic field configuration, it is necessary to perform MHD simulations in the numerical domain which size is several times bigger then the size of active region. The simulations for AR 0365 have been done in domain with the size 4×10^{10} cm. The simulations have been started several days before the series of flares 27 May 2003 produced by AR 0365. In this time the strong disturbances in corona were absent, and the potential magnetic field can be taken for setting the initial conditions. To find potential magnetic field the Laplace equation is solved numerically with oblique derivative boundary conditions on the photosphere. The distributions of the line-of-sight magnetic field component are taken from magnetic maps observed by SOHO MDI (http://soi.stanford.edu/magnetic/index5.html) for setting photospheric boundary conditions. Others boundary conditions are approximated by free-exit conditions.

The simulations are performed by numerical solving of 3D MHD equations above the active region in the solar corona. Its lower boundary is situated on the photosphere and contains the active region AR 0365. The calculations are done in the computational domain ($0\le x\le 1$, $0\le y\le 0.3$, $0\le z\le 1$, in dimensionless units). The unit of the length is chosen as the size of photospheric boundary of the computational domain $L_0=4\times10^{10}$ cm. The Y-axis is directed away from the Sun normally to the photosphere. The XZ (y=0) plane is the photospheric plane. The X-axis is directed from East to West, and the Z-axis is directed from North to South. Situation of photospheric boundary of the computational domain ($y=0$, $0\le x\le 1$, $0\le z\le 1$) in the flare day 27 May 2003 is shown in Figure 1a. The magnetic field $B_0=300$ Gauss is taken as a unit. The dimensionless units of the plasma density ρ_0 and the temperature T_0 are taken to be equal to their values in the initial moment of time in the corona, which are

supposed to be constant in space. $n_0=10^8$ cm^{-3} ($\rho_0=n_0m_i$, m_i is the ion mass), $T_0=10^6$ ^oK. The dimensionless units of the plasma velocity, time, and the current density are taken as correspondingly the Alfven velocity $V_0 = V_A = B_0 / \sqrt{4\pi\rho_0}$, $t_0 = L_0/V_0$, $j_0 = cB_0/4\pi L_0$. The 3D dimensionless MHD equations have the form:

$$\frac{\partial \mathbf{B}}{\partial t} = \mathrm{rot}(\mathbf{V}\times\mathbf{B}) - \frac{1}{\mathrm{Re}_m}\mathrm{rot}\left(\frac{\sigma_0}{\sigma}\mathrm{rot}\mathbf{B}\right) \quad (1)$$

$$\frac{\partial \rho}{\partial t} = -\mathrm{div}(\mathbf{V}\rho) \quad (2)$$

$$\frac{\partial \mathbf{V}}{\partial t} = -(\mathbf{V},\nabla)\mathbf{V} - \frac{\beta_0}{2\rho}\nabla(\rho T) - \frac{1}{\rho}\left(\mathbf{B}\times\mathrm{rot}\mathbf{B}\right) + \frac{1}{\mathrm{Re}\rho}\Delta\mathbf{V} + G_g\mathbf{G} \quad (3)$$

$$\frac{\partial T}{\partial t} = -(\mathbf{V},\nabla)T - (\gamma-1)T\mathrm{div}\mathbf{V} + (\gamma-1)\frac{2\sigma_0}{\mathrm{Re}_m\sigma\beta_0\rho}\left(\mathrm{rot}\mathbf{B}\right)^2 - (\gamma-1)G_q\rho L'(T) +$$

$$+\frac{\gamma-1}{\rho}\mathrm{div}\left(\mathbf{e}_{\parallel}\kappa_{dl}(\mathbf{e}_{\parallel},\nabla T) + \mathbf{e}_{\perp 1}\kappa_{\perp dl}(\mathbf{e}_{\perp 1},\nabla T) + \mathbf{e}_{\perp 2}\kappa_{\perp dl}(\mathbf{e}_{\perp 2},\nabla T)\right) \quad (4)$$

The restrictions connected with the finite step of the difference scheme do not permit to set real dimensionless parameters, which characterize the diffusion terms of equations (1)-(4). The principle of limited simulation [6] is used. According to this principle, the dimensionless parameters, which are much larger then 1 should be chosen larger than 1 in the numerical experiment, but their order of magnitude can be different. In our calculations the parameters are chosen as $\gamma = 5/3$, $\mathrm{Re}_m=1000$, $\mathrm{Re}=300$, $\beta=0.6\times10^{-5}$, $\Pi=100$, $\Pi_B=10^4$, $G_q=0.3\times10^{-5}$. The gravitation force can be neglected comparing with magnetic and plasma pressure forces: $G_g=0$.

To stabilize the numerical instabilities it is used an absolutely implicit finite-difference scheme, which is solved by the iteration method [7]. The scheme is also conservative relative to the magnetic flux. The artificial viscosity is introduced near the computational domain boundary, and some other special methods are used.

The numerical solving of MHD equations is initiated three days before the flare, when there are no strong disturbances and the magnetic field in the active region of the solar corona can be considered as potential one. The potential magnetic field is found by solving of the Laplace equation for the magnetic potential φ_B ($\mathbf{B}= -\nabla\varphi_B$) with the tilted derivative along the line-of-sight as the boundary condition on the photospheric boundary:

$$\Delta\varphi=0; \quad \partial\varphi/\partial l_{sight}|_{PhBoun}=-B_{lsight}; \quad \mathbf{B}=-\nabla\varphi \quad (5)$$

The distribution of the line-of-sight magnetic field component B_{lsight} on the photosphere is taken from magnetic maps obtained by SOHO MDI (http://soi.stanford.edu/magnetic/index5.html). The special methods are developed to obtain the potential field in such approximation to be stable solution of MHD equations system for using finite-difference scheme which is absolutely implicit and conservative relative to magnetic flux. The Laplace equation (5) is solved using a finite-difference scheme on the same grid as for solving MHD equations (1-5). To minimize $|[\mathrm{div}\mathbf{B}]|$ after solving of the Laplace equation for the field potential with tilted derivative as boundary condition (see [5]). It is done two corrections of field. The first of them is solving of the diffusion equation for $\mathbf{B}$ $\frac{\partial \mathbf{B}}{\partial t} = \Delta\mathbf{B}$ with the scheme (1). The second one is inserting magnetic charges in the center of cells of the numerical greed with the value $q=-[\mathrm{div}\mathbf{B}]V_{cell}/4\pi$ (V_{cell} is the cell volume).

For solving the equation (5), it is necessary to set condition on the nonphotospheric boundary. Here the magnetic field is small, and it cannot produce any strong influence on the solution inside the region. The conditions on nonphotospheric boundary are set by two methods. According to the first one, the normal component on the nonphotospheric boundary

$B_{NoPhBoun}$ is set as a constant. $B_{NoPhBoun}$ is calculated from the condition that the full magnetic flux through the boundary of calculation region is equal to zero (the outgoing flux is equal to the flux directed inside the region). For Laplace equation (5) solving the condition $\partial\varphi/\partial n=-B_{NoPhBoun}$ is set on nonphotospheric boundary. According to the second method, the potential φ is set to be zero on the nonphotospheric boundary. The results obtained by the both methods are almost the same.

To solve the system of MHD equations it is need to set two magnetic field components parallel to the boundary on the photospheric boundary of the domain in each moment of time. But SOHO MDI observes on the photosphere only the line-of-sight magnetic field component. For setting boundary conditions, two parallel to the photosphere magnetic field components are taken from calculated potential magnetic field by solving of the equation (5) by the same way as for the initial moment of time. Such method is valid because the magnetic field on the photosphere is defined mainly by the currents under the photosphere, but not by the currents in the corona.

The dimensionless initial conditions for the density, temperature, and velocity take the form:

$$\rho=1;\ T=1;\ V_x=0;\ V_y=0;\ V_z=0$$

The plasma density, velocity, and temperature at the photospheric boundary are specified as follows:

$$\rho=1,\ \partial V_x/\partial n=0,\ \partial V_y/\partial n=0,\ \partial V_z/\partial n=0,\ \partial T/\partial n=0$$

At the other boundaries, these conditions take the form

$$\partial\rho/\partial n=0,\ \partial V_x/\partial n=0,\ \partial V_y/\partial n=0,\ \partial V_z/\partial n=0,\ \partial T/\partial n=0$$

The change of the photospheric magnetic field leads to evolution of the coronal magnetic configuration that simulated by solving MHD equations. In spite of special methods used to stabilize numerical instability it is necessary to have sufficient small time step, otherwise a numerical instability appears. Therefore, the equations are solved slowly, and computations were performed on a time scale shortened by four orders of magnitude in order to accomplish this procedure using the available computer. The calculations performed on a shortened time scale made it possible to understand the general pattern of the magnetic field behavior above an active region and to find the current sheet positions, which appear in the places of X-type singular lines.

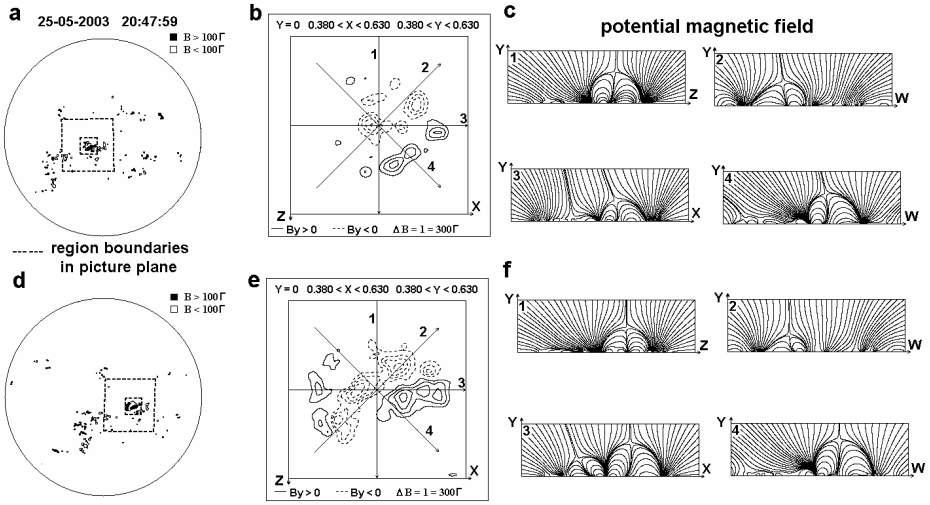

Figure 1. (a, d) SOHO MDI magnetic maps on the solar disk on May 25 and 27, 2003. The positions of the L0=4×1010 and L0=1.2×1010 domains are demonstrated. (b, e) The contour lines of the magnetic field normal component in the active region; (c, f) the configurations of the potential magnetic field in the planes perpendicular to the photosphere; the projections of planes 1–4 are shown in (b) and (e).

Results of MHD simulation in the solar corona above the active region: the current sheet appearance and development

The initial potential magnetic field configuration above the active region AR 10365 is presented in Figure 1 in planes perpendicular to photosphere, which cross the photosphere by lines shown in the Figures 1b, 1e. In each plane the X-type magnetic field configuration is presented, which means that somewhere near it the X-type singular line must be situated. In the vicinity of this X-type singular line the current sheet can be created by focusing of disturbances. The disturbances are propagated from the photosphere. In MHD simulation such disturbances appears due to setting of observed magnetic field, which change in time, on the photosphere boundary.

The Figure 2 demonstrates that numerical MHD simulation shows the current sheet appearance. The left panels present the distribution contours of the magnetic field component, which is normal to the photosphere in the active region; 1–4 show the intersections of the corresponding planes with the photosphere. In each plane perpendicular to the photosphere the magnetic field near to the X-point deforms into configurations, which remind current sheet. The positions of such current sheet configurations are shown by arrows. It does not mean that we see the current sheet in this place of the plane, because the X-type magnetic singular line can be inclined at some angle to this plane. But it means that the current sheet appears in the vicinity of X-type singular line near the place of field deformation in the plane. Our purpose is to find the current sheet and its magnetic field configuration, which is most distinctly pronounced in the plane perpendicular to the singular line.

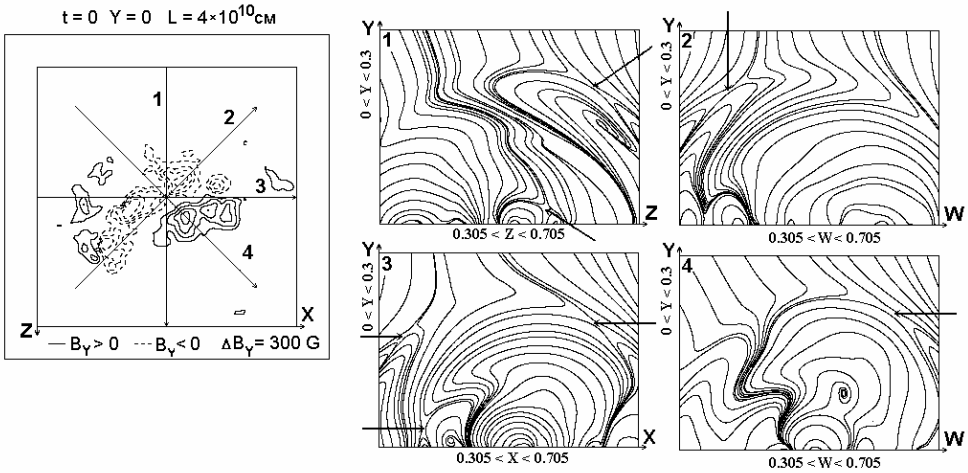

Figure 2. Calculated magnetic field configuration in the corona above AR 10365 before a series of flares in the planes perpendicular to the photosphere. The position of the planes is shown on the left-hand side. The arrows mark the produced current sheets.

A numerical simulation of a current sheet [8, 9] indicated that the plasma density near the sheet decreases during a quasistationary evolution process. The decrease of the plasma density results in an instability and explosive energy release [10, 11].

The calculated magnetic field configurations [5] in the most representative central plane of the region show appearance of several current sheets (see Figure 3). The disturbances that originated on the photosphere propagate upward into the corona. The magnetic field is deformed in the vicinity of the X points (arrows 1 and 2) that existed in the potential magnetic field at the instant t= 0, and current sheets are formed. By the t= 2.2 instant, the current sheets marked by arrows 1 and 2 are formed, and a sheet originates near the photosphere (marked by arrow 3). The field lines of sheets 2and 3are scaled up in the bottom panels. The field configuration corresponds to typical current sheets with the normal component of the magnetic field. As the magnetic field emerges, the current sheets move upward, and the sheet

2 goes beyond the computational domain by instant 3.8. The field lines of this current sheet are located so that it is difficult to detect this sheet in the Z= 0.5 plane.

Figure 4 shows the field lines in the three-dimensional space near the horizontally located sheet marked by arrow 2. These data correspond to the field configuration that originated on May 26, 2003.

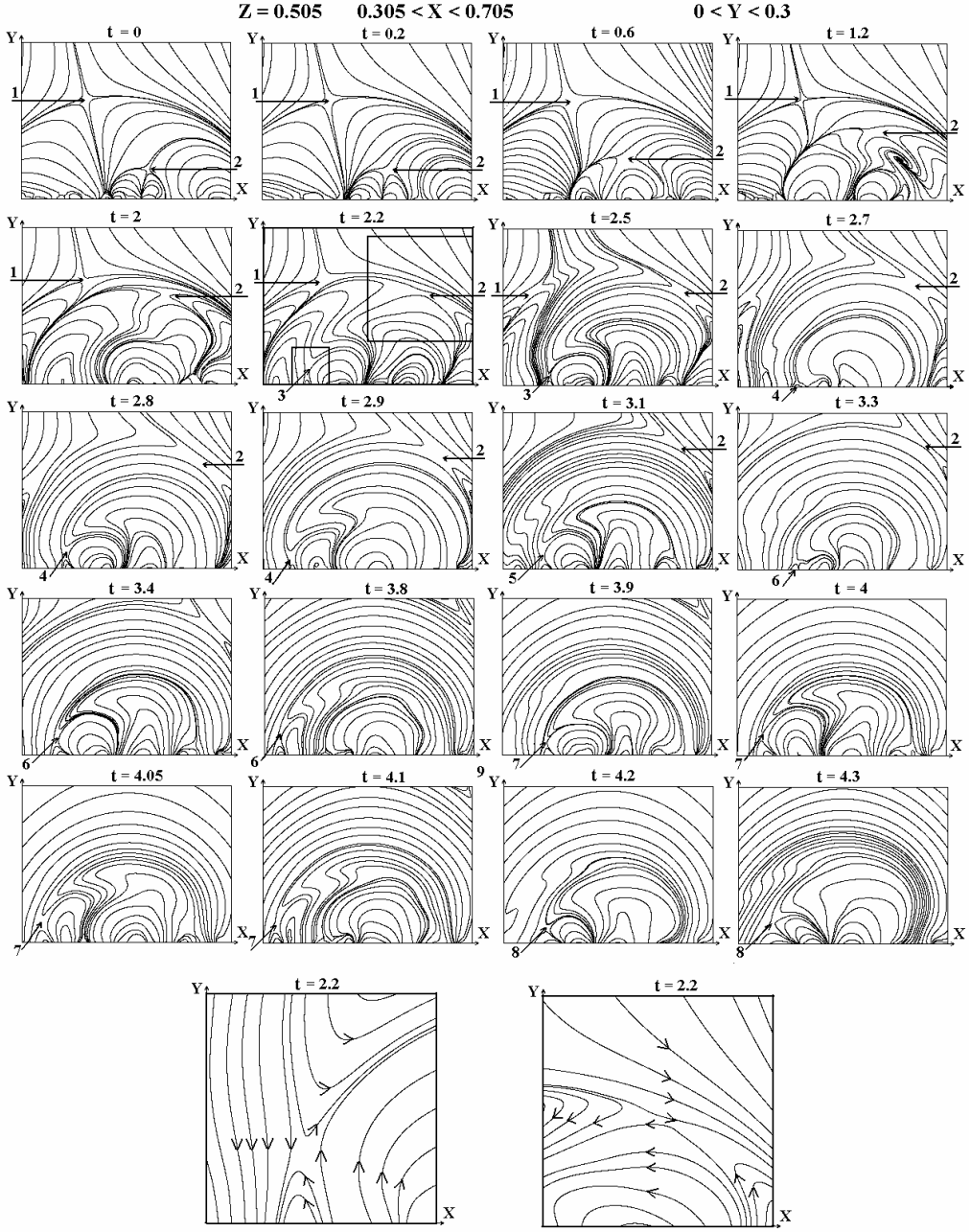

Figure 3. Magnetic field lines in the central plane of computational domain in corona above the active region obtained by MHD simulations. The current sheets are indicated by arrows. Below, the field lines near the two current sheets indicated by arrows 2 and 3 for time t = 2.2 are shown on an expanded scale.

To find positions of sources of soft X-ray radiation in the corona the graphical system developed by authors is used. The current sheet property is used, according to which the local maximum of the absolute value of the current density is located in the center of a current sheet. In any selected plane, which can be placed arbitrarily in the space in the computational domain, the lines of level of absolute values of current density are constructed. Furthermore, in this plane all positions of the local current density maxima in the plane and projections on

the plane of all positions of the local maxima of the current density in the space are marked. Marked points are located at the intersection of the current sheets with the plane, or they are corresponded to current sheets centers. The program can easily obtain information about any marked point of the maximum. It can be outputted coordinate value of that point in any chosen coordinate system and the all calculated values (magnetic field vector, plasma density, and plasma temperature, etc.) in this point. In order to determine whether a given point of the current density maximum corresponds to the current sheet center or simply corresponds to an increase of the current density as a result of some disturbance, the program offers the possibility to build the magnetic field configuration in the vicinity of the selected point in any arbitrarily rotated coordinate system. Typically, in first turn it is expected to build the magnetic field configuration in a plane containing the selected point of the current density maximum which is situated perpendicular to the magnetic field vector. [12].

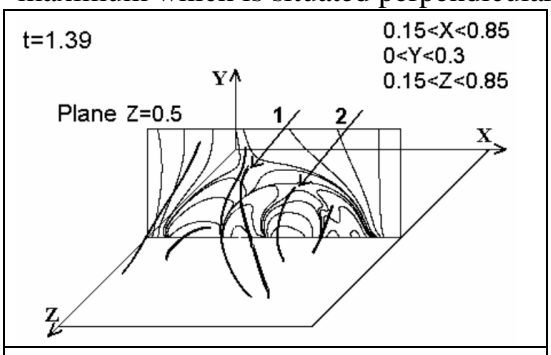

Figure 4. Magnetic field characteristic lines in three dimensional space (thick lines) and on thez= 0.5 plane.

The developed graphical system permits to find of the current sheet position for the flare, which occurred May 27, 2003 at 02:53 above the active region NOAA 10365. The coordinates of the center of the founded current sheet in the computational domain are (0.46, 0.04, 0.445). It situated on the height ~ 16 000 km. Taking into account that on such small height the magnetic field is large, the position of a such current sheet, must correspond to the solar flare place. In the vicinity of this local maximum in the plane, which is perpendicular to the magnetic field vector, the magnetic field configuration corresponds to the pronounced current sheet distinctly (see Figure 5a) The lines of equal current density in this plane and 3D magnetic lines are presented in Figures 5 b, c.

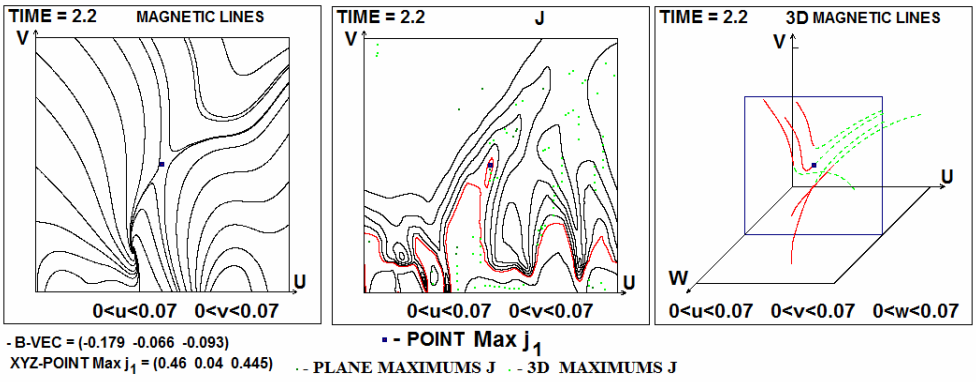

Figure 5. a, b – Magnetic field configuration and lines of equal current density in the plane which contains the point of current density maximum with coordinates (0.445, 0.105, 0.42) and which is situated perpendicular to magnetic field vector B=(0.0086, 0.0264, 0.0819). The 3D magnetic lines are presented in the left panel, behind the plane they are marked as dashed lines.

The current sheet position coincides with the position of the source of thermal X-ray. [13]. This coincidence is independent evidence of the solar flare mechanism, based on the accumulation of the flare energy in the current sheet magnetic field in the corona.

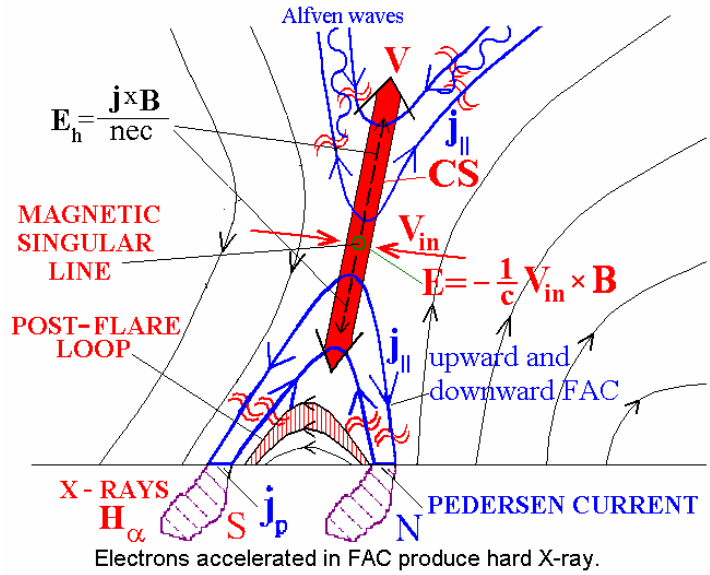

Figure 6. The electrodynamic model of the flare. The magnetic field lines are shown by thin lines and arrows; the field-aligned currents are demonstrated by thick lines and arrows.

Conclusion. Solar flare model

Numerical simulation permits to conclude that energy accumulation for the solar flare takes place in the current sheet magnetic field. Decay of this current sheet should cause the complex of phenomena detected during the flare. The most informative data were obtained in the measurements of X-ray emission on the spacecraft RHESSI. The position of the thermal X-ray emission source coincides with the calculated position of the current sheet. Thus, it can be concluded that the fact of plasma heating by dissipation of the current sheet magnetic field is established. The measurements in the magnetospheric tail and laboratory experiments [14] show generation of the Hall electric field j×B/nec in the current sheet. The Hall field should produce field-aligned currents, in which the electrons must be accelerated and precipitate on the solar surface. The source of hard beam X-ray emission is registered on the solar surface by RHESSI. The numerical simulation [15] shows proton acceleration up to relativistic energies by electric field along the singular line of the current sheet. The **j×B** force should accelerate the plasma along the sheet, and eject it into space (Coronal mass ejection). Matching of these observational data and the fact of current sheet creation before the flare, obtained by numerical simulation, permits us to propose the electrodynamic model of the flare, shown in Figure 6. The model explains release of the magnetic energy accumulated above the active region and the main observational manifestations of the solar flare.

Acknowledgments. This work was supported by RFBR grant №13-02-00064.

References.

1. Podgorny I.M., Podgorny A.I., Meshalkina N.S., *Sun and Geosphere*. **8**, 63 – 69 (2013).
2 Kliem B., Titov V.S., Torok T., *Astron. Astrophys. 413*, L23-L26 2004.
3.Kusano, K., Yokoyama T., Maeshiroi T., Sakurai T., *Adv. Space Res.*, **32**, 1931 – 1936 (2003).
4. Zaitsev V.V., Stepanov A.V., *Progress in Physical Science (Physics Uspekhi)* 178, 1166 – 1197 (2008).
5. Podgorny A.I, Podgorny I.M., *Astronomy Repoprts*. 52, 666 – 675 (2008).
6. Podgorny I.M., *Fund. Cosmic Phys.* **1**, 1 – 72 (1978).
7. Podgorny A. I., Podgorny I. M. *Comput. Mathematics and Mathemat. Physics*. **44**, 1784 – 1806 (2004).
8. Bilenko I.A., Podgorny A.I., Podgorny I.M., *Solar Phys.* **207**, 323 – 336 (2002).
9. Podgorny A.I, Podgorny I.M., *Astronomy Repoprts*. 47, 696 – 702 (2008).
10. Podgorny A.I. *Solar Phys.* **123**, 285 – 308. (1989).
11. Podgorny A.I. *Plasma Physics and Controlled Fusion.* **31**, 1271 – 1279 (1989).
12. Podgorny A.I., Podgorny I.M, Meshalkina N.S., *Solar System Research*. **41**, 322 – 329 (2007).
13 Podgorny A.I., Podgorny I. M., *Sun and Geosphere.* **8**, 71 – 76 (2013).
14 Minami S., Podgorny A.I., Podgorny I.M., *Geophys. Res. Letts.* **20**, 9 – 12 (1993).
15 Podgorny I.M., Balabin Yu,V., Podgorny A.I., Vashenyuk E.V., *J. Atm. Solar-Ter. Phys.* 72, 988 – 991 (2010).

CME in the interplanetary medium by observations of IPS at the decameter wavelengths

N.N. Kalinichenko[1], *A.A. Konovalenko*[1], *A.I.Brazhenko*[2], *V.V. Solov'ev*[1]

[1] Institute of radio astronomy, Kharkiv, Ukraine
[2] Gravimetric observatory, Poltava, Ukraine
E-mail: kalinich@rian.kharkov.ua

INTRODUCTION

We carry out interplanetary scintillation (IPS) observations of cosmic radio sources (Hewish et al. 1964) with using URAN decameter radio telescope system (8 - 32 MHz, Ukraine). During the last few years the registration, control and others systems of the radio telescopes composing URAN system (UTR-2, Grakovo; URAN-1, Zmiyov; URAN-2, Poltava; URAN-3, Lviv; URAN-4, Odesa) were essentially improved. These improvements and the development of the new effective methods for weakening ionospheric and interference effects allow us to raise efficiency of IPS observations and experimental data reliability. Among other these allow us to find and to study large scale moving disturbances in the solar wind associated with coronal mass ejections (CME). In particular, we manage to find and to study the large scale disturbance in the solar wind associated with Valentine's day CME (15 February 2011).

At present time investigations of coronal mass ejections in the interplanetary medium (ICME) with using IPS observations at high frequencies (more or about 100 MHz) are common at the distances from the Sun less than 1 a. u. We manage to observe ICME at the distances from the Sun, which is more than 1 a. u., by observing IPS at decameter wavelengths at solar elongations (angle between the directions to the Sun and the source) more than 90^0. This became possible, as at the decameter wavelengths the cosmic radio sources show good scintillations right up to elongations of about 180^0, at which the high frequencies (more or about 100 MHz) are only slightly scattered by low density plasma at the large distances from the Sun (large solar elongations correspond to large distances from the Sun).

OBSERVATIONS

Valentine's day CME took place in February 15, 2011, about 01:57 UT and was registered by SOHO and Stereo A, B spacecrafts. SOHO, Stereo A, B spacecraft data showed that Valentine's day CME was an Earth-directed, had an initial speed of about 1000 km/s and was expected to reach the Earth on late 17^{th} to early 18^{th} February 2011 (Lee et al. 2013). The angular width of CME was $65–85^o$.

Observations of IPS were synchronously made with the largest in the world decameter radio telescope UTR-2, Grakovo (Braude et al. 1978) and the decameter radio telescope URAN-2, Poltava (Megn et al 2003). Every day, from February 16 to February 22,2011, three radio sources (3C144, 3C196 and 3C273) were observed at elongations of 114^o, 136^o, 143^o, correspondingly. Records were obtained by using digital spectrum analyzers DSP-z (Ryabov et al. 2010) with parameters of registration: the continuous frequency range - 20.63 to 28.88 MHz, the time constant - 20 ms. The use of the digital spectrum analyzers and records from two radio telescopes allows us to apply special methods for weakening ionospheric and interference effects and to achieve sensitivity that is close to maximal. Figures 1 a - d show examples of data recordings for February 17, the day before ICME came to the Earth (Figure 1 a, b) and February 18, the day when ICME crossed Earth's orbit and appeared on the lines of sight to the observed radio sources (Figure 1 c, d). The difference in scintillation levels for these two days is visible to the unaided eye.

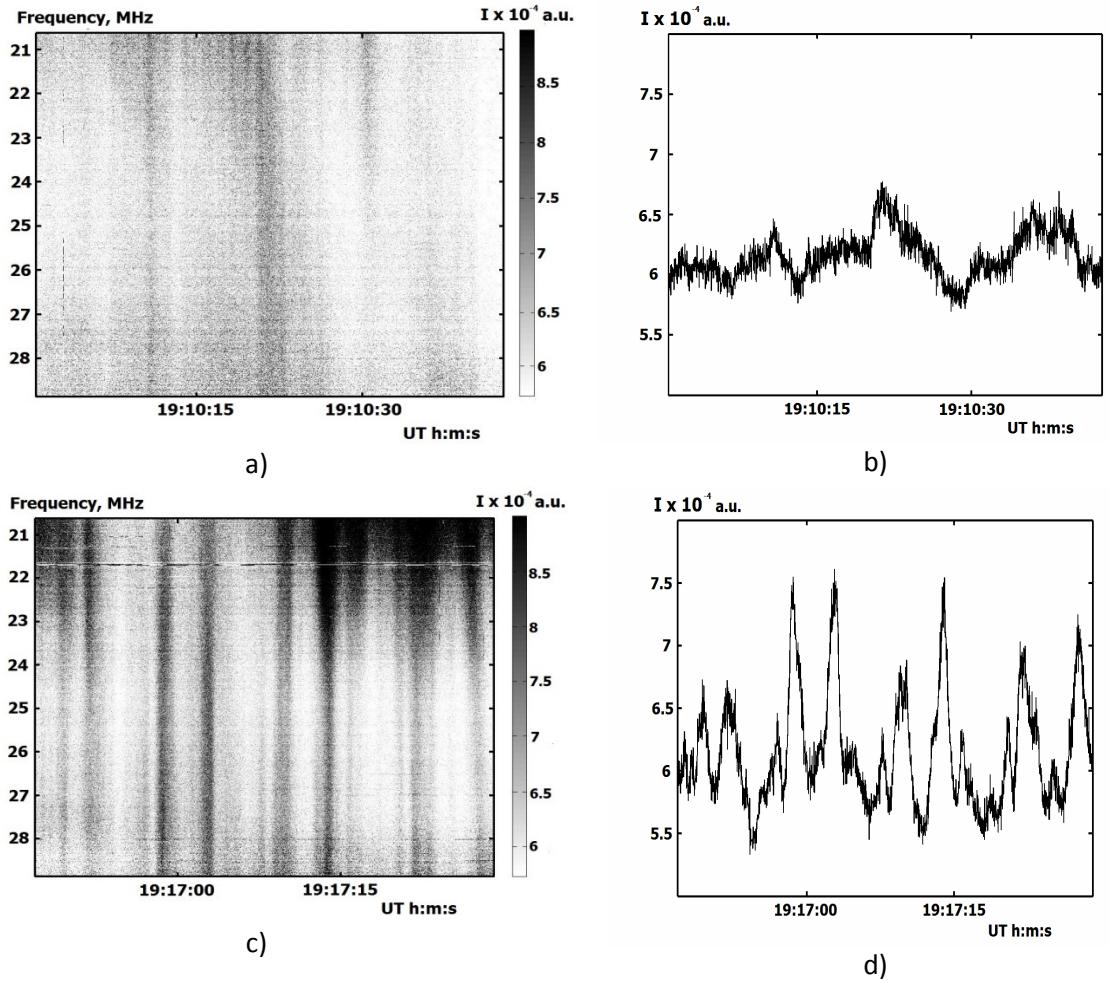

Figure 1. Two examples of data recordings for February 17 (a, b) and February 18 (c, d). a) and c) are dynamic spectra (intensity in arbitrary units on the frequency vs time plane). b) and d) are the sections of the corresponding dynamic spectra at the frequency of 25MHz.

DATA PROCESSING

Data processing consists in estimation of power spectrum $P(\nu)$ and scintillation index m for all radio sources and for all days of observations. $P(\nu)$ is defined by

$$P(\nu) = |F(\nu)|^2 / T,$$

where $F(\nu)$ is Fourier transform of $I(t)$ process, ν is the fluctuation frequency, T is the duration of time series.

Scintillation index m is determined from formula

$$m = \frac{\sigma_{IPS}}{\overline{I(t)}} = \frac{\sqrt{\sigma^2_{(IPS+n)} - \sigma^2_n}}{\overline{I(t)}} \quad ,$$

where $\overline{I(t)}$ is the mean intensity of the radio source, σ^2_{IPS}, σ^2_n, $\sigma^2_{(IPS+n)}$ - are the dispersions of the interplanetary scintillations, noise and their sum estimated from the power spectrum.

DATA ANALYSES

Figure 2 shows the averaged power spectra which were estimated for 5 observational days (radio source 3C144, Crab Nebula). It is clearly seen the difference of the cutoff frequency for each spectrum. For February 18, 19 and 20 the cutoff frequencies are equal to 0.3, 0.15 and 0.12, correspondingly.

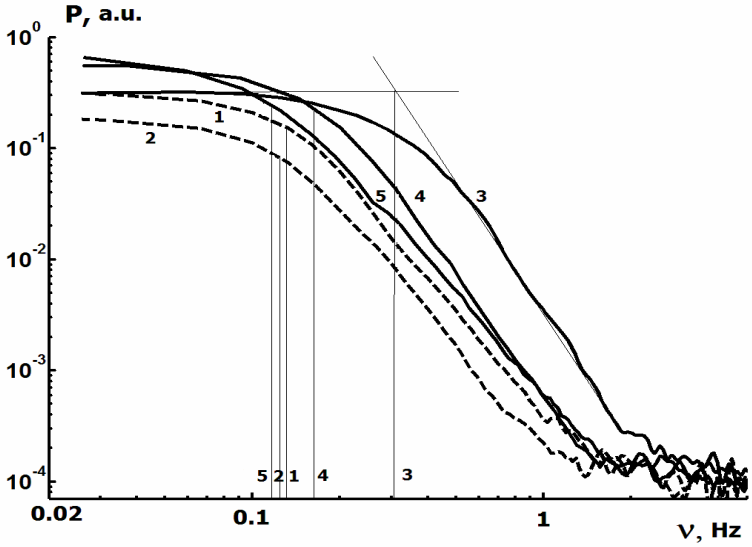

Figure 2. Power spectra for radio source 3C144: 1 - 16.02.2011, 2 - 17.02.2011, 3 - 18.02.2011, 4 - 19.02.2011, 5 - 20.02.2011

The behaviour of the scintillation index during the corresponding days for observed radio sources is demonstrated in Figure 3. The abrupt increase of the scintillation index on late 18^{th} to early 19^{th} February 2011 is connected with the appearance of ICME on the lines of sight to the observed radio sources.

Knowledge of the cutoff frequency allows conclusions to be made on the distance to the scattering layer using simple formulas (phase screen model):

$$\nu_{cutoff} = \frac{V_{\perp}}{\sqrt{2\pi\lambda z}},$$

from which the distance to the scattering layer can be defined by

$$z = \frac{V_{\perp}^2}{2\pi\lambda\nu_{Френ}^2}$$

For 3C144 the distance z is equal to 0.2, 0.6. and 1.0 a. u. for February 18, 19 and 20, correspondingly. For 3C273 the distance z equals 0.1, 0.4 and 0.7 a. u. The position of CME in the interplanetary medium beyond Earth's orbit can be reconstructed by using data from all radio sources and accepting cone model of CME (Lee et al. 2013) (see Figure 4).
Analyses of all data allows the following conclusions to be made.

CONCLUSIONS

The carried out investigations showed the high efficiency of the interplanetary scintillation method in the decameter range of radio waves for discovering and studing ICME beyond Earth's orbit. It is established that coronal mass ejection in the interplanetary medium continues slowing at distances from 1 to 1.7 au from the Sun, its velocity tending to the velocity of the ambient solar wind, the angular size being not less than 66^0.

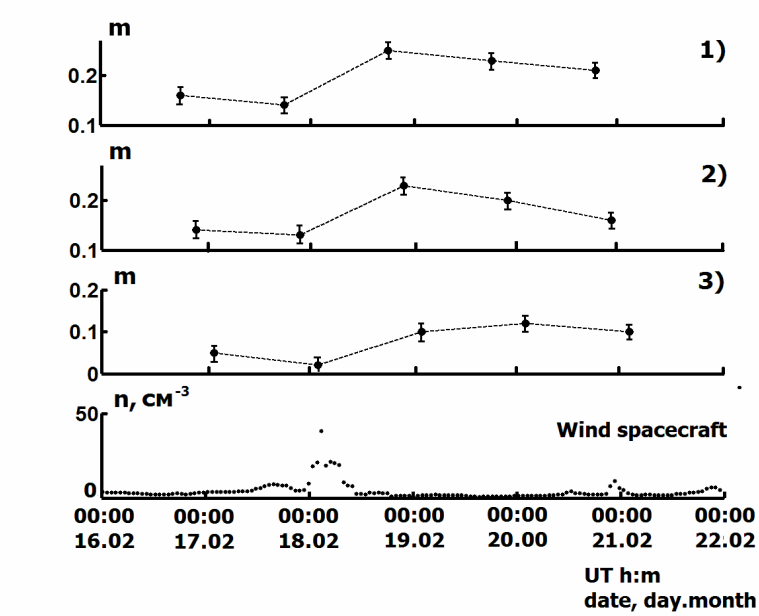

Figure 3. The behaviour of the scintillation index during the corresponding days for observed radio sources (1 - 3C144, 2 - 3C196, 3 - 3C273) and the proton density in the solar wind measured by NASA spacecraft Wind (the bottommost panel of the Figure)

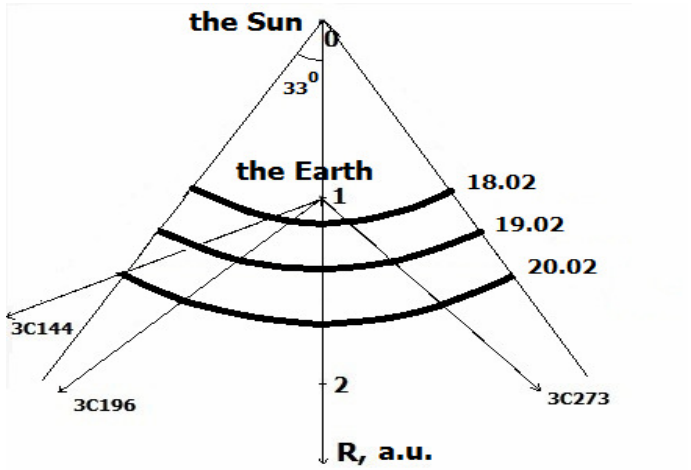

Figure 4. The position of CME in the interplanetary medium beyond Earth's orbit for February 18, 19 and 20, 2011.

REFERENCES

Braude, S.J., Megn, A.V., Sodin, L.G. 1978, in A.Pistolkors (ed.), Antennas, 26, 3.

Hewish, A., Scott, P.F., Wills, D. // Nature. -1964. -Vol. 203, 1214.

Lee C.O., Arge C.N., Odstrcil D., Millward G., Pizzo V., Quinn J.M., Henney C.J. Ensemble modeling of CME propagation. // Solar physics. -2013.-Vol. 285, Issue 1. - P. 349-368.

Megn A.V., Sharykin N.K., Zakharenko V.V., Bulatsen V.G. Brazhenko A.I. Vashishin R.V. Decameter radio telescope URAN-2 // Radiofizika i radioastronomia. -2003. - V. 8, N 4. - P. 345 -356.

Ryabov V.B. Vavriv D.M., Zarka P. A low-noise, high-dynamic-range, digital receiver for radio astronomy applications: an efficient solution for observing radio-bursts from Jupiter, the Sun, pulsars, and other astrophysical plasmas below 30 MHz // Astron. Astrophys. -2010. - Vol. 510. – P. 13.

CMEs and frequency cut-off of solar bursts

Aleksander Stanislavsky, Aleksander Konovalenko, Artem Koval, Yaroslav Volvach

Institute of Radio Astronomy, 4 Chervonopraporna Str., Kharkiv 61002, Ukraine
E-mail: astex@ukr.ua

ABSTRACT

Observations of solar bursts with high-frequency cutoff by the radio telescope UTR-2 (near Kharkiv, Ukraine) at 8-33 MHz on 17-19 August 2012 are presented. Such cut-off may be attributed to the emergence of the burst sources behind limb of the Sun toward the Earth. The events are strongly associated with solar eruptions occurred in a new active region. Ray tracing calculations show that the CMEs play a constructive role for the behind-limb bursts to be detected in ground-based observations. Likely, due to tunnel-like cavities with low density in CMEs, the radio emission of solar bursts is directed to the Earth.

INTRODUCTION

Coronal mass ejections (CMEs) tightly are associated with three types of low-frequency radio bursts [1], namely II, III and IV types. The bursts mirror the processes that initiate and develop phenomena accompanying CMEs. In particular, the source of type III bursts is accelerated electrons propagating along open magnetic field lines, whereas type II bursts are emitted by electrons accelerated in shocks. Consequently, each type of the bursts has visibly different frequency-drift rates on dynamical spectra of radio observations. The same is related to type IV bursts, radiation of which involves acceleration of electrons trapped in magnetic arches. The magnetic arches can be stretched and compressed by CMEs [2]. Of the sporadic radio emission from the Sun, the type III bursts are likely most indicative of eruptions of energetic particles. They provide important diagnostics of the ambient medium through which the solar disturbances propagate and can be used as natural plasma probes traversing the corona. Note, our understanding of the bursts and their relations to CMEs are far from perfect. Although type III bursts are observed from 500 MHz to tens kilohertz, they do not always show a frequency drift from the highest frequencies to very low ones. In particular, the low-frequency cut-off of solar bursts in the ground-based observations is imposed by the ionosphere. On the other hand, as it is well known (see, for example, [3]), often the bursts observed at metric wavelengths are not observed at decametric range of wavelengths, and on the contrary many bursts are not observed at hectometric and kilometric wavelengths and are clearly detected in ground-based observations at decametric wavelengths. The reasons for these cut-offs have not fully understood yet. In this report we consider the solar bursts with high-frequency cutoff at decametric wavelengths, and a possible source of such burst radio emission is discussed as applied to the interpretation of their cut-off features.

OBSERVATIONS

During this observation the UTR-2 radio telescope was operated in the mode includes four sections of the north-south array of the antenna. The total effective area of these four sections is 50 000 m^2 with the beam pattern size of 1°×15° at 25 MHz. On 17-19 August 2012 we observed some tens of solar bursts with high-frequency cut-off. Their frequency cut-off varies from event to event in the range 14-30 MHz, and the frequency drift rate was from 0.3 MHz/s up to some ones MHz/s. Sometimes the bursts show a fine structure similar to bright filaments with small frequency drift rate. Therefore, they were even named "caterpillar" in [4]. The bursts with high-frequency cut-off are characterized by a relatively low degree of polarization about 10 % [5] that points out to their occurrence at the second harmonic relative to the local plasma frequency. Figure 1 shows the dynamic radio spectrum of one example of them at 8:16 UT on 18 August 2012. The data were recorded by the digital DSP spectrometer operating in the frequency range of 8-33 MHz with a frequency-time resolution in 4 kHz and

100 ms, respectively. The given burst has the frequency drift rate about -0.46 MHz/s, and the noticeable frequency of cut-off is 16. ± 1 MHz, although some weak details of radio emission occur at higher frequencies. Its flux achieved 240 s.f.u. (1 s.f.u. = 10^{-22} W/(Hz m^2)). In this event we can distinguish two components. One of them has the duration about 20 s at 10 MHz and 8 s at 16 MHz, and the second component lasts 14 s.

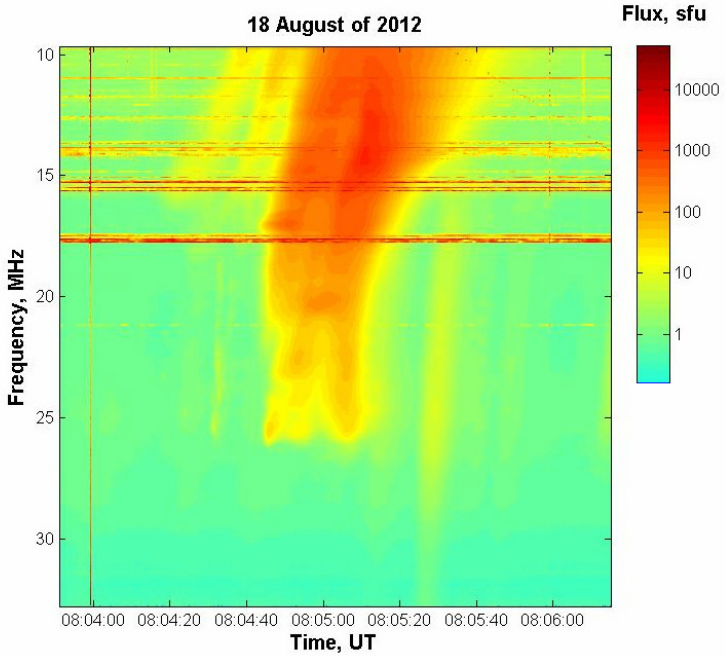

Figure 1: An illustrative example of the bursts with high-frequency cut-off on 18 August 2012. The horizontal bright lines on the dynamic spectrum indicate intensive disturbances due to broadcast radio stations.

On 17-19 August 2012 many C-class and M-class X-ray flares, following each other, were observed (see Figure 2 as an example) by STEREO, GOES and SOHO spacecrafts. The solar activity is also accompanied with CMEs emerging near the solar limb, if the events are viewed toward the Earth. They were connected with NOAA active region 11548 invisible from the Earth.

PROBLEM

The simplest interpretation of the cutoff leads to the conclusion that the location of their radiating sources is behind the Sun relative to an observer on Earth, and the bursts are emitted at the second (H) harmonic of the local plasma frequency [4]. Then the high-frequency radiation part is hidden (occulted) by the solar corona. However, this explanation needs to be clarified. In this connection also it should be accounted for the refraction of radio emission in coronal plasma. Because of this effect the ray tracing from the burst sources, located behind the solar limb, may be directed away from the Earth.

Really, from the refractive index variation with height in the solar corona, the path of a radio emission ray is calculated with help of the Snell's law [6, 7]. Without loss of generality we assume the spherical symmetry that simplifies the ray tracing calculations. The refractive index is written as $n^2 = 1 - f_{pe}^2 / f^2$, where $f_{pe} = 8.98\sqrt{N_e}$ is the electron plasma frequency in kHz, and N_e (cm^{-3}) describes the electron density of the solar corona in dependence of the distance ρ from the center of the Sun. The point (ρ, θ) of the ray tracing obeys the equation

$$\theta = a\int_{\rho}^{\infty} \frac{d\rho}{\rho\sqrt{n^2\rho^2 - a^2}},$$

where a is the distance of the asymptote of the ray for large ρ with $n=1$. Here θ is the angle between the line through the center of the Sun, parallel to the asymptote, and the direction on the ray position [6]. As the radius of the Sun is 109 times the radius of the Earth, the value a becomes very small (close to zero) in our study. It is not difficult to show that in this case the angle θ is proportional to a for any model of the solar electron density. This means that the value $\theta \geq \pi/2$ requires a special case of the electron density variation with height in the solar corona, namely the refractive index should be close to one. Therefore, the scheme of propagation of post-limb radio emission, if it is watched on the Earth, should be developed in a new way. In this problem we notice the important contribution of CMEs that took place near the solar limb. Their occurrence strongly is correlated with the emergence of solar bursts with high-frequency cut-off.

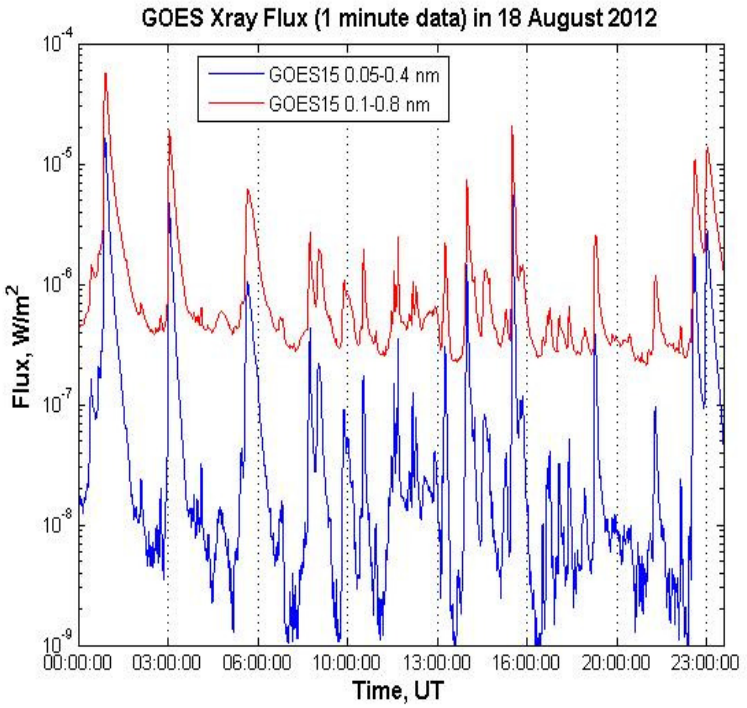

Figure 2: A time series of solar X-ray emission observed by the GOES-15 on 18 August 2012.

RESULTS

As a CME emerges, it typically contains a lower-density cavity behind its crest (dark bands at LASCO frames), and it often has a bright prominence core embedded within it [8]. The interesting feature of CMEs indicates that they may form tunnel-like cavities with low density. Under appropriate conditions this permit burst sources, moving behind the solar limb (relative to an observer on the Earth), to emit radio signals towards the Earth through or due to such cavities (Fig. 3). Probably, the radiation is observed in ground-based observations as solar bursts with high-frequency cut-off.

Based on the study, we guess that the bursts with high-frequency cut-off are nothing else, but type III radio bursts. However, since their source is located behind the solar limb toward the Earth, the effects of radio wave propagation in tunnel-like cavities of the solar corona can distort the observed frequency-drift rate of the bursts. This explains why some of them have the frequency drift rate as one in type III radio bursts, and others are not. Moreover, the duration of the behind-limb bursts may be somewhat more than one typical for type III bursts at decametric wavelengths because of the confluence of several nearby bursts with delay.

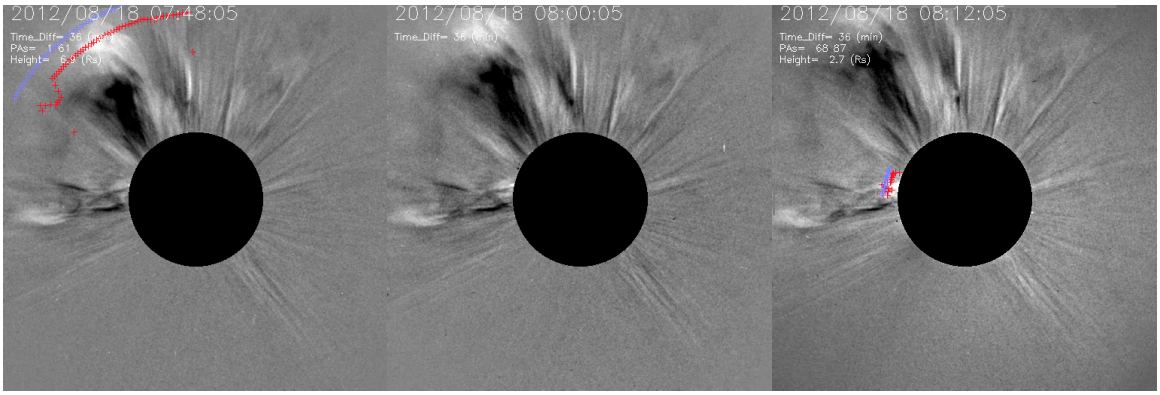

Figure 3: Image of the solar corona, taken by the LASCO coronagraph (C2) on the SOHO observatory. Image courtesy of the SOHO team.

ACKNOWLEDGEMENTS

We thank the GOES and SOHO teams for developing and operating the instruments and we are grateful for their open data policy. This research was partially supported by Research Grant "Synchronized simultaneous study of radio emission of solar system objects by low-frequency ground- and space-based astronomy" from the National Academy of Sciences of Ukraine.

REFERENCES

[1] N. Gopalswamy, "Coronal Mass Ejections and Solar Radio Emission", in Planetary Radio Emissions VII, H.O. Rucker, W. S. Kurth, P. Louarn, and G. Fischer, Eds. Austrian Academy of Sciences Press, Vienna, pp. 325-342, 2010.

[2] A.A. Konovalenko, A.A. Stanislavsky, et al., "Absorption in Burst Emission", Solar Phys., vol. 245, pp. 345–354, 2007.

[3] H. Alvarez, F. Haddock, and R.P. Lin, "Evidence for Electron Excitation of Type III Radio Burst Emission", Solar Phys., vol. 26, pp. 468-473, 1972.

[4] V.N. Melnik, A.I. Brazhenko, et al., "Unusual Solar Radio Burst Observed at Decameter Wavelengths", Solar Phys., vol. 289, pp. 263-278, 2014.

[5] A.I. Brazhenko, private communication, 2014.

[6] R.N. Bracewell, and G.W. Preston, "Radio Reflection and Refraction Phenomena in the High Solar Corona", Astrophys. J., vol. 123, pp. 14-29, 1956.

[7] G. Thejappa, and R.J. MacDowall, "Localization of a type III burst observed by the STEREO spacecraft", Astrophys. J., vol. 720, pp. 1395-1404, 2010.

[8] S.E. Gibson, T.A. Kucera, et al., "Three-dimensional Morphology of a Coronal Prominence Cavity", Astrophys. J., vol. 724, pp. 1133-1146, 2010.

Advances in solar bursts observations by the low-frequency radio telescopes of a new age

I.N. Bubnov, A.A. Stanislavsky, A.A. Konovalenko, S. Yerin,
A.A. Gridin, A.A. Koval
Institute of radio astronomy national academy of sciences of Ukraine
E-mail: boobnov@mail.ru

ABSTRACT

Observations of solar radio emission and the impact of solar activity on the space weather is one of the hot topics in astrophysics today. In particular, a great variety of the bursts is observed at frequencies below 100 MHz. This paper is devoted to a new sub-array of Giant Ukrainian Radio Telescope (GURT) and recent results obtained with this instrument as applied to the study of sporadic solar radio emission within 10-70 MHz range. Wideband observations at decameter-meter wavelengths considerably extend the possibility in registrations of rare solar events. The examples of such phenomena recorded in 2012 and 2014 are given. The study of ionosphere scintillations of cosmic radio sources well adds the analysis of solar events.

INTRODUCTION

Observations of solar radio emission and the influence of solar activity on interplanetary medium, magnetosphere, ionosphere and atmosphere of the Earth is one of the most important task today. Such observations should be carried out in a wide frequency range and with high time-frequency resolution to detect a fine structure of sporadic radio bursts. A great variety of the bursts is observed at frequencies below 100 MHz. This is one of the main reasons to devote so much observational time for the study of solar radio emission in scientific programs at modern low-frequency instruments such as LOFAR, LWA and so on [1].

OBSERVATIONS

A short description of the sub-array of new low frequency Giant Ukrainian Radio Telescope (called briefly GURT) and recent results of radio astronomy observations with help of this instrument within 10-70 MHz range are presented [2,3]. Examples of solar III and III-B type bursts are shown. A very rare phenomenon, the solar low-frequency U-burst, which is generated by electrons moving along closed magnetic field lines at solar corona, has been registered [4]. Wideband observations in decameter and meter wavelengths ranges considerably raise the probability of burst registrations in harmonic pairs. Such pairs are generated at first and second harmonics of electron plasma frequency. Examples of the phenomena registered in 2012 and 2014 are given. In addition the records of ionosphere scintillations of cosmic radio sources which can be used for studies of ionosphere conditions in the place of radio astronomy observations are presented.

CONCLUSION

The presented results show that the built GURT sub-array can be used for intensive studies of sporadic solar radio emission as well as ionosphere scintillations. Further extending of GURT radio telescope effective area with building new additional sub-arrays will allow increasing the spatial resolution for solar observations and using methods of both ionosphere and interplanetary scintillations for measuring the parameters of ionosphere and interplanetary media (study of solar wind).

REFERENCES

[1] S. M. White, N. E. Kassim, and W. C. Erickson, Solar radioastronomy with the LOFAR (LOw Frequency ARray) radio telescope, in Innovative Telescopes and Instrumentation for Solar Astrophysics, vol. 4853 of Proceedings of SPIE, pp. 111–120, Waikoloa, Hawaii, USA, August 2002.

[2] A.A. Konovalenko, I.S. Falkovich, N.N. Kalinichenko, A.A. Gridin, I.N. Bubnov, A. Lecacheux, C. Rosolen, H.O. Rucker, Thirty-element active antenna array as a prototype of a huge low-frequency radio telescope, Experimental Astronomy, vol. 16, no. 3, pp. 149–164, 2003.

[3] A. A. Stanislavsky, I. N. Bubnov, A. A. Konovalenko, A. A. Gridin, V. V. Shevchenko, L. A. Stanislavsky, D. V. Mukha, and A. A. Koval, First Radio Astronomy Examination of the Low-Frequency Broadband Active Antenna Subarray, Advances in Astronomy, Vol. 2014 (2014), Article ID 517058, 5 p., http://dx.doi.org/10.1155/2014/517058.

[4]. V. Dorovskyy, V. Melnik, A. Konovalenko, I. Bubnov, A. Gridin, N. Shevchuk, H. Rucker, S. Poedts, and M. Panchenko, Decameter U-burst Harmonic Pair from a High Loop, Solar Phys., Vol. 290 (1), pp. 181-192, 2015.

Analysis of the Nonlinear Behavior of the Accretion Flows

Krasimira Yankova[1]

[1] Space Research and Technology Institute – Bulgarian Academy of Sciences
E-mail: *f7@space.bas.bg*

Abstract

In this paper a research of the accretion flow structures in disks on Cyg X-1 and SgrA* have been done. We analyze the behaviour on the advective hypothesis. We discuss influence of the self-induction advection over components on the systems disk - corona in these real objects.

Introduction

We have developed a new model of the accretion disc's magneto-hydrodynamics, based on some specific advective hypothesis, presented in Yankova (2013, 2015). We constructed geometrically thin, optically thick, one-temperature Keplerian disc in a normal magnetic field, around a black hole.

The results of the model, given in detail in Iankova (2007a, b), Iankova (2009), Yankova (2012a, b, c), we presented global model for radial and vertical structures of disk; model for local structure and adaptation of the model for the conditions of emerging corona.

Results and analyze

We applied the model in real sources, and we will analyze the results for the nature of the flow in them.

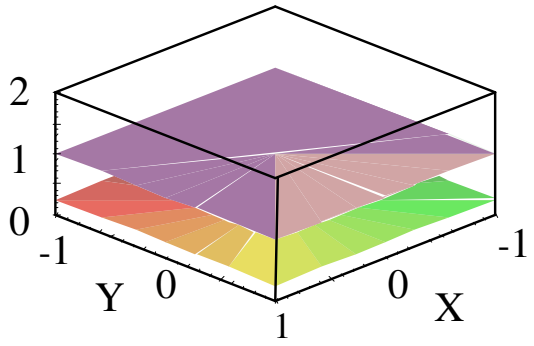

Fig.1a: Distribution $f_3(X,Y)$ of the dimensionless function of the sound velocity $f_3(x,\varphi)$ in the plane disc (X,Y) at $t=1P\sim\Omega_0^{-1}$.

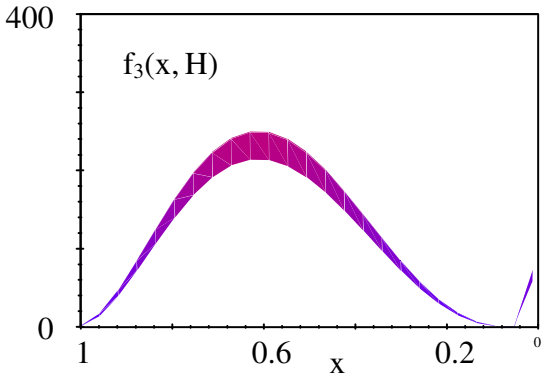

Fig.1b:Distribution $f_3(X,H)$ of the dimensionless function of the sound velocity $f_3(x,Z)$ on the border between the corona and disc.

The results for the sound velocity (Figure 1a) indicate that the function forming two well-distinguishable independent main branches. This means that a period after spreading of the disc it starts forming compacting zones - rings with a higher density relative to the environment. Local model of these formations determine clearly their advective character and distinguish them uniquely from the spirals on the disc.

In the binary, the branch of advective rings was layered additional (Figure 2a), which means secondary packing of the radiation in the flow from the fluidic optical fibers formed in the disc. In the disk of galactic core, ring-like areas remain unilamellar (fig.2b) and as shows the continuity of the surfaces of the two branches of the function, advective rings and both cases are mobile in accordance with their physical selves.

$$\frac{\partial(\rho v_i)}{\partial t}+\frac{\partial}{\partial x_j}\left(\rho v_i v_j\right)=\rho\left(\frac{\partial v_i}{\partial t}+v_j\frac{\partial v_i}{\partial x_j}\right)=\rho\frac{Dv_i}{Dt} \qquad (1)$$

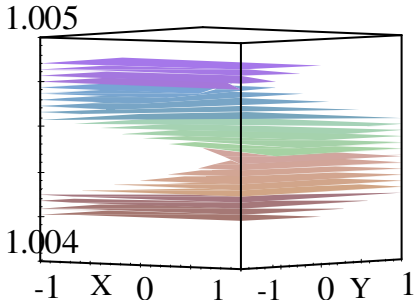

Fig.2a: Distribution $f_3(X,Y)$ of the dimensionless function of the sound velocity $f_3(x,\varphi)$ in the plane disc (X,Y) at t=1P~Ω_0^{-1}, for Cyg X-1.

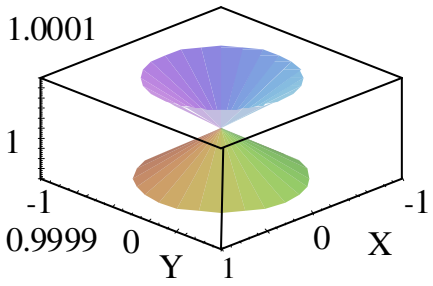

Fig.2b: Distribution $f_3(X,Y)$ of the dimensionless function of the sound velocity $f_3(x,\varphi)$ in the plane disc (X,Y) at t=1P~Ω_0^{-1}, for SgrA*.

By the development of the components of the magnetic field provides information about the microstructures present in the stream, and their behaviour.

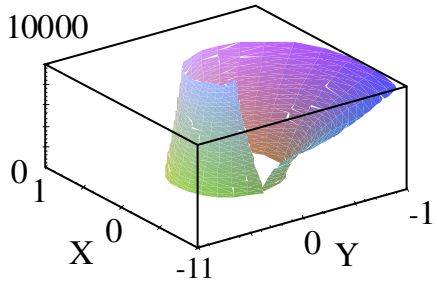

Fig.3a: Distribution $f_5(X,Y)$ of the dimensionless function of the radial field $f_5(x,\varphi)$ in the plane disc (X,Y) at t=1P~Ω_0^{-1}, for Cyg X-1.

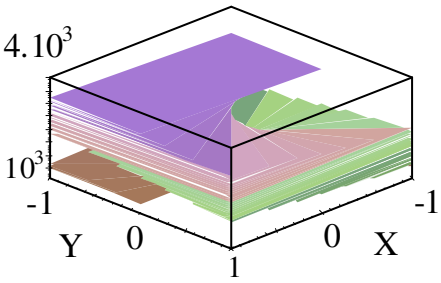

Fig.3b: Distribution $f_5(X,Y)$ of the dimensionless function of the radial field $f_5(x,\varphi)$ in the plane disc (X,Y) at t=1P~Ω_0^{-1}, for SgrA*.

In Cyg X-1 amplified asymmetry is observed in $\mathbf{B}_r$ (fig.3a). The function does not show clustering around discrete values in increase, what we see in Sgr A * (fig.3b). The projection of $f_6(x, \varphi)$ (fig.4b) indicates that the disc has a plurality of different sized loops - both positive and negative relative to the direction of flow. All this means continuous cascade that maintains the negative gradient of entropy and with it the self-induction in the advection.

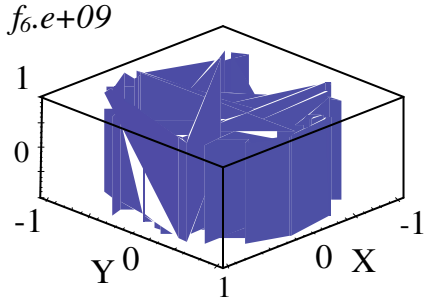

(a)

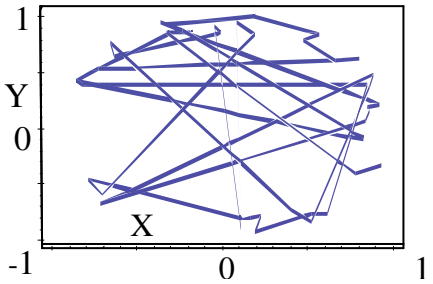

(b)

(c)

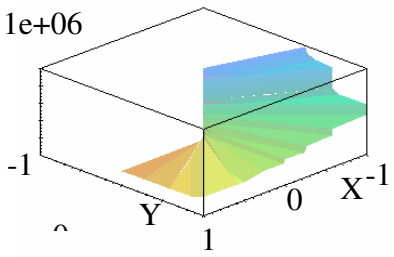

Fig.4: Distribution $f_6(X,Y)$ of the dimensionless function of the azimuthal field $f_6(x,\phi)$ in the plane disc (X,Y) at $t=1P\sim\Omega_0^{-1}$, for Cyg X-1 (4a, b). And SgrA*(4c).

The behavior of the function $\mathbf{B}_r$ at Sgr A * (fig.3b) shows the existence of different groups MPH, with the exchange of energy between the low and high harmonics in the spectrum (see also the leaps increasing on $f_6(x, \varphi)$ (fig.4c)). This is fragmented and consolidated of loops, accompanied with absorbing energy from the environment during the above-mentioned exchange. Growing microstructures compensate the effects of negative entropy gradient (fig.6b), as absorb energetic surplus. This reserve ensures the reemergence of the ML from plasma in another way, and with this explains simplified advective rings on this disc.

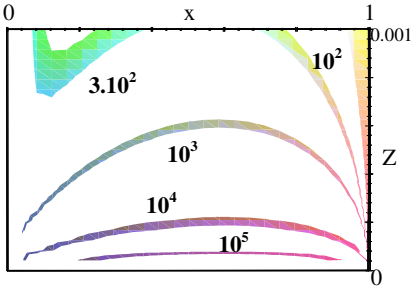

Fig.5a: Profile in the plane (x, Z) of the sound velocity for the point of inflow $\phi_0 = 0$, at the time $t = 1P \sim\Omega_0^{-1}$, in $f_3(x, Z)=10^2; 3.10^2; 10^3; 10^4; 10^5$, for Cyg X-1.

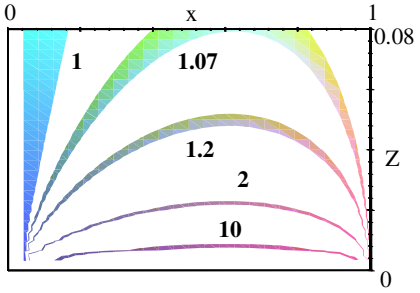

Fig.5b: Profile in the plane (x, Z) of the sound velocity for the point of inflow $\phi_0 = 0$, at the time $t = 1P \sim\Omega_0^{-1}$, in $f_3(x,Z) =1; 1.07; 1.2; 2; 10$, for SgrA*.

Vertical distribution of sound velocity is especially sensitive to the exchange and distribution of energy in the disk, which is controlled by the overall interaction between parameters and the impact of nonlinear effects on them. Arched contours in the vertical structure of the disk show that in the inner regions of a re-stabilization of the stream, which is confirmed by the recovery of the positive gradient of entropy (fig.5-6). This stabilization was mainly due to the emerging corona.

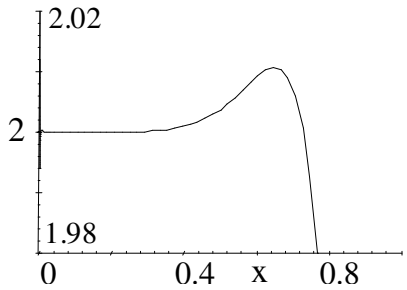

Fig.6a: Development of the gradient of entropy in Cyg X-1.

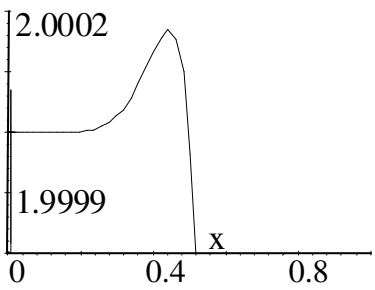

Fig.6b: Development of the gradient of entropy in SgrA*

Conclution

In this paper, we use the results of the theoretical model of the disk, to description of the processes in the disk and on boundary with the corona at two real objects. Advective rings which provide the warming of the pad, determine the type of the border with the corona. At Cyg X-1 rings of this type contribute to form a sharp boundary between the disc and the corona and both components of the system can be considered individually. Cannibalism of instabilities in the disk of SgrA* and incomplete re-stabilization of the stream (as opposed to micro-quasar) talked about fuzzy border. Components is well be considered complex there, but still can be considered individually depending on the degree of fuzziness of the border.

These results are another step in the direction of for creating full model of the system disk-corona. Also, tool for determining the degree to which the main component influenced the development of coronary component.

References

Iankova Kr. D.: 2007a, BSSPP Proc. Ser. 1, pp 143-146.

Iankova Kr. D.: 2007b, 5th Bulgarian-Serbian Conference (V BSCASS): "Astronomy and Space Science", Heron Press Ltd.Science series, pp 326-29.

Iankova Kr. D.: 2009, Proc. VI Serbian-Bulgarian Astronomical Conference, Publ. Astr. Soc. "Rudjer Bољkovi ", No. 9, 327-333.

Yankova Kr. D.: 2012a, SSTRI-BAN, SENS 2011 proceedings, ISSN 1313-3888, 73-78.

Yankova Kr.D.: 2012b, Publications of the Astronomical Society "Rudjer Boskovic", vol. 11, pp.375-383. Hhttp://adsabs.harvard.edu/abs/2012PASRB..11..375YH

Yankova Kr.D.: 2012c, JUBILEE INTERNATIONAL CONGRESS: SCIENCE, EDUCATION, TECHNOLOGIES "40 YEARS BULGARIA – SPACE COUNTRY ", proceedings (ISBN 978-954-577-636-6), Tom1, 152-158.

Yankova Kr.D.: 2013, Proceedings of the VIII Serbian-Bulgarian Astronomical Conference (VIII SBAC), Publ. Astron. Soc. “Rudjer Bošković” vol. 12, 375-381. Hhttp://wfpdb.org/ftp/8_SBAC_D1/pdfs/34.pdf

Yankova Kr.: 2015, Bulgarian Astronomical Journal, Vol. 22, p. 83. http://adsabs.harvard.edu/abs/2015BlgAJ..22...83Y

Delayed response of global TEC to ionization variations seen from combined SolACES-SDO/EVE solar EUV spectra

Jacobi Ch [1], *Unglaub C* [1], *Schmidtke, G* [2], *Pfeifer M* [2], *Schäfer R* [2], *Brunner R* [2], *Woods T* [3], *Jakowski N* [4]

[1]Institute for Meteorology, Universität Leipzig , [2]Fraunhofer IPM, Freiburg, [3]LASP, University of Colorado, Boulder, CO, [4]German Aerospace Center, Neustrelitz
E-mail: jacobi@uni-leipzig.de

INTRODUCTION

The solar extreme ultraviolet (EUV) radiation varies on different time scales, including the 27-day Carrington rotation as one of the primary sources of variability at the intra-seasonal time scale. Consequences are strong changes of ionization of the Earth´s upper atmosphere, and corresponding variability of the electron density and also the Total Electron Content (TEC). TEC variability is a coarse estimate for ionization as well, so that indices describing EUV and ionization may be compared against ionospheric TEC. Such indices may be obtained from integrating observed EUV spectral solar flux, e.g. from the SDO/EVE experiment (Woods et al., 2012) in the relevant wavelength range. Unglaub et al. (2011) have introduced a proxy, termed EUV-TEC, which is based on the vertical and globally integrated primary ionization rates calculated from observed EUV spectra.

However, correlation of parameters describing ionospheric electron density and EUV proxies is not always strong at time scales of the solar rotation, and several studies report a delayed response of the ionospheric plasma density to solar activity changes (e.g. Jakowski et al., 1991; Lee et al., 2012). Therefore, this ionospheric delayed response is analyzed here, and taken into account in the EUV proxies.

EUV proxy and analysis of delay

We calculate a daily EUV proxy as the SDO/EVE Version 5 data integrated between 16.5 and 105.5 nm. Daily global mean TEC values have been calculated based on IGS TEC maps (Hernandez-Pajares et al., 2009) in order to evaluate this EUV proxy. The data were normalized by subtracting the mean and dividing by the standard deviation from January 20, 2011 through March 10, 2014 (approx. Carrington rotations 2106 - 2147). The mean values and standard deviations are 3.822±0.387 mWm^{-2} for SDO/EVE fluxes, and 24.41±6.05 TECU for global TEC. Figure 1 presents the normalized EUV flux and global TEC from 2011 through early 2014. The observations cover part of solar cycle 24, with generally increasing solar flux and consequently ionospheric TEC. The time series is too short to investigate the 11-year solar cycle. Generally there is good agreement of TEC and EUV at the interannual time scale. At the seasonal time scale there are some discrepancies owing to the semiannual TEC cycle which is not seen in EUV. At the 27-day time scale of the solar rotation there is considerable agreement between the time series when the amplitudes are large, although the amplitudes not always correspond to each other.

In order to analyze the correlation of TEC and EUV proxies at different time scales, we filtered the normalized data using a Lanczos bandpass filter with 100 weights. In Figure 2, part of the time series of SDO/EVE integrated fluxes and TEC are presented for time scales of 2-90 days and for 24-28 days. The variability is mainly determined by the 27-day solar rotation, and a time delay is visible between the EUV flux (black) and TEC (red). The squared correlation coefficient between normalized TEC and EUV at the time scales 2-90 days is $r^2 = 0.75$. Longer time scales than 90 days will not be considered here, because these are dominated by the annual cycle, which is different for TEC and solar radiation, and part of the 11-year cycle.

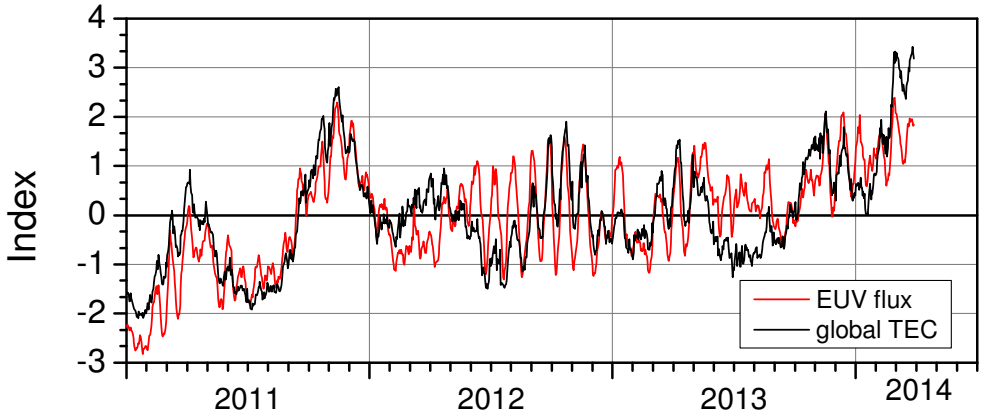

Figure 1: Normalized integrated EUV flux from SDO/EVE Version 5 spectra and global TEC.

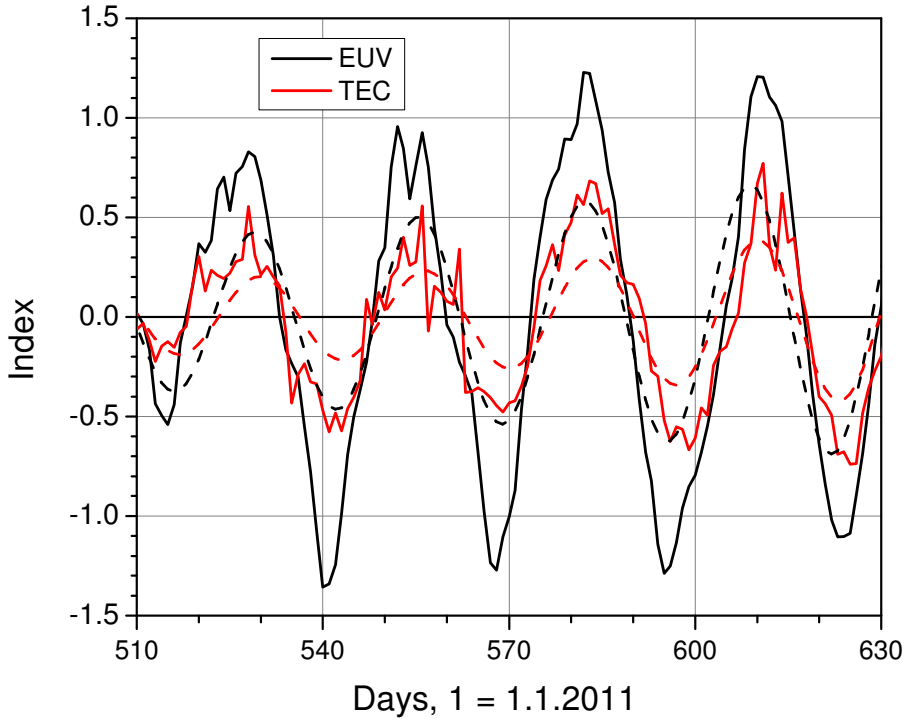

Figure 2: Time series of EUV integrated fluxes and global TEC in different the 2-90 days (solid) and 24-28 days (dashed) period bands.

To systematically investigate the delay at different time scales, we now filtered the time series in different period bands, and the cut-off periods of the Lanczos filter were chosen in such a way that each period band ranges over 4 days, while the centre of the period band was shifted from 4 to 88 days. For each pair of filtered time series, i.e. for each time scale, the cross-correlation function is shown in Figure 3. Positive values indicate that TEC variations lag EUV ones. Solid blue dots are added that show the time lag with maximum correlation which can, however, only be provided at an accuracy of one day. We also analyzed a EUV-TEC proxy after Unglaub et al. (2011), based on the combined SDO/EVE and SolACES (Schmidtke et al., 2014) spectra in this wavelength interval. EUV-TEC is calculated as the primary ionization using a NRLMSISE-00 (Picone et al., 2002) model atmosphere. The proxy is defined as the daily vertically and globally averaged ionization rates normalized by their time mean and standard deviation. The ionization rates were normalized by their mean and standard deviations being $1.180 \cdot 10^{19} \pm 1.23 \cdot 10^{18}$ ions/m^2. The lag of maximum correlation between this proxy and global TEC are also shown in Figure 3 as light blue dots.

Figure 2 shows that at short time scales of few days, the correlation is weak. At time scales of the solar rotation, the strongest correlation is found and global TEC lags EUV flux variations by about one day. The lag increases a bit for time scales around 2 months. For the EUV-TEC proxy, the lag at time scales of about 2 months is slightly longer. Differences to directly using SDO/EVE fluxes may be due to the fact that the EUV-TEC proxy uses the NRLMSIS-E atmosphere, which is calculated using the F10.7 solar index. At longer time scales than the solar rotation, the effect of seasonal variations of the background atmosphere will affect the proxy.

To improve the correlation between TEC and EUV flux, we shifted the TEC time series by one day. Taking into account that the time resolution of the datasets allows only a coarse approach, we did not consider small structures in the time lag at different time scales as they are visible in Figure 3. When using the shifted TEC time series, the squared correlation between normalized TEC and EUV increases to $r^2 = 0.81$.

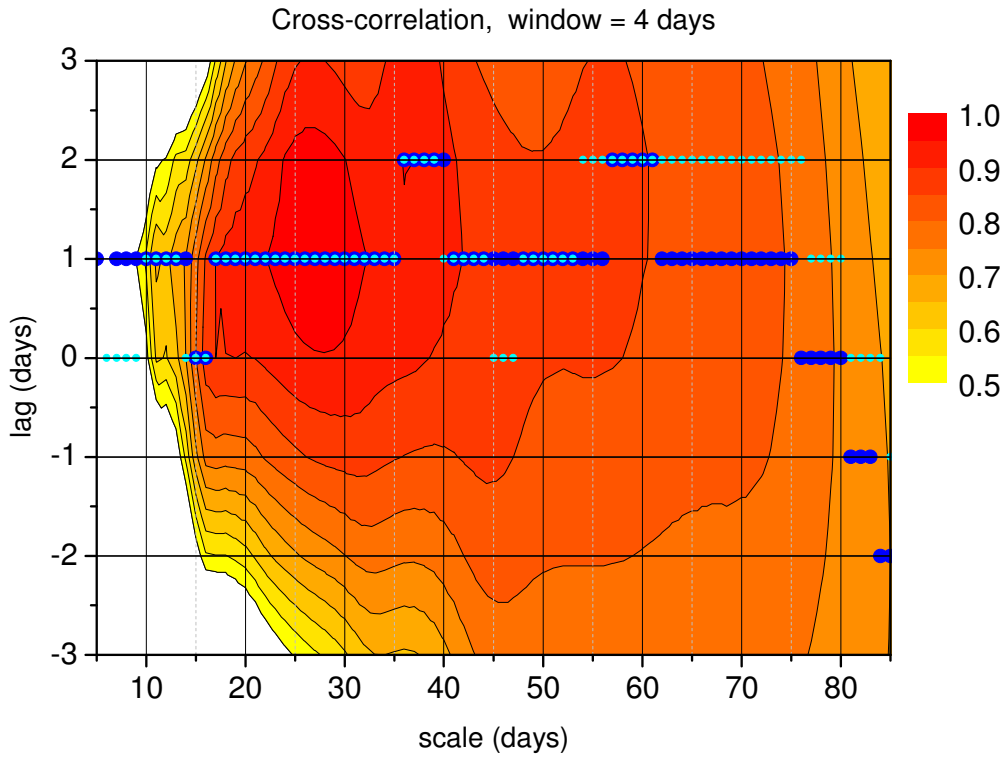

Figure 3: Cross-correlation coefficients between global TEC and SDO/EVE integrated fluxes. The scale is the centre of the 4-day period band of the respective filter. Positive values indicate that TEC variations lag EUV ones. Solid dark blue dots show the lag with maximum correlation at an accuracy of one day. Light blue dots are added that indicate maximum correlation between TEC and the EUV-TEC primary ionization proxy based on SDO/EVE and SolACES combined daily EUV spectra.

Conclusions and outlook

When taking into account the ionospheric delay at the solar rotation time scale, proxies to describe the influence of EUV on ionization rates can be improved. The results presented here are preliminary. We used daily EUV spectra and daily and globally averaged TEC, which gives only coarse values for the time lag. TEC maps are available at higher temporal resolution, and EUV fluxes at least for some spectral bands are also available. This will provide the possibility to study ionospheric delay at higher temporal and spatial resolution.

Acknowledgements: TEC data has been provided by NASA through ftp access on ftp://cddis.gsfc.nasa.gov/gps/products/ionex/.

REFERENCES

Hernandez-Pajares, M., Juan, J.M., Sanz, J., Orus, R., Garcia-Rigo, A., Feltens, J., Komjathy, A., Schaer, S.C., Krankowski, A., 2009: The IGS VTEC maps: a reliable source of ionospheric information since 1998, J. Geod. 83, 263–275.

Jakowski., N., Fichtelmann, B., Jungstand, A., 1991: Solar activity control of ionospheric and thermospheric processes. J. Atmos. Terr. Phys., 53, 1125-1130.

Lee, C.-K., Han, S.-C., Bilitza, D., Seo, K.-W., 2012. Global characteristics of the correlation and time lag between solar and ionospheric parameters in the 27-day period. J. Atmos. Sol.-Terr. Phys, 77, 219–224, doi:10.1016/j.jastp.2012.01.010.

Picone, J.M., Hedin, A.E., Drob, D.P., 2002: NRLMSISE-00 empirical model of the atmosphere: statistical comparisons and scientific issues, J. Geophys. Res., 107, 1468, doi:10.1029/2002JA009430.

Schmidtke, G., Nikutowski, B., Jacobi, Ch., Brunner, R., Erhardt, Ch., Knecht, S., Scherle, J., Schlagenhauf, J., 2014: Solar EUV irradiance measurements by the Auto-Calibrating EUV Spectrometers (SolACES) aboard the International Space Station (ISS), Solar Phys., 289, 1863-1883, doi: 10.1007/s11207-013-0430-5.

Unglaub, C., Jacobi, Ch., Schmidtke, G., Nikutowski, B., Brunner, R., 2011: EUV-TEC proxy to describe ionospheric variability using satellite-borne solar EUV measurements: first results, Adv. Space Res., 47, 1578-1584, doi:10.1016/j.asr.2010.12.014.

Woods, T.N., Eparvier, F.G., Hock, R.; Jones, A.R., Woodraska, D., Judge, D., Didkovsky, L., Lean, J., Mariska, J., Warren, H., McMullin, D., Chamberlin, P., Berthiaume, G., Bailey, S., Fuller-Rowell, T., Sojka, J., Tobiska, W.K., Viereck, R., 2010: Extreme Ultraviolet Variability Experiment (EVE) on the Solar Dynamics Observatory (SDO): Overview of Science Objectives, Instrument Design, Data Products, and Model Developments, Solar Physics, 275, 115-143, doi: 10.1007/s11207-009-9487-6.

GEOMAGNETIC Pc1 PULSATION BEHAVIOR DEPENDING ON SOLAR ACTIVITY

Feygin F.Z., Malysheva L.M., Kleimenova N.G., Khabazin Yu.G.

Schmidt Institute of the Physics of the Earth RAS, Moscow, Russia
E-mail: kleimen@ifz.ru

Abstract

The latitude feature of Pc1 geomagnetic pulsations was studied on the base of the Scandinavian magnetometer chain near the maximum and minimum of the 24-th solar activity cycle. In the minimum (2008) there were about 30 magnetic storms, but in 2009 - only 5. The number of the hours with Pc1 was ~100 in 2008 and only ~20 in 2009. During the solar minimum, the shape of the Pc1 dynamic spectra was, generally, simple and the wave duration < 3-5 hours. However, during the declining (2006) and increasing (2010) solar activity stage, the spectral structure of Pc1 became more complicated and the wave duration increased up to 10-12 hours. We compared the total, right-hand and left-hand polarized Pc1 pulsations at two latitude spaced stations: SOD (Φ=63.8^0, L~5.3) and NUR (Φ=56.6^0, L~3.5). It was found that that in 2003 (near solar maximum), the Pc1 pulsations were stronger at NUR with left-hand polarization. It means that the station was located in vicinity of the wave exit point from the ionosphere. However, in the solar minimum, the Pc1 events were stronger at SOD and demonstrated the left-hand polarization too. Our finding supports the idea that the area of Pc1 wave generation could be related to the vicinity of the plasmapause.

Introduction

The Pc1 geomagnetic pulsations are the repeated wave packets of Alfven waves in the frequency range 0.2-5.0 Hz travelling between the conjugated hemispheres. Their theory of generation and the morphological properties are widely discussed in the literature last time in several revues [e.g. Kangas et al., 1998; Demekhov, 2007]. It is no doubt that Pc1 pulsations ("pearls") are generated via the cyclotron instability of radiation belt protons with anisotropic velocity distribution [e.g. Feygin and Yakimenko, 1971 and many others].

Here we present the analyzing results of the data obtained from the ground-based induction magnetometer network at Scandinavia), stored at (http://sgo.fi/Data/Pulsation/pulArchive.php). Figure 1 demonstrated the solar activity during the discussed period.

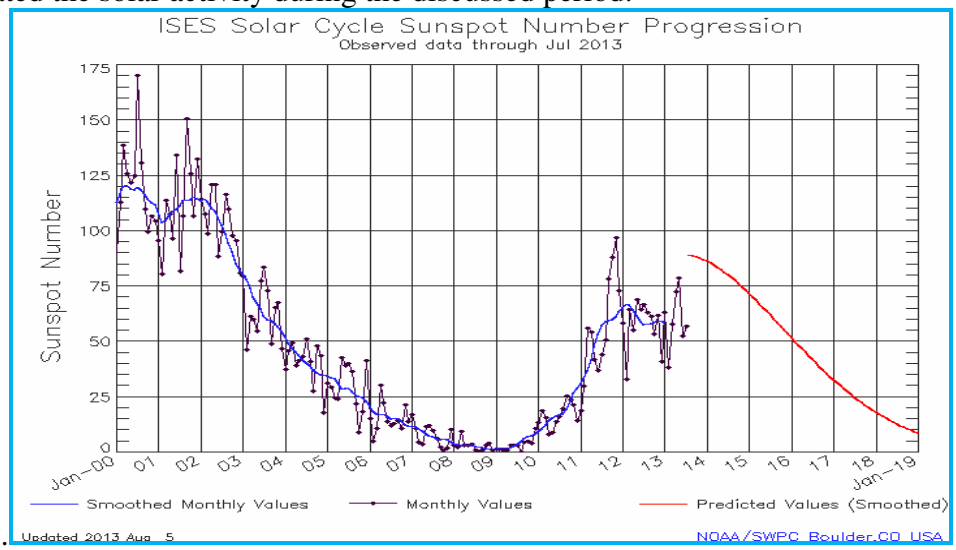

Fig.1. Solar activity (measured the Sunspot number) in 2001-2013 (blue line) and its prediction (red line).

Results of analysis

It is known, that the Pc1 occurrence maximum is observed in the declining phase of the solar activity. Really, in the declining phase of the 23-th cycle of the solar activity (2006), the number of the hours with long-lasting (more 2 hours) Pc1 series was ~270. In the minimum between 23-th and 24-th cycle, the lowest value of the Wolf number (Wp) ~ 3 was observed in 2008 and 2009. However, in 2008 there were two sequences of recurrent magnetic storms with 13-14 storms in each, but in 2009 there were only 5 small magnetic storms. Correspondingly, the number of the hours with long-lasting Pc1 series was ~100 in 2008 and it was~20 in 2009. It supports the relationship of long-lasting Pc1 generation with magnetic storms development.

The spectral structure of the Pc1 pulsations was different in quiet and disturbed magnetic conditions. An example of such events is presented in Fig. 2.

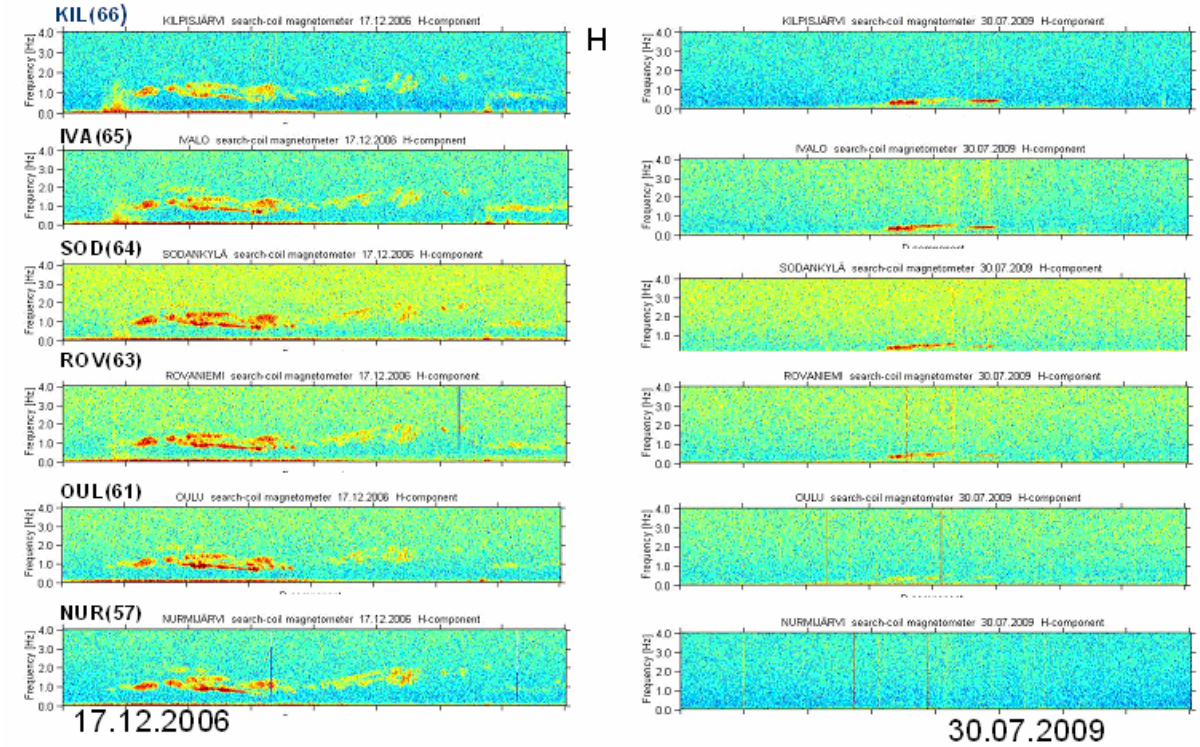

Fig. 2. The spectral structure of Pc1 pulsations under magnetically disturbed period (left panel) and under very quiet condition (right panel). The geomagnetic latitude of stations is shown behind the station cod.

As a rule, during the solar activity minimum, the shape of the frequency-temporal Pc1 spectra looked like a very monochromatic emission of not more 3-5 hours duration with a narrow of the width of the dynamic spectra. During the declining (2006) and increasing (2010) phases of the solar activity, the spectral structure of Pc1 pulsations became more complicated and the duration of the Pc1 series increased up to 10-12 hours. Sometimes it consisted of several varying frequency bands as it was demonstrated at the left panel of Fig. 2.

During the solar minimum (2008, 2009), the Pc1 pulsations are typically observed in the beginning of geomagnetic activity increasing after magnetically quiet (Kp ~ 0-1) periods, and the left-hand polarized pulsations were stronger in SOD (L~5.3) than in NUR (L~3.6), as it is shown in Fig.3. In such condition, the estimated plasmapause could be located according the model www.spaceweather.eu at L~5.0-5.5, thus, in vicinity of SOD station.

During the solar maximum (2003) Pc1 pulsations were observed generally in the recovery phase of magnetic storms and Pc1 waves were stronger in lower latitudes, e.g. in NUR (L~3.6) than in SOD (L~5.3). The examples are presented in Fig. 4. The wave

polarization in NUR was mainly left-handed (L). The estimated plasmapause location could be in the vicinity of NUR station.

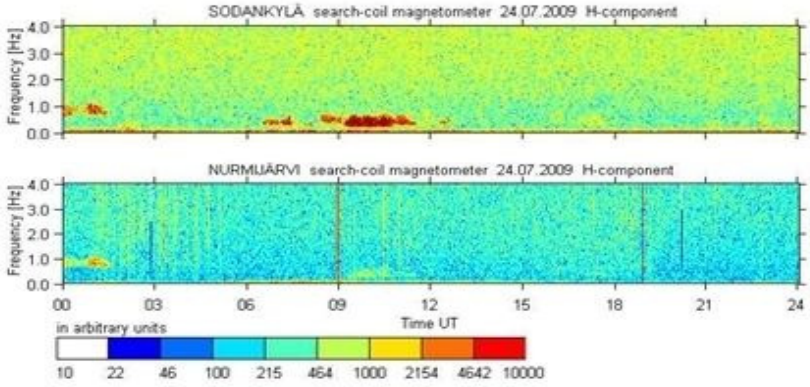

Fig. 3. Spectrograms of Pc1 pulsations in SOD and NUR stations

Discussion

The Pc1 pulsations propagate in the magnetosphere along geomagnetic field lines down to the ionosphere as left-hand polarized electromagnetic (Alfven) waves. Mapping through the ionosphere, these waves are seen on the ground near their footprint as the left polarized mode. Also the maximum of geomagnetic pulsation intensity is located in this region. Thus, the left-hand polarization of ground-based Pc1 indicates this station location in vicinity of Pc1 source footprint.

Right-hand polarized Pc1 waves on the ground could be related to the capture of Alfven waves into the ionospheric waveguide [e.g. Greifinger and Greifinger, 1968] and their convert into the fast magnetosonic ones with the wave polarization change from the left-handed to the right-handed. Another reason of right-hand polarized Pc1 wave appearance could be the availability of the heavy ions (mainly He^+ and O^+) in the magnetospheric plasma, leading to the emergence of so called the tunnel effect and the wave polarization reverse as it was observed, for example, on GEOS spacecraft [Perraut et al., 1984, Mikhailova, 2011]

Summary

The analysis of ground-based Scandinavian data showed:

1. The ground-based Pc1 pulsations (pearls) behavior is controlled by the solar activity level.
2. In the minimum of the solar activity (2008-2009), the shape of the Pc1 dynamic spectra was simple. However, during the declining (2006) and increasing (2010) solar activity stage, the spectral structure of Pc1 became more complicated and the wave duration increases.
3. During the solar minimum, the Pc1 events were stronger at higher latitudes, e.g. at SOD (L~5.3) than at NUR (L~3.5) and the plasmapause was mapped in the vicinity of SOD. The opposite situation was observed during the solar maximum: the Pc1 pulsations were stronger in NUR (L~3.6) than in SOD (L~5.3) and the plasmapause was mapped in the vicinity of NUR.
4. The wave polarization study can give us some additional information about the possible plasmapause location and its temporal dynamics.

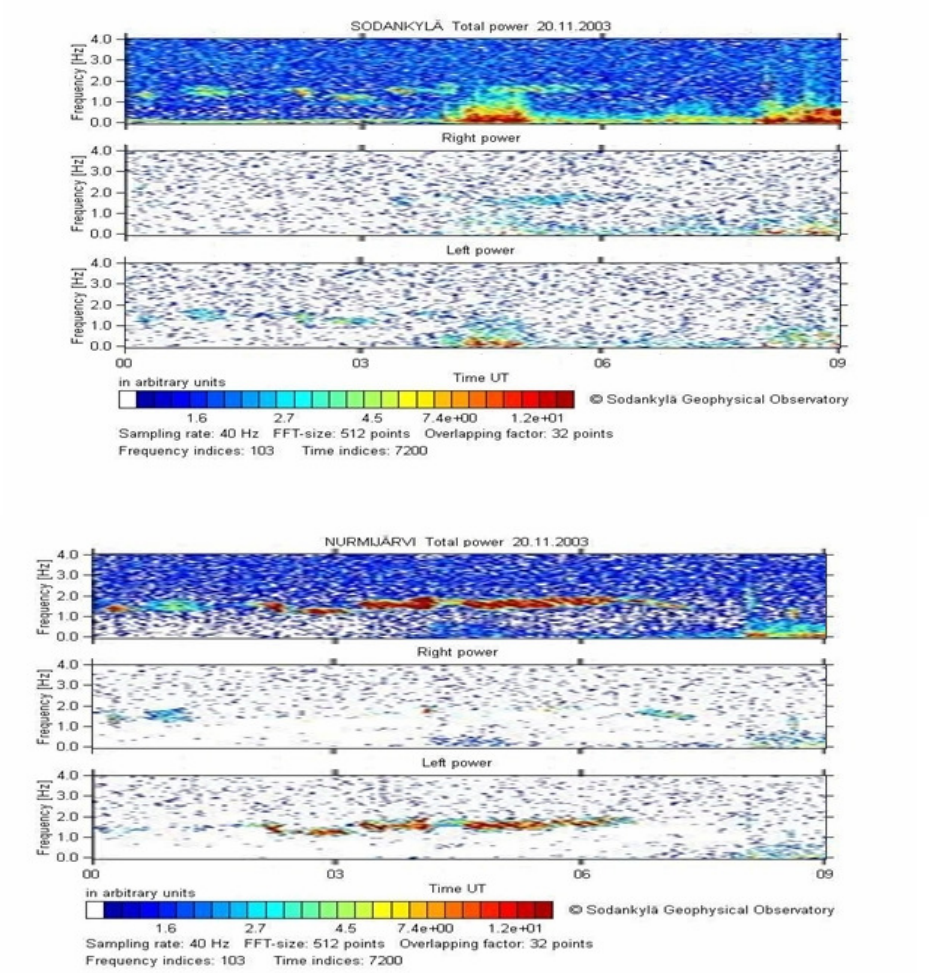

Fig. 4.Spectrograms of Pc1 pulsations in SOD (upper plots) and NUR (bottom plots); from top to bottom: total , right-hand and left-hand intensities.

Acknowledgements. The paper was supported by the Program No 9 of the Presidium of the Russian Academy of Sciences (RAS) and partly by the RFBR Grants № 15-05-07623 (F.F. and Yu.Kh.) and № 13-05-00233 (L.M. and N.K.)

References

Demekhov, A.G. Recent progress in understanding Pc1 pearl formation, *J. Atm. Solar-Terr. Phys.*, 69, 1609-1622, 2007.

Feygin, F.Z, and Yakimenko, V.L. Appearance and development of geomagnetic Pc1 type micropulsations ("pearls") due to cyclotron instability of proton belt, *Ann. Geophys*., 27, 49–55. 1971.

Greifinger, C. and Greifinger, P.S. Theory of hydromagnetic propagation in the ionospheric waveguide, *J. Geophys. Res*., 73, 7473-7490, 1968.

Mikhailova, O.S., On the possibility of localization of waves Pc 1 near ionosphere with the presence of heavy ions in the magnetosphere of the Earth, *Solar-terrestrial physics*, 19, 83-87, 2011.

Kangas, J., Guglielmi, A., and Pokhotelov, O., Morphology and physics of shortperiod magnetic pulsations, *Space Sci. Rev*, 83, 435–512, 1998.

Perraut S., Gendrin R., Roux A., and C. de Villedary. Ion cyclotron waves: direct comparison between ground-based measurements and observations in the source region,*J. Geophys. Res.,* 89 (A1), 195-202, 1984.

Geophysically Induced Currents, a space weather hazard. Case study – Europe under intense geomagnetic storms of the solar cycle 23

Crisan Demetrescu, Venera Dobrica, Cristiana Stefan, Razvan Greculeasa

Institute of Geodynamics, Romanian Academy
E-mail: crisan@geodin.ro

The interaction of the solar wind and heliospheric magnetic field with the magnetosphere and ionosphere results in variations of the geomagnetic field that induce hazardous electric currents in grounded technological systems (electric power and hydrocarbon transportation networks), the so-called GICs. In order to evaluate the hazard induced on the European continent, we present a study of the surface electric field induced by 16 intense (Dst < -150 nT) geomagnetic storms, based on the analysis of the geomagnetic records from the European network of observatories, study that tend to solve the geophysical part of the problem. The evolution during storm development and the sources of the disturbance field are explored in case of the largest geomagnetic storm in the cycle 23 (Dst = -422 nT, November 20-21, 2003), and the geographical distribution of the maximum induced surface geoelectric field over Europe by the 16 storms considered in the study is presented.

Data and method

1-minute values of the northward and eastward geomagnetic elements, recorded at up to 29 European observatories from the INTERMAGNET network during six days encompassing the 16 intense storms of the study (Table 1), were processed to get the time derivative that is driving the induced electric field.

Table 1

Year	Date	Dst (nT)	Year	Date	Dst (nT)
1998	May, 4	-205	2001	Apr, 11	-271
1998	Sep, 25	-207	2001	Nov, 5	-292
1999	Oct, 21	-237	2001	Nov, 24	-221
2000	Apr, 6	-287	2003	Oct, 29	-383
2000	Jul, 15	-301	2003	Nov, 20	-422
2000	Aug, 12	-235	2004	Nov, 7	-374
2000	Sep, 17	-201	2005	May, 15	-247
2001	March, 31	-387	2005	Aug, 24	-184

The induced electric field is assessed according to the method of Viljanen and Pirjola (1989), shortly reviewed in the next lines.

Generally, the horizontal electric field (Ex, Ey) produced by the variable magnetic field is linked to the magnetic field (Bx, By) through the impedance Z(ω) of the underground subject to the plane wave that approximate the propagation of the geomagnetic disturbance.

$$E_x(\omega) = \frac{Z(\omega)}{\mu_0} B_y(\omega), E_y(\omega) = \frac{Z(\omega)}{\mu_0} B_x(\omega)$$

For an Earth viewed as a halfspace with a conductivity σ, the surface electric field is described by

$$E_y(t) = -\frac{1}{\sqrt{\pi \mu_0 \sigma}} \int_{-\infty}^{t} \frac{g_x(u)}{\sqrt{t-u}} du ,$$

where g_x denotes the time derivative of the field B. The integral is converted to a sum that allows to calculate the 1-minute E values. A numerical code was written for the present study.

Two other methods to estimate the geographical distribution ofthe induced geoelectric field in a denser network of points is presently in use (Viljanen et al., 2014; Matandirotya et al., 2014).

Results

The largest storm of the sudy, namely – November 20-21, 2003, Dst = -422 nT – was produced by the interaction of the ICME, illustrated in Fig. 1 by the parameters of the solar wind recorded at the Lagrangean point 1 and available at http://omniweb.gsfc.nasa.gov/, with the magnetosphere. The evolution of the storm is illustrated in the same figure by means of the Dst geomagnetic index.

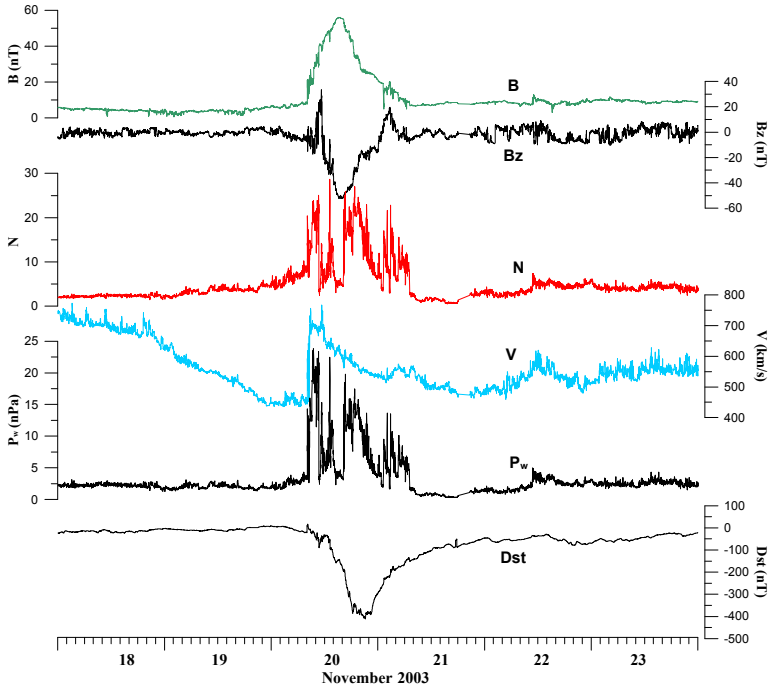

Fig. 1. Solar wind parameters and the Dst evolution for the November 2003 storm

To get an idea on the latitudinal differences that characterize the evolution of the geomagnetic field and of its time derivative, as well as of the induced surface geoelectric field during a geomagnetic storm, we show in Fig. 2 the results obtained for a longitudinal chain of observatories along the 105°E geomagnetic meridian. To show the extreme possible variations, the AL geomagnetic index, showing the disturbed field produced by the ionospheric electrojet at auroral latitude, and the Dst index, showing the disturbed field produced by the magnetospheric ring current at the geomagnetic equator, are plotted on top and, respectively, at the figure bottom.

Examining the figure several conclusions can be underlined, namely:

- the disturbance in Bx is 2-3 times larger at northern latitudes than at mid and southern latitudes;
- during the geomagnetic storm, effects of auroral electrojets superimpose at all latitudes on the disturbance created by the magetospheric ring current;
- the amplitude of the geoelectric field produced by magnetic variations is of the order of hundreths of mV/km in case of SUA (45°N), and of 1-2 mV/km in case of UPS (60°N);
- the more pronounced geoelectric component is directed East-West.

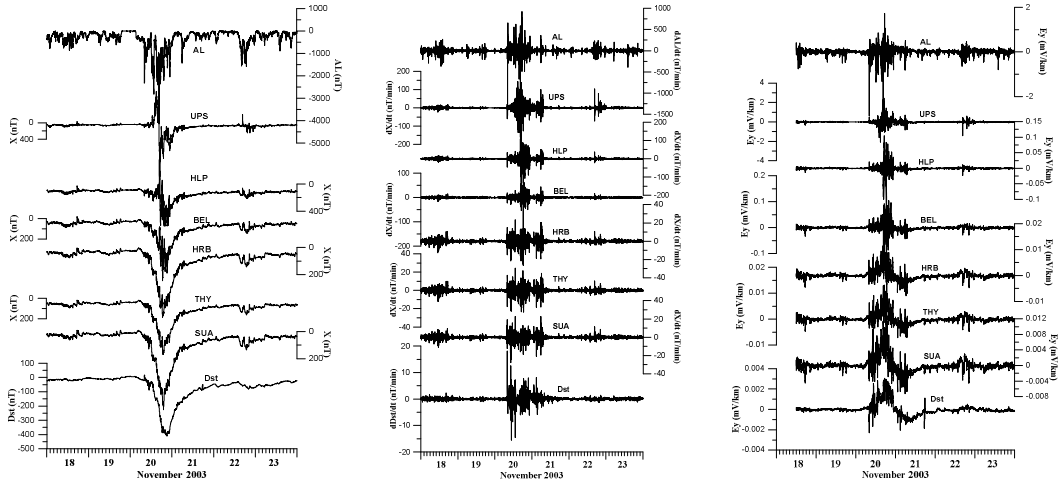

Fig. 2. The geomagnetic disturbance (Bx) (left), its time derivative (middle), and the resulting surface electric field (Ey) (right) for the November 2003 storm, at geomagnetic observatories along the 105°E geomagnetic meridian

As regards the sources of the variations observed, our study indicates both the magnetospheric ring current and the ionospheric auroral electrojet. Fig. 3 shows the geographical distribution of the correlation coefficient between the observed geomagnetic disturbance and the Dst index, while Fig. 4 shows that in case of northern latitude observatories the auroral electrojet and sometimes the magnetopause currents produced by solar wind pressure impulses are a good candidate.

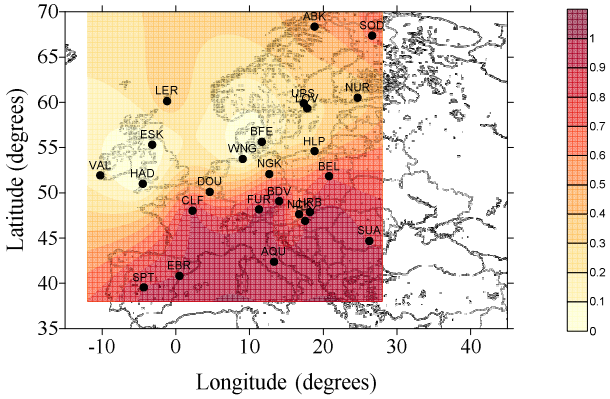

Fig. 3. Correlation coefficient between the Dst index and the horizontal component disturbance at European observatories

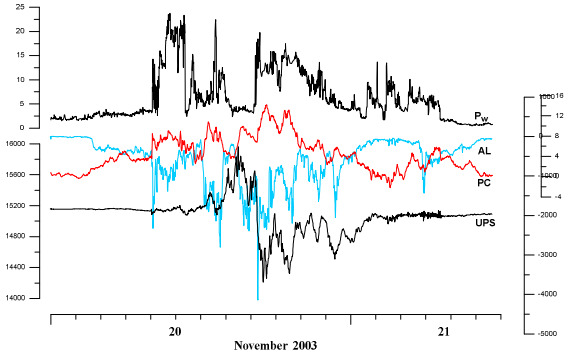

Fig. 4. Evolution of the solar wind dynamic pressure Pw, polar cap currents (PC index), auroral electrojet (AL index), and geomagnetic disturbance at a northern observatory (UPS)

Finally, as a next step in assessing the GIC hazard for the European territory, we calculated the maximum value of the electric field and its orientation at observatories of the network, for each storm considered in this study. Maps are presented in Fig. 5.

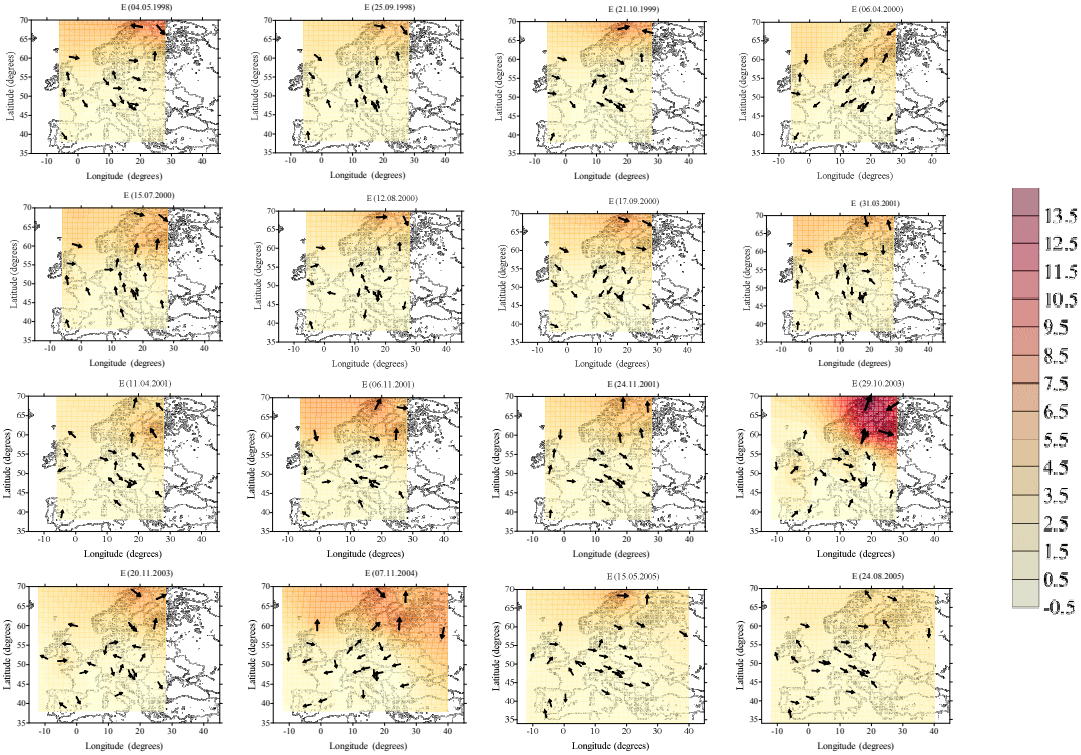

Fig. 5. Maps of the maximum geoelectric field induced at observatories of the European network, for each of the 16 geomagnetic storms of the present study

It is to be noted that the maximum E value is not reached at the same moment at all observatories and its orientation depends on that moment of the storm development. Estimating the actual GICs is an engineering problem and needs knowledge of the power grid.

Instead of conclusion

For future work, we intend to look at local effects and explore the role of magnetopause currents.

Acknowledgements.

The study has been done in the frame of the project CNCSIS – UEFISCDI 93/2011.

References

Matandirotya, E., Cilliers, P. J., Van Zyl, R. R., 2015, Modelling geomagnetically induced currents in the South African power transmission network using the finite element method, Space Weather , doi: 10.1002/2014SW001135.

Viljanen, A. and Pirjola, R., 1989, Statistics on geomagnetically-induced currents in the Finnish 400 kV Power system based on recordings of geomagnetic variations, J. Geomag. Geoelectr., 41, 411-420.

Viljanen, A., Pirjola, R., Pracser, E., Katkalov, J., Wik, M., 2014, Geomagnetically induced currents in Europe, J. Space Weather Space Clim., 4, A09, doi: 10.1051/swsc/2014006.

The Influence of Apr 10, 2001 CME on the Magnetosphere

Diana Beşliu-Ionescu[1], *Marilena Mierla*[2,1], *Georgeta Maris Muntean*[1]

[1] Institute of Geodynamics "Sabba S. Ştefănescu" of the Romanian Academy, Bucharest, Romania
[2] Royal Oservatory of Belgium, Brussels, Belgium
E-mail: diana.ionescu@geodin.ro

Abstract:

Coronal mass ejections (CME) are huge explosions of plasma that could trigger geomagnetic storms. On April 10, 2001 a halo CME was registered by LASCO at 05:30 UT. It was detected into the interplanetary space as an ICME on April 11 at 22:00. The geomagnetic storm associated with this event reached its minimum Dst value one hour later.

We analyse this CME properties and calculate the probability (Srivatsava, 2005) of this (I)CME to have triggered a strong geomagnetic storm. We also investigate the quantity of energy deposited into the magnetosphere during the main phase of this storm using two different formulas by Akasofu (1981) and Wang et al. (2014).

Key words: CME, ICME, geomagnetic storm, energy transfer

1. Introduction

Earth's magnetosphere is the first layer of interaction between solar wind and our technological life. It's form varies with stationary and eruptive phenomena sometimes allowing energetic particles to enter our atmosphere or increase the magnetic field.

Most of the major geomagnetic storms are related to powerful CMEs (e.g. Zhang et al., 2004; Zhao and Webb, 2003), such as the full halo CME from April 10, 2001. The connection between the detection of a CME and the triggering of the geomagnetic storm has been intensively studied (e.g. Gosling, 1993; Gopalswamy et al., 2007). One of the most important property for a CME to be a geo-effective one is its position. This has to be on the Sun's front side and close to the centre.

The prediction of the occurrence of geomagnetic storm is a subject of great interest because of their many side-effects in our lives. There are many methods that scientists use to predict such an event, some pure statistical ones, some of them include modelling and others are pure CME propagation modelling. We chose a semi-empirical model. In order to predict the triggering of intense/super intense geomagnetic storms Srivastava (2005) has implemented a logistic regression model. It combines various CME parameters, to some interplanetary measurements to be correlated with the Dst index.

A very important issue in the occurrence of these storms is the quantity of energy that is transferred from the solar wind to the magnetosphere. We used two different formulas to estimate this energy, that were introduced by Akasofu (1981) and Wang et al. (2014).

We present here the analysis of a CME that was followed by an intense geomagnetic storm, the probability that this CME should have been a geo-effective one and the energy transfer during the following storm.

2. Data Analysis

2.1 CME/ICME

On April 10, 2001 a full halo CME was registered by LASCO at 05:30 UT with a linear speed of 2411 km/s and an acceleration of 211 km/s^2. Its speed at 20 solar radii was 2974 km/s making this CME one of the fastest CMEs of solar cycle 23.

It was triggered by the X2.3 solar flare that started at 05:06 UT, had its maximum at 05:26 and ended at 05:42 UT, in the active region NOAA 9415. This region had an βγδ magnetic classification and it was situated at S22W21. The CME became an interplanetary

coronal mass ejection (ICME) and was registered by ACE on April 11 at 22:00 UT. It was preceded by a sudden concomitant increase in solar wind speed and density. Also the magnitude (B) and the x-component (B_x) of the interplanetary magnetic field had a significant increase.

2.2 Geomagnetic Storm

Figure 1 presents the variation of the Dst index (blue line) along with the magnitude (B) (orange line) and the vertical component of the interplanetary magnetic field (B_z)(green line). The geomagnetic storm associated with the April 10 full halo CME begun with a sudden commencement at 13:43 UT marked by a sudden jump in the Dst time profile of ~20 nT.

This storm's main phase lasted seven hours and, except a small increase around 19:00 UT, it is a smooth decrease to the minimum Dst value of -271 nT at 23:00 UT. The recovery phase lasts a bit more than a day and Dst reaches pre-storm values approximately in the same time as the magnitude of the interplanetary magnetic field (B).

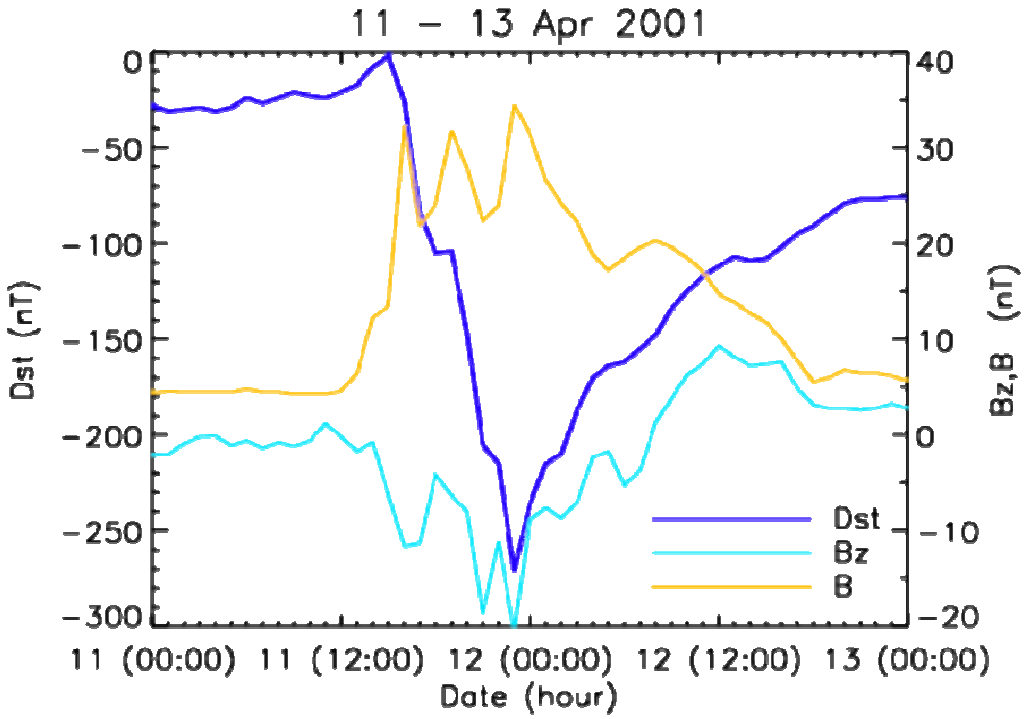

Figure 1: Temporal profiles of Dst, Bz and B during April 11 – 13, 2001

2.3 Probability of the April 10, 2001 CME to have triggered an intense geomagnetic storm

Srivastava (2005) introduced a logistic model to compute the probability of intense and super intense geomagnetic storms to be triggered by CMEs. We modified this model by increasing the number of independent variables from seven to nine, which are now: CME projected speed, acceleration, neutral line orientation, flare importance, position (latitude and longitude), magnetic classification of AR, average magnetic field and the B_z component of the interplanetary magnetic field, and one dependent variable, the Dst index.

The formula introduced by Srivastava (2005) is

$$\Pi = \frac{1}{1 + e^{-Z_i}}, \quad \text{where } Z_i = b_0 + b_1 \times x_{i1} + \ldots + b_j \times x_{ij}$$

where Πi - probability of the occurrence of intense geomagnetic storm given by the i-th observation of the solar variable, b_j (j=0 to J) - model parameters (regression coefficients), x_{ij} (i=0 to I; j=0 to J) - the independent variables. I and J are total number of observations.

In SC23 there were 25 ICMEs to be followed by intense and super-intense geomagnetic storms (-200 nT < Dst < -150 nT, respectively Dst < -200 nT). We have trained the model with 21 events, and used the remaining 4 for validation.

Thus, for April 10, 2001 halo CME we found a 100% probability that this CME should be a geo-effective one.

3. Energy transfer into the magnetosphere

We computed the energy transferred into the magnetosphere during the geomagnetic storm of April 11, 2001 using two different formulas:

the Akasofu empirical parameter (Akasofu, 1981) $\varepsilon = 10^7 V B^2 l_0^2 \sin^4 \frac{\theta}{2}$ [J/s]

and a function obtained by Wang et al. (2013) deducted using a neural network method

$$E_{IN} = 3.78 \times 10^7 n_{SW}^{0.24} V_{SW}^{1.47} B_T^{0.86} (\sin^{2.7} \frac{\theta}{2} + 0.25) \text{ [J/s]}$$

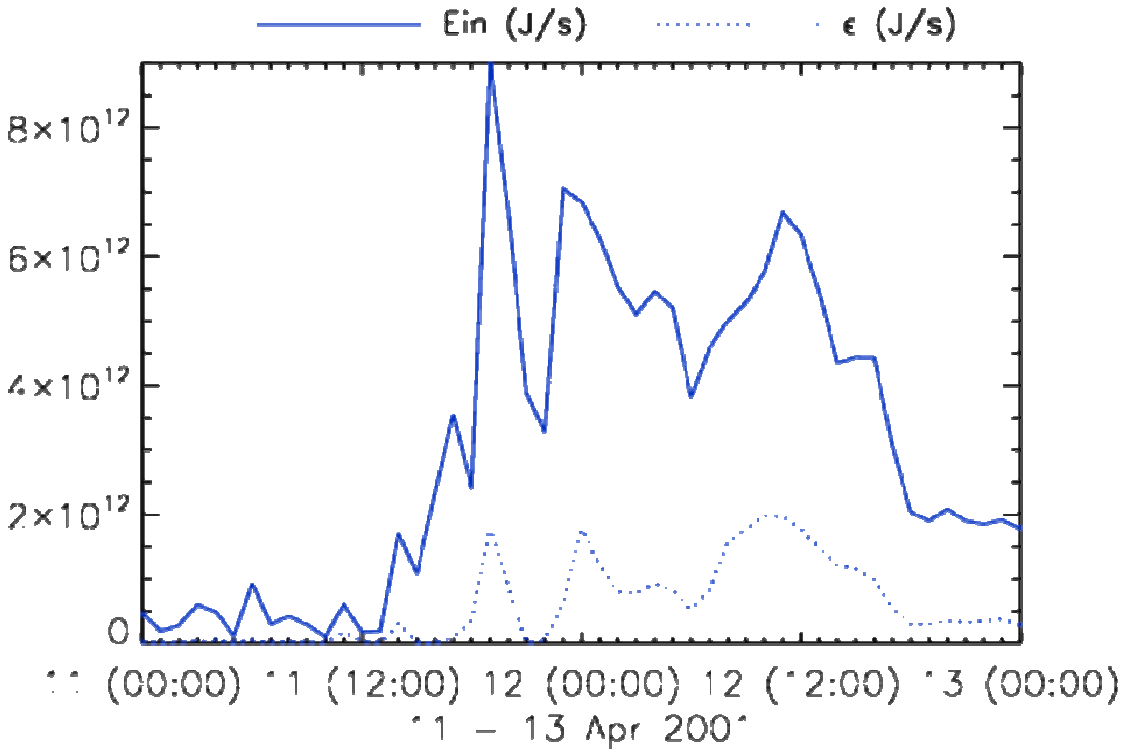

Figure 2: Temporal profiles of ε and EIN during April 11 – 13, 2001

Using the "classical" consideration that the energy is input into the magnetosphere during the main phase of the storm, which in our case is seven hours (Akasofu, 1981), we obtained $W(\varepsilon) = 1.35 \times 10^{17}$ J and $W(E_{IN}) = 1.33 \times 10^{18}$ J. E_{IN} is by one order of magnitude larger than ε, discrepancy that is larger compared to the results obtained by Wang et al. (2014).

Integrating over the entire period that both ε and E_{IN} show a significant increase as compared to a background level – in this case from April 11 at 13:00 UT to April 12 at 18:00 UT – we obtained $W(\varepsilon) = 2.88 \times 10^{18}$ J and $W(E_{IN}) = 1.48 \times 10^{19}$ J.

4. Results and Discussion

We analysed an intense geomagnetic storm that was registered with a minimum Dst on April 11 at 23:00 UT. We presented the characteristics of the triggering coronal mass ejection and its travel towards Earth. We noticed this CME to be situated close to the solar centre. We also analysed the evolution of the geomagnetic storm.

We computed the probability that the April 10, 2001 halo CME should be geo-effective and obtained a 100% certainty.

We noticed that the energy is transferred into the magnetosphere even after the main phase of the geomagnetic storm. We also observed that the two formulas used to calculate this energy transfer have similar temporal profiles, the difference being the magnitude.

Future work should include studying how corrections to the Akasofu parameter change values for the quantity of energy transferred into the magnetosphere.

Acknowledgements:

This research was supported from the CNCSIS project IDEI, No. 93/5.10.2011.

Bibliography

Akasofu, Space Science Reviews, 28, 121-190, 1981
Gopalswamy, N., Yashiro, S., Akiyama, S.: 2007, J. Geophys.Res., 112, A06112
Gosling, J. T., The solar flare myth, J. Geophys. Res., 98, 18937, 1993
Srivatsava, N.: Annales Geophysicae, Volume 23, 2989-2995, 2005
Wang, Y.M., Ye, P.Z., Wang, S., Zhau, G.P., Wang, J., J. Geophys. Res. 107 (A11), 1340, 2002
Wang, G.C., Han, J.P., Li, H., Peng, Z., Richardson, J.D.: J. Geohys. Res., 119, 6199, 2014
Zhang, J., Liemohn, M.W., Kozyra, J.U., Lynch, B.J., Zurbuchen, T.H.: J. Geohys. Res.109, A09101, 2004.
Zhao, X.P., Webb, D.F.: J. Geophys. Res. 108, A6, 2003

Post-Storm High-Latitude Geomagnetic Pc5 Pulsations And Vlf Emissions as A Result of Solar Wind Disturbances

N.G. Kleimenova

Schmidt Institute of the Physics of the Earth RAS, Moscow, Russia
E-mail: kleimen@ifz.ru

Abstract

It is well known that strong solar wind disturbances under southward IMF (Interplanetary Magnetic Field) direction lead to significant space weather violations such as magnetic storms with large geomagnetic activity mainly in the night sector of the auroral latitudes. In the late recovery storm phase, when IMF turns northward and a solar wind energy input stops, the magnetosphere starts to relax, geomagnetic activity drops, but some post-storm effects occur as the different magnetospheric auto-oscillations generation. They get excited mainly in the dayside of the Earth and are observed on the ground. The typical magnetosphere relaxing waves can be the geomagnetic Pc5 pulsations at several minutes period with quasi-monochromatic structure. The main source of these Pc5 pulsations can be the magnetic field line resonance (FLR). Several expressive events of such Pc5 pulsations are shown. The auto-oscillations in the relaxed magnetospheric plasma maser can be observed in the higher frequency band too, namely, as a special regime of the electron-cyclotron instability at several kHz (Very Low Frequency - VLF) emissions, known as quasi-periodic VLF waves. The example of non-typical quasi-periodic picturesque VLF events and their relation with Pc5 pulsations is presented. The trigger of both discussed above processes onset are related with a sudden appearance of some inhomogeneity in the solar wind or IMF.

Introduction

Geomagnetic storms are large disturbances in the Earth's magnetosphere, produced by enhanced solar wind-magnetosphere energy coupling through the magnetic reconnection mechanism. The strong solar wind disturbances under southward Interplanetary Magnetic Field (IMF) direction lead to significant space weather violations with large geomagnetic activity mainly in the night sector of the auroral latitudes. A magnetic storm recovery phase starts with the northward IMF Bz turning and the ring current decay beginning. In this time, solar wind energy input stops, the magnetosphere starts to relax, geomagnetic activity drops, but some post-storm effects occur as the different magnetospheric auto-oscillations generation observed at high latitudes. They get excited mainly in the dayside of the Earth and can be recorded on the ground. Two of them, resonant geomagnetic Pc5 pulsations at frequency range of 1-6 mHz (periods of few minutes) and electromagnetic Very Low Frequency (VLF) emissions at frequency of several kHz, are discussed below.

Geomagnetic pulsations (Pc5 range)

Geomagnetic Pc5 pulsations are typical for storm recovery phase [e.g., Troitskaya et al., 1965; Posch et al., 2003], they exit after ending a last storm main phase substorm (Fig.1). The Pc5 pulsations are attributed to the field line resonances driven by magnetopause shear-flow instability, developing preferentially on the dawn flank. The typical morning Pc5 ground-based pulsations and their spatial geomagnetic latitude (LAT) versus magnetic local time (MLT) distribution are shown in Fig.1. The most likely source for Pc5 pulsations is Kelvin-Helmholtz (KHI) instabilities at the magnetopause generating compressional mode waves that propagate through the magnetosphere and couple to Field Line Resonances (FLR). The cavity mode model [e.g. Samson et al., 1992; Mann et al., 1999] provides a mechanism to convert broadband KHI wave into monochromatic waves corresponded to cavity eigen-frequency. The ability of the cavity to trap waveguide modes as well as KHI exiting is strongly

dependent on the solar wind velocity. Typically, the Pc5 onset generation is caused by an impulse or jump of the solar wind dynamic pressure or an impulsive change in IMF.

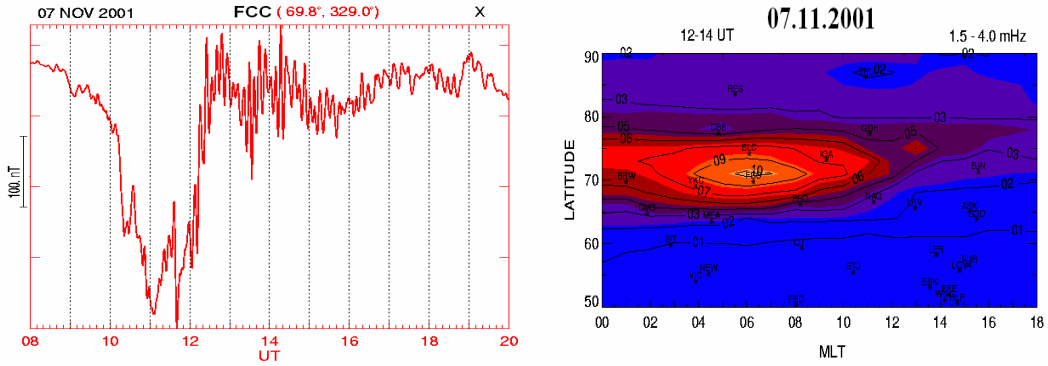

Fig.1. Typical Pc5 geomagnetic pulsations: ground-based magnetogram and LAT-MLT distribution.

The resonant frequency is determined by a field line length, magnetic field strength and the local plasma density. The wave resonant frequency decreases with L-shell increasing. There is an amplitude local peak and phase reversal across the resonant latitude. Such resonant oscillations are usually recorded in high latitudes in the recovery stage of moderate magnetic storms.

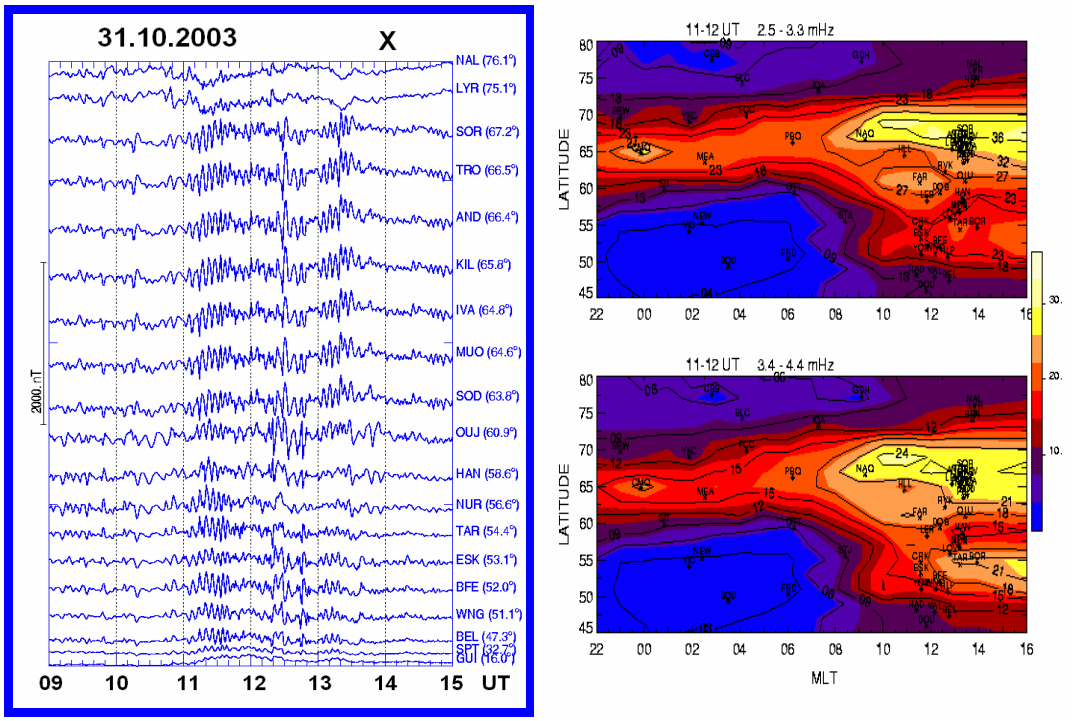

Fig.2. Global Pc5 pulsations in the late recovery phase of the superstorm on 31.10. 2003, magnetograms at different geomagnetic latitudes and LAT-MLT distribution.

After very strong storms and superstorms, caused by huge variations of all solar wind and IMF parameters, the Pc5 pulsations can be observed in global latitude scale (from magnetopause to equator latitudes) [e.g. Kleimenova and Kozyreva, 2007, 2009] sometimes with unusual longitudinal (morning–day) asymmetry. The post-storm intense Pc5 waves can penetrate deep into the inner magnetosphere in the afternoon sector. The nature of these pulsations is still not understand because they do not show a typical local resonance signature. Probably, such post-storm global Pc5 pulsations can be attributed to some eigen-modes of the magneto-hydrodynamic waveguide cavity in the outer magnetosphere due to huge energy stored in the magnetosphere during super storms.

Quasi-periodic VLF-emissions

The auto-oscillations in the relaxed magnetospheric plasma maser can be observed in the higher frequency band too, namely, as a special regime of the whistler mode electron-cyclotron (Very Low Frequency - VLF) emissions at several kHz, known as quasi-periodic (QP) VLF waves (e.g. Manninen et al., 2012, 2013). Note, that typical natural whistler mode electromagnetic emissions (well known as chorus at ~0.5-10 kHz) are generated in the disturbed magnetosphere and do not observed under quiet geomagnetic conditions. The example of typical post-storm QP emissions, observed near high-latitude Scandinavian obs. Sodankyla (SOD), is shown in Fig.3. Such emissions observed more frequently in winter due to better VLF wave reflection from the opposite (summer) hemisphere.

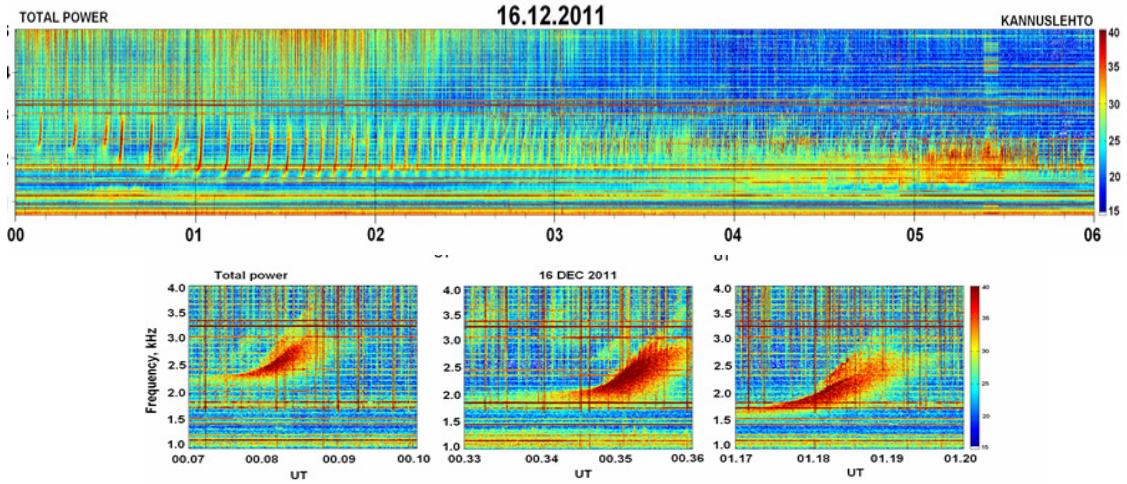

Fig.3. Example of post-storm high-latitude QP emissions: upper panel – 6 hours duration event, bottom one - the 3-min successive intervals of this event.

There is no complete theory, which could adequately explain the observed QP emissions generation. Nevertheless, it is possible to interpret these QP emissions by applying the theory of the auto-oscillation regimes of the cyclotron instability in the magnetospheric plasma maser [Bespalov, 1982; Bespalov and Trakhtengerts, 1986]. According to this theory the primary reason of QP emissions is the auto-oscillations of the radiation belt electrons that correspond to periodic processes of accumulation of energetic particles in the radiation belts and their precipitation into the ionosphere during the electromagnetic emission bursts. The excitation of these oscillations is possible only during low geomagnetic activity. However, one of the necessary conditions for such processes is a transport in the magnetosphere an addition energetic electrons caused by some irregularities in the solar wind and IMF, which usually are observed in that time. The interaction of Pc5 geomagnetic pulsations and hiss VLF emissions is shown in fig.4 and 5. The strange "mushroom" like shape of spectral-temporal VLF hiss variation was observed in the late recovery phase of magnetic storm on 12 December 2013. The cut-off near 2 kHz is a result of the wave propagation in the ionosphere waveguide.

Summary

In the magnetic storm recovery phase, when the solar wind energy input stops, and the magnetosphere starts to relax, the post-storm effects are observed at high latitudes in the dayside as some magnetospheric auto-oscillations such as resonant geomagnetic Pc5 pulsations at frequency range of 1-6 mHz (periods of few minutes) and electromagnetic QP VLF emissions at frequency of several kHz.

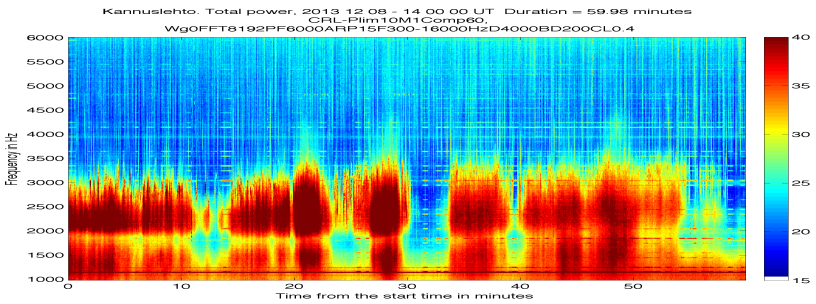

Fig. 4. VLF "mushrooms" at 1-3 kHz at SOD in the storm recovery phase on 08.12.2013.

However, the sequence of individual "mushrooms" could be a result of the modulation of the grow rate of the electron-cyclotron instability by simultaneous resonant Pc5 pulsations (Fig.5). It is seen that each negative Pc5 deviations coincides with a burst of VLF emissions.

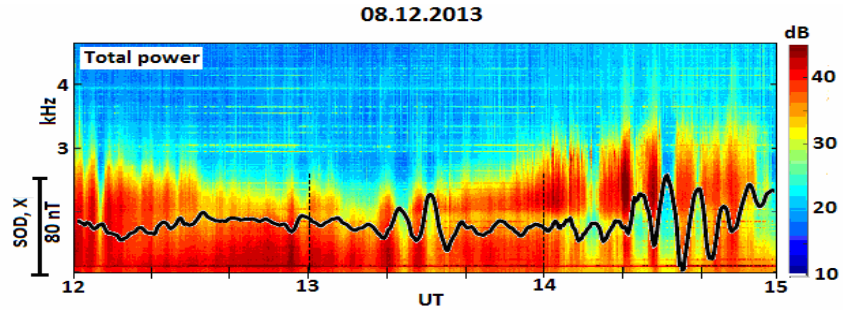

Fig. 5. Modulation of VLFemissions by Pc5 geomagnetic pulsations (black curve).

Acknowledgements. The paper was supported by the RFBR Grants № 13-05-00233 and partly by the Program No 9 of the Presidium of the Russian Academy of Sciences (RAS).

Referances

Bespalov, P.A., Self-excitation of periodic cyclotron instability regimes in a plasma magnetic trap, Physica Scripta, 2/2, 575-579, 1982.

Bespalov, P.A. and Trakhtengerts, V.YuThe cyclotron instability in the Earth radiation belts, Rev. Plasma Physics, 10, 155-292, 1986.

Kleimenova, N.G. and Kozyreva, O.V., Daytime Quasi-periodic geomagnetic pulsations during the recovery phase of the strong magnetic storm of May 15, 2005, Geomagnetism and Aeronomy, 47 (5), 580-587, 2007.

Kleimenova, N.G. and Kozyreva, O.V., Penetration of Pc5 geomagnetic pulsations to unusually low latitudes during the recovery phase of the super-strong magnetic storm of October 31, 2003, Geomagnetism and Aeronomy, 49 (8), 1199–1203, 2009.

Mann, I.R., Wright, A.N., Mills, K.J., and Nakariakov, V.M., Excitation of magnetospheric waveguide modes by magnetosheath flows, J. Geophys. Res., 104, 333-353, 1999.

Manninen, J., Kleimenova, N.G., and Kozyreva, O.V., New type of ensemble of quasi-periodic, long-lasting VLF emissions at the auroral zone, Ann. Geophys., 30, 1655–1660, 2012.

Manninen, J., Kleimenova, N.G., Kozyreva, O.V., Bespalov, P.A., and Kozlovsky, A.E., Non-typical ground-based quasi-periodic VLF emissions observed at L~5.3 under quiet geomagnetic conditions at night, J. Atmos. Solar-Terr. Phys., 99, 123-128, 2013.

Posch, J.L., Engebretson, M.J., Pilipenko, V.A., Hughes, W.J., Russell, C.T., and Lanzerotti, L.J. Characterizing the long-period ULF response to magnetic storms, J. Geophys. Res., 108(A1), 1029, doi:10.1029/2002JA009386, 2003.

Samson, J.C., Harrold, B.G, Ruohoniemi, J.M., Greenwald, R.A., and Walker, A.D.M. Field line resonances associated with MHD waveguides in the magnetosphere, Geophys. Res. Lett. 19, 19441-19444, 1992.

Troitskaya V.A., Melnikova M.V., Bolshakova O.V., Rokityanskaya D.A., Bulatova G.A. Magnetic storms fine structure // Ann. USSR Acad. Sci., Earth physics, 6, 82-86, 1965.

Comparison of substorms during two solar cycles maximum: (1999-2000 and 2012-2013)

I.V. Despirak[1], *A.A. Lubchich*[1], *N.G. Kleimenova*[2]

[1] Polar Geophysical Institute RAS, Apatity, 184209, Russia
[2] Schmidt Institute of the Earth Physics RAS, Moscow, Russia
E-mail: despirak@gmail.com

Abstract:

We presented the comparative analysis of the substorm behavior in the periods of two solar cycles maximum. The substorms, observed during the large solar cycle maximum (1999- 2000, with Wp> 100) and during the last maximum (2012-2013 with Wp~60), were studied. All considered substorms were divided into 3 types according to auroral oval dynamic. First type - substorms which observed only in auroral latitudes ("usual" substorms); second type - substorms which propagate from auroral latitudes (<70º) to polar geomagnetic latitudes (>70º) ("expanded" substorms, according to expanded oval); third type is substorms which observed only at latitudes above ~70º in the absence of simultaneous geomagnetic disturbances below 70° ("polar" substorms, according to contracted oval). Our analysis was based on the 10-s sampled IMAGE magnetometers data, the 1-min sampled OMNI solar wind and interplanetary magnetic field (IMF) data. There were analyzed above 1700 events of "expanded", "polar" and "usual" substorms in 1999- 2000 and in 2012-2013 years. The following substorm characteristics have been studied: (i) the seasonal variations of substorms, (ii) the substorm onset latitude, (iii) the maximal reaching latitude, (iiii) latitudinal range of all three types of substorms. We compare these substorms characteristics and the solar wind conditions observed before substorm onsets.

Introduction

Magnetospheric substorms have long been in the focus of solar□terrestrial physics; however, up to now they still represent an outstanding unresolved problem. In this paper we studied substorms during the large solar cycle maximum (1999- 2000, with Wp> 100) and during the last maximum (2012-2013 with Wp~60). Namely, we present a comparative analysis of some substorms characteristics and the solar wind conditions observed before substorm onsets.

It is noted that although the history of the study substorms is very long, there are only a few large statistical studies of substorms (Borovsky et al., 1993; Tanskanen et al., 2002, 2005; Newell et al., 2001; Frey et al., 2004). Newell et al., 2001 determined 390 substorms events from POLAR UVI, Frey et al., 2004 found more than 2400 substorm events from IMAGE FUV instrument, Tanskanen et al, 2002, 2005 identified more 5000 substorm events from IMAGE magnetometers network. Traditionally, researchers have been considered all substorms. In our work we divided all observed substorms into 3 groups according auroral dynamics. It is known that under normal conditions (moderate disturbance) the auroral oval is located at geomagnetic latitudes about 65-67° ("normal oval"), under quiet conditions (at B_Z>0) the auroral oval shrinks and moves to higher latitudes (>70°GLAT, "contracted oval"), and in disturbed conditions, at increased magnitude of the IMF negative B_Z component, the equatorward boundary of the oval is shifted down to 50° geomagnetic latitude, while its poleward boundary extends to higher latitudes ("expanded oval") (Feldstein and Starkov, 1967). Thus, in our terminology, we call the first type of substorms as "usual" substorms-substorms which observed only in auroral latitudes. Similarly as the auroral oval is called an "expanded" oval, meaning its extension in the disturbed conditions, we will call "expanded" substorms those which start in the auroral zone and then propagate to very high latitudes. We point out that in the maximum phase of "expanded" substorms, the westward electrojet can be

observed at very high geomagnetic latitudes (> 75º) (Despirak et al., 2008). The third type of substorms, we term as "polar" substorms, according to contracted oval. They represent the isolated bay-like magnetic disturbances, observed at geomagnetic latitudes higher than the location of the typical polarward boundary of the auroral oval (> 70° GLAT) and not accompanied or preceded by substorm activity at auroral latitudes.

The aim of this work is the comparison of some substorm characteristics of all three types of substorms and the solar wind conditions observed before substorm onsets during two solar cycles maximum: (1999-2000 and 2012-2013).

Data

We used the magnetic data of the IMAGE meridional chain Nurmijarvi - Ny Alesund, from 57º to 75º of geomagnetic latitudes. The solar wind and Interplanetary Magnetic Field parameters measured by Wind spacecraft were taken from OMNI database. The 1999-2000 and 2012-2013 time intervals, close to two different maximums of the solar activity are used. There were analyzed above 1700 events of "expanded", "polar" and "usual" substorms in 1999- 2000 and in 2012-2013 years.

Results

a) Seasonal variations of substorm number

We calculated the seasonal variations of substorms, observed in two different periods – in 1999-2000 years and in 2012-2013 years. Figure 1 presents the results for 4 different types of substorms: A- all substorms; U- classical (usual) substorms; P- polar substorms; E-expanded substorms.

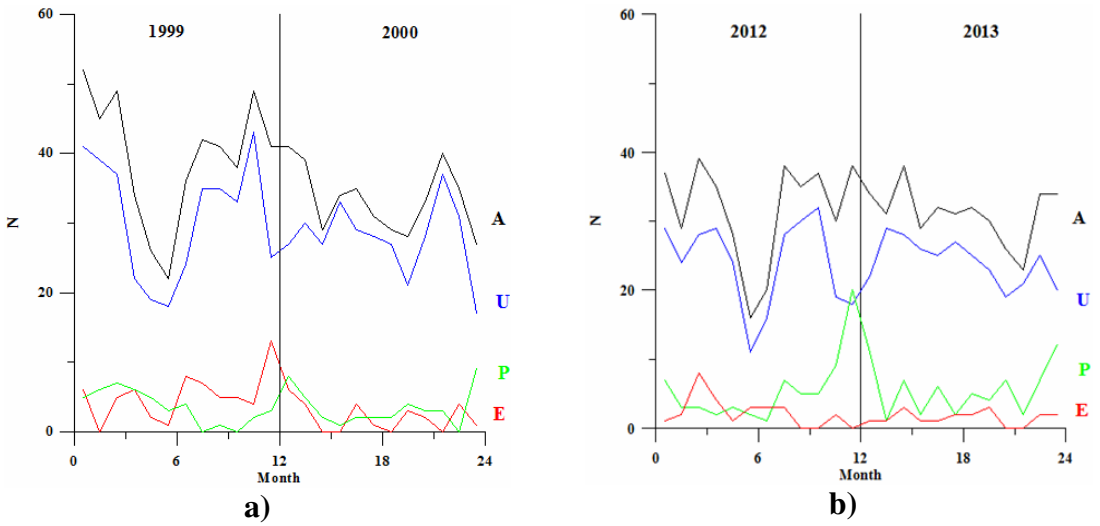

Fig. 1 The results of seasonal variations of substorms during two solar cycle maximums – a)- in 1999-2000 years ; b) – in 2012-2013 years

It is seen that number of substorms is higher during 1999-2000 periods than during 2012-2013 periods; summer minimums of substorms number and spring and autumn maximums are common to both periods; polar substorms behavior was in opposition to other types of substorms. Number of polar substorms have maximum in the winter months; wherein it is noted that expanded substorms maximum was observed in winter 1999-2000, but not observed in winter 2012-2013.

b) the substorm onset latitude and the maximal reaching latitude

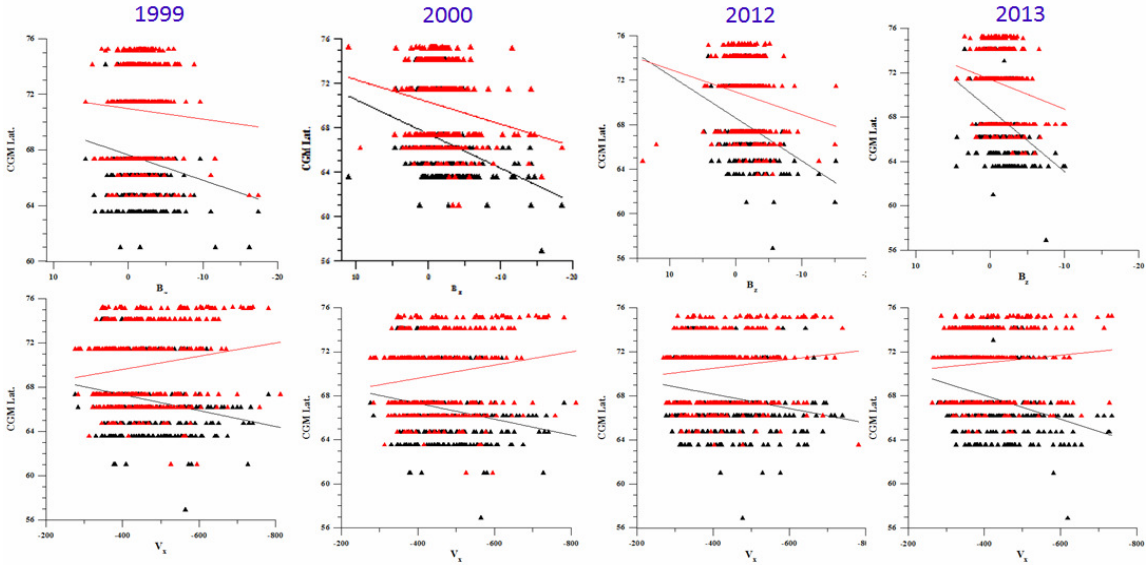

Fig. 2 Substorm onset and maximal reaching latitudes for all substorms during 1999, 2000, 2012 and 2013 periods in dependence on solar wind velosity (V_X) and B_Z component of IMF

c) Solar wind and IMF parameters before substorms onsets

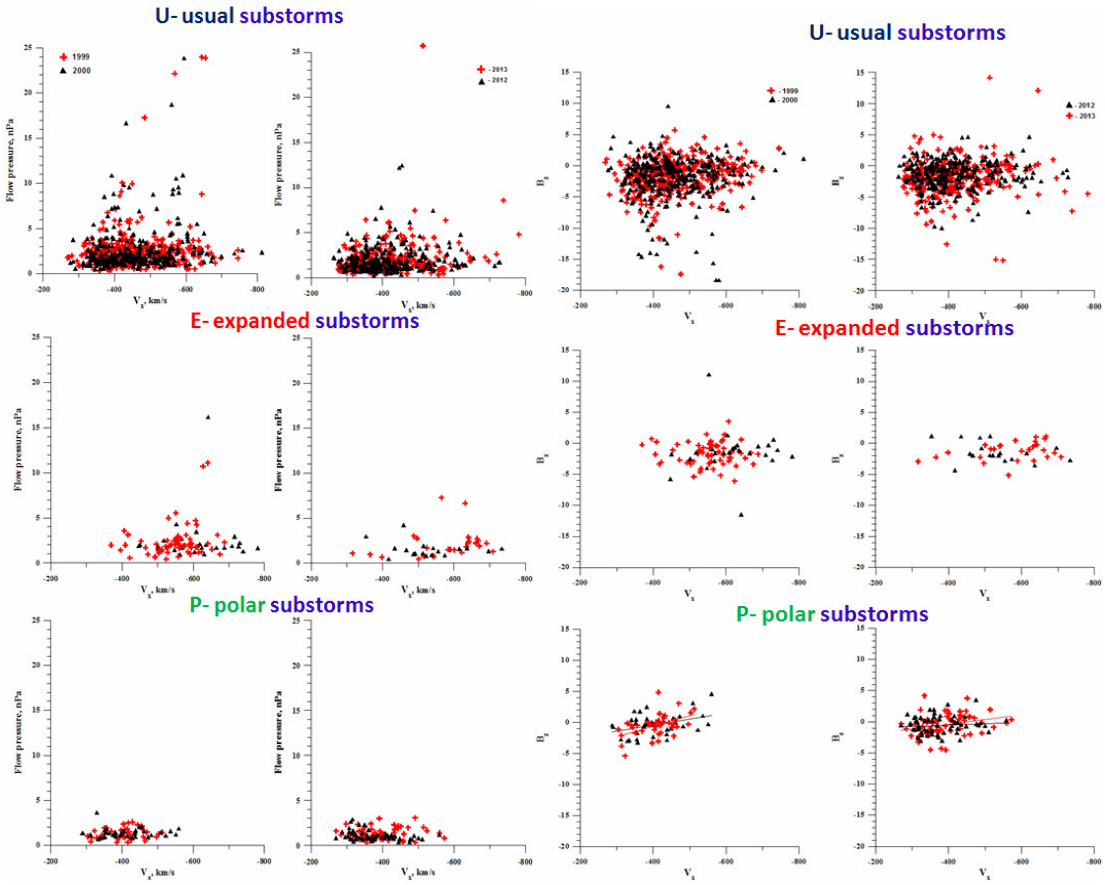

Fig. 3 Parameters of the solar wind and the IMF (B_Z, V_X and P) before substorms onsets for 1999-2000 (left columns) and for 2012-2013 (right columns)

It is shown that significant differences in dependencies on the solar wind parameters (Vx, Bz, P, N, T) between substorms in 1999-2000 and substorms in 2012-2013 not found.

Conclusions

It is shown that:

1. Number of substorms is higher during 1999-2000 periods than during 2012-2013 periods; summer minimums of substorms number and spring and autumn maximums are common to both periods; polar substorms behavior was in opposition to other types of substorms. Number of polar substorms have maximum in the winter months; wherein it is noted that expanded substorms maximum was observed in winter 1999-2000, but not observed in winter 2012-2013.
2. Substorms onset latitudes for 1999-2000 years were a little lower that onset latitudes for 2012-2013 years; the latitudinal sizes of substorms in 1999-2000 years were a little more than the latituinal size of substorms during 2012-2013 years.

Acknowledgment This study was supported by Program No 9 of the Presidium of the RAS. The study is part of a joint Russian - Bulgarian Project 1.2.10 of PGI RAS and IKIT-BAS under the Fundamental Space Research Program between RAS and BAS.

References

Borovsky J.E., R.J. Nemzek, R.D. Belian (1993), The occurrence rate of magnetospheric-substorm onsets: Random and periodic substorms, *J.Geophys.Res*., 105, 3807-3813.

Tanskanen E., T.I. Pulkkinen, H.E.J. Koskinen, J.A. Slavin (2002), Substorm energy budget during low and high solar activity: 1997 and 1999 compared, *J.Geophys.Res*., 107, 1086, doi:10.1029/2001JA900153.

Tanskanen E.I., J.A. Slavin, A.J. Tanskanen, A. Viljanen, T.I. Pulkkinen, , H.E.J. Koskinen, A. Pulkkinen, J. Eastwood (2005), Magnetospheric substorms and strongly modulated by interplanetary high-speed streams, *Geophys. Res. Lett*., 32, L16104, doi:10.1029/2005GL023318.

Newell P.T., K. Liou, T. Sotirelis, C.-I. Meng (2001), Auroral precipitation power during substorms: A Polar UV Imager-based superposed epox analisys, *J.Geophys.Res*., 106, 28885-28896.

Frey H.U, S.B. Mende, V. Angelopoulos, E.F. Donovan (2004), Substorm onset observations by IMAGE-FUV, *J.Geophys.Res*., 109, A10304, doi:10.1029/2004JA010607.

Feldstein, Y.L. and G.V. Starkov (1967), Dynamics of auroral belt and geomagnetic disturbances. *Planet. Space Sci*., 15, 209-229.

Despirak, I.V., A.A. Lyubchich, Kh.K. Birnat, A.G. Yakhnin (2008), Poleward expansion of the westward electrojet depending on the solar wind and IMF parameters. *Geomagn. Aeron.*, 48, no. 3, 284-292.

Substorms observations during two strongly disturbed periods - in March 2012 and March 2015

V. Guineva[1], *I.V. Despirak*[2], *B.V. Kozelov*[2]

[1] Space Research and Technology Institute (SRTI), BAS,
Stara Zagora Department, Stara Zagora, Bulgaria
[2] Polar Geophysical Institute (PGI), Apatity, Russia
E-mail: v_guineva@yahoo.com

Abstract.

In this work two events of strong geomagnetic activity were examined: the period 7-17 March 2012, which is one of the most disturbed periods during the ascending phase of Solar Cycle 24, and the severe geomagnetic storm on 17-20 March 2015. During the first period four consecutive magnetic storms occurred on 7, 9, 12, and 15 March. These storms were caused by Sheath, MC and HSS, and the detailed scenarios for the storms were different. The second event is a storm of fourth level with Kp = 8, the strongest one during the last four years. A geomagnetic storm of such intensity was observed in September 2011. Since then, the level of Kp never exceeded the value 7. Object of our study were the substorms registered during these periods. Observations of the Multiscale Aurora Imaging Network (MAIN) in Apatity have been used. The substorm developments during different storms were compared. Solar wind and interplanetary magnetic field parameters were taken from OMNI data base. Substorm onset time and the subsequent development were verified by data of IMAGE magnetometers network and by data of the all-sky cameras at Apatity. The particularities in the behaviours of substorms connected with different storms during these two interesting strongly disturbed periods are discussed.

Introduction.

It is known that magnetic storms are generated by certain types of solar wind, mainly interplanetary coronal mass ejections (ICME) including Sheath- region ahead and body of ICME (magnetic cloud (MC), and Corotating Ineraction Regions (CIR) between recurrent streams and slower streams (e.g. Gonzales et al., 1990; Tsurutani et al., 2006, Balogh et al., 1999, Burlaga et al., 1982). During solar maxima, most common are the sporadic flows associated with CME (Webb and Howard, 1994), respectively MC (e.g. Burlaga et al., 1982). Recurrent streams and their CIR are more frequent during solar minima. It should be noted that there are differences between storms generated by Sheath, MC and CIR (in intensity, recovery phase duration, etc.) (e.g., Huttunen et al., 2006; Pulkkinen et al., 2007; Yermolaev and Yermolaev, 2006). However there are more complicated storm cases, when the magnetic storms are caused by several sources in the solar wind, coming consecutively one after the other or partly overlapping. Events of strong geomagnetic activity are of special interest because magnetic storms can affect the energetic systems, the space crafts or the ground based systems. That's why coordinated actions of the scientific community are needed to perform and gather observations, to create models of the whole chain of phenomena from the Sun to the Earth in order to make successful predictions of space weather and to prevent failures in the technologic infrastructure by reason of strong geomagnetic storms (Schrijver et al., 2015). Storms are the final effect of the enhanced solar and interplanetary activity. So, it is important to have more observations of substorms during storms, especially under strongly disturbed conditions.

In this paper, two periods of high geomagnetic activity are examined and the observed substorms were studied.

Instrumentation and data used.

Measurements from the Multiscale Aurora Imaging Network (MAIN) in Apatity during two strongly disturbed periods in March 2012 and March 2015 have been used. The all-sky cameras observational system has being built in Apatity since 2008. The cameras characteristics, their mutual situation and the measurement process are described in detail by Kozelov et al. (2012).

Solar wind and interplanetary magnetic field parameters were taken from OMNI data base (http://sdaweb.gsfc.nasa.gov/cdaweb/istp_public/). Kp indices were taken from NOAA database: http://www.ngdc.noaa.gov/stp/GEOMAG/kp_ap.html.

Substorm presence was verified by ground-based data of IMAGE magnetometers network (using meridional chains).

To study the substorm development data from the Apatity all-sky camera (images and keograms) and the Guppy F-044C (GC) camera with field of view ~67° (keograms) were used.

Overview of the interplanetary conditions.

Two time intervals of strong geomagnetic activity were examined: 7-17 March 2012 and 17-20 March 2015.

The time interval 7 – 17 March 2012 (11 days) is one of the first major geomagnetically active periods of the ascending phase of SC24 (Tsurutani et al., 2014). It was examined and the detected features were described (Valchuk, 2013; Tsurutani et al., 2014). Magnetic storms occurred on 7, 9, 12, and 15 March, these are called the S1, S2, S3, and S4 events. These storms were caused by Sheath, MC and HSS, the detailed scenario for all four storms were different.

On 17 March 2015, St Patrick's day, a severe geomagnetic storm (G4) occurred. It was the result of a pair of CME's which left the Sun on 15 March, maybe unexpectedly combined spreading towards Earth and formed a large shock front crossing the Earth orbit. In 4:45 UT the shock wave formed by the CME swept past our planet and a geomagnetic sudden impulse was registered. It coincides with the storm sudden commencement when Dst jumped from 16 to 66 nT. A Magnetic cloud passed the Earth and just after it a HSS superposed and contributed to the storm duration. Dst reached the value -235 nT in 22:47 UT. An overview of the interplanetary conditions during both examined periods is presented in Fig.1.

Results.

The measurements during the periods 7-17 March 2012 and 17-20 March 2015 were examined together with the interplanetary conditions during the measuring periods. 18 substorms were identified over Apatity under clear sky conditions: 10 of them developed during the first period and 8 – during the second one. Three typical cases of substorms were chosen presenting a substorm generated during the main storm phase, a substorm during the recovery phase in the vicinity of the maximal development and a substorm during the late recovery phase.

Case 1. 17 March 2015.

The substorm occurred during the main phase of the severe geomagnetic storm on the same day. Dst was -163 nT. The substorm development is presented in Fig.2 by chosen images of the all-sky camera. The world directions are shown on the first image. UT is written above the images. The substorm was first seen from Apatity in 17:36:40 UT to the South of the station. For some minutes auroras stayed in the South part of the field of view. In 17:42 UT a fast motion towards North was observed and in 17:45:30 UT the auroras occupied the whole field of view.

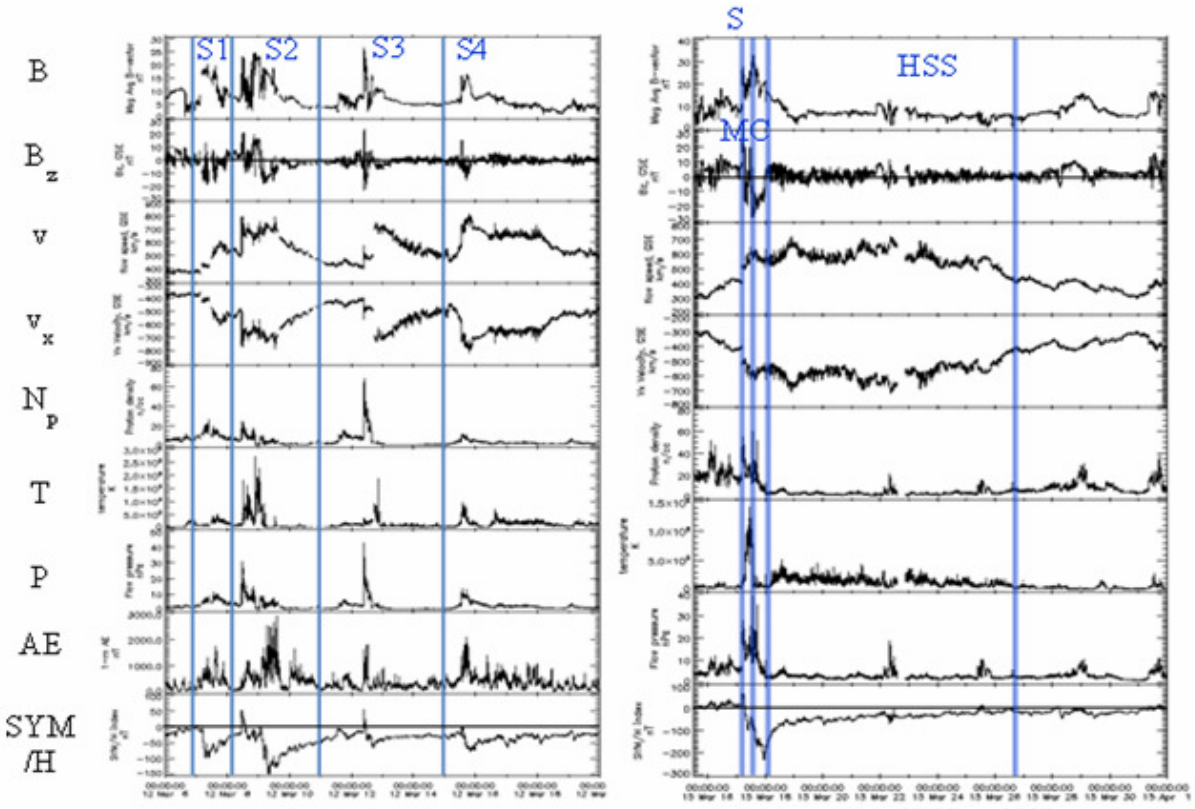

Fig.1. Overview of the interplanetary conditions during the time periods 7-20 March 2012 (to the left) and 16-30 March 2015 (to the right).

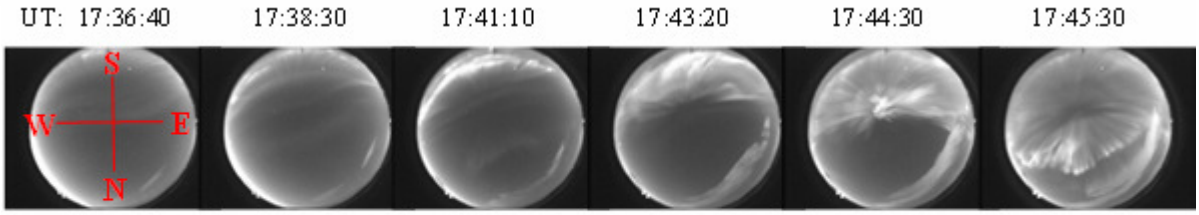

Fig.2. Development of the substorm on 17 March 2015 in 17:36:40 by selected all-sky camera images.

Case 2. 7 March 2012.

The substorm began during the first event of the disturbed interval 7-17 March 2012 during a storm with Dstmin = -98 nT caused by the southward directed sheath fields. In Fig.3. selected images of the all-sky camera are shown. The format is the same as in Fig.2. The substorm developed during the recovery phase of the storm, near the maximal storm development. Dst was -45 nT. Subtsorm auroras appeared in the South part of the field of view in 18:45 UT. The auroras moved towards North, reached zenith in about 18:53 UT and after that auroras surpassed it.

Case 3. 10 March 2012.

The substorm developed during the second event of the disturbed period 7-17 March 2012, when a geomagnetic storm was generated by a MC. Dstmin reached -148 nT. The

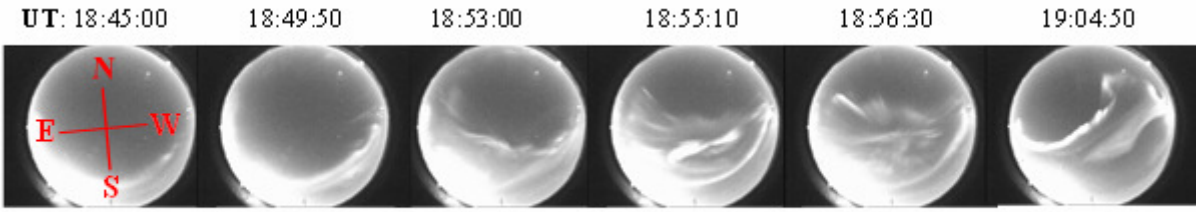

Fig.3. The substorm on 7 March 2012 by all-sky images.

substorm occured in the late recovery phase, Dst was -50 nT. The substorm behavior is presented in Fig.4. The format is the same as in Fig.2. The substorm onset over Apatity was in 18:35:50 UT on 10.03.2012 to the North of the station. The aurora traveled to South, reached zenith in 18:39 UT and moved further to South.

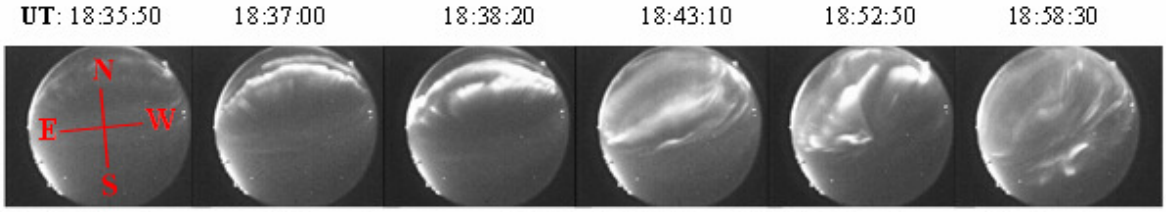

Fig.4. Development of the substorm on 10 March 2012 in 18:35:50 by chosen all-sky images.

Conclusions

It is shown that:

1. Substorms, originated during the main storm phase or near the Dst minimum in the recovery phase, occurred to the South of Apatity, and substorm auroras expanded in North direction;
2. For substorms during the recovery phase or the late recovery phase, auroras were observed near the station zenith or to the North of the Apatity station, and their motion from North to South was registered.

Acknowledgment: This study was supported by Program No 9 of the Presidium of RAS. The study is part of a joint Russian - Bulgarian Project 1.2.10 of PGI RAS and IKIT-BAS under the Fundamental Space Research Program between RAS and BAS.

References:

Balogh A., J.T. Gosling, J.R. Jokipii, R. Kallenbach, H. Kunow (1999), *Space Sci. Rev*., 89, 141-411.

Burlaga L.F., L.F. Klein, L. Sheeley, N.R. Michels, D.J. Howard, R.A. Koomen, M.J. Schwenn, H. Rosenbauer (1982), *Geophys. Res. Lett.* 9, 1317-1320.

Gonzalez W.D., A.L.C. Gonzalez, B.T. Tsurutani (1990), *Planet. Space Sci*. 38, 181-187.

Huttunen K.E.J., H.E.J. Koskinen, A. Karinen, K. Mursula (2006), *Geophys. Res. Lett.* 33, L06107, doi:10.1029/2005GL024894.

Kozelov, B.V., S.V. Pilgaev, L.P. Borovkov, V.E. Yurov (2012), *Geosci. Insrum. Method. Data Syst.*, 1, 1-6,

Pulkkinen T.I., N.Y. Ganushkina, E.I. Tanskanen, M. Kubyshkina, G.D. Reeves, M.F. Thomsen, C.T. Russel, H.J. Singer, J.A. Slavin, J. Gjerloev (2006), *J. Geophys. Res.* 111, A11S17, doi:10.1029/2006JA011627.

Schrijver C.J. et al. (2015), *Adv. Space Res*., 55, 2745-2807

Yermolaev Yu.I., M.Yu. Yermolaev (2006), *Adv. Space Res.* 37, 1175-1181.

Tsurutani B.T., W.D. Gonzalez, A.L.C. Gonzalez, F.L. Guarnieri, N. Gopalswamy, M. Grande, Y. Kamide, Y. Kasahara, G. Lu, I. Mann, R. McPherron, F. Soraas, V. Vasyliunas (2006), *J. Geophys. Res.* 111, A07S01, doi:10.1029/2005JA011273.

Tsurutani B.T., E. Echer, K.Shibata, O.P. Verkhoglyadova, A.J. Mannucci, W.D. Gonzalez, J.U. Kozyra, M. Pätzold (2014), *J. Space Weather Space Clim*., 4, A02, DOI: 10.1051/swsc/2013056

Valchuk T.E., (2013), Astron. Tsirkulyar, N1585, ISSN 0236-2457

Webb D.F., R.A. Howard (1994), *J. Geophys. Res.* 99, 4201-4220.

Development of a Greek solar map based on solar model estimations*

Harry D. Kambezidis[1], *Basil E. Psiloglou*[1], *Kosmas A. Kavadias*[2], *Athanasios G. Paliatsos*[3], *Aristides Bartzokas*[4]

[1]Atmospheric Research Team, Institute of Environmental Research and Sustainable Development, National Observatory of Athens, Greece
[2]Laboratory of Soft Energy Applications & Environmental Protection, TEI of Piraeus, Greece
[3]Laboratory of Environmental Technology, Electronic Computer Systems Engineering Department, TEI of Piraeus, Greece
[4]Laboratory of Meteorology, Department of Physics, University of Ioannina, Greece
E-mail: harry@noa.gr

*Joint funding between KRIPIS-THESPIA and ARCHIMED programmes

ABSTRACT

The realization of Renewable Energy Sources (RES) for power generation as the only environmentally-friendly solution, moved solar systems to the forefront of the energy market in the last decade. The capacity of solar power doubles almost every two years in many European countries, including Greece. This rise has brought the need for reliable predictions of meteorological data that can easily be utilized for proper RES-site allocation. The absence of solar measurements has, therefore, raised the demand for deploying a suitable model in order to create solar maps. The generation of a solar map for Greece could provide solid foundations on the prediction of the energy production of a solar power plant installed in the country, by providing an estimation of the solar energy acquired at each longitude and latitude of the map. In the present work, the Meteorological Radiation Model (MRM), a broadband solar radiation model, is engaged. This model utilizes common meteorological data, such as air temperature, relative humidity, barometric pressure and sunshine duration, in order to calculate solar radiation for areas where such data are not available. Hourly values of the above meteorological parameters are used from 39 meteorological stations, evenly dispersed around Greece; hourly values of solar radiation are, therefore, calculated through MRM. Then, by using an integrated spatial interpolation method, a Greek solar energy map is generated, providing annual solar energy values all over Greece.

Keywords: MRM, Meteorological Radiation Model, solar radiation, Greek solar map

INTRODUCTION

Solar power systems have been at the forefront of the global energy market for at least one decade. In the meantime, the world realized that the only environmentally-friendly solution concerning power generation is the implementation of RES. In this context, following the rapid development of wind energy, solar power systems also presented remarkable market progress. At the same time, a rapid increase in installations of photovoltaic systems has been recorded in many European countries, including Greece, where during the recent period the installed photovoltaic capacity almost doubles every two years with total installations in 2013 exceeding 2.5 GW_e. It is, therefore, obvious that there is an increased interest in the possession of up-to-date and accurate solar radiation data that play prime role in energy-resource assessment of solar power systems.

In the recent years, solar radiation modelling utilizing existing climatic parameters, such as sunshine duration, cloud cover, relative humidity, air temperature etc., has shown remarkable progress. It is generally accepted that the use of models for solar radiation prediction, instead of using scattered ground-based measurements, is essential in solar energy systems design, because in most cases the low density and the limited number of solar

radiation measuring stations cannot describe the required variability of the climatic parameters involved (Muneer et al. 2007).

Several solar radiation models have appeared globally since the middle of the 20th century in order to generate solar radiation on horizontal plane, mostly under clear-sky conditions (e.g. Gueymard 2012). For example, the US National Solar Radiation Data Base provides hourly radiation data and Typical Meteorological Years (TMYs) for 239 US regions, with more than 90% of these having been derived from appropriate modelling (Maxwell 1998). Also, the European Solar Radiation Atlas (ESRA) is used for providing topography-based maps of solar irradiance in Europe and bordering countries (Page et al. 2001).

In the context of the above, a broadband model, which has been developed in Greece in the late 80's by the Atmospheric Research Team at the National Observatory of Athens for estimating solar radiation on horizontal surface, is the *Meteorological Radiation Model* (MRM). Since then, consecutive versions (the latest is version 5) of the model have been released with their full description given in a series of publications (Kambezidis et al. 1999, Psiloglou and Kambezidis 2007). Applications of MRM may be found in a variety of solar resource-assessment studies as well as in solar irradiance forecasting (Museruka and Mutabazi 2007, González et al. 2010). The main advantage of MRM is its simplicity in acquiring and using the necessary input data (i.e. four measured variables namely, air temperature, relative humidity, barometric pressure and sunshine duration).

Apart from the establishment of solar models, solar irradiance maps created by spatial interpolation of the estimated solar radiation by such models can provide a first insight of the solar potential at a candidate location. Several spatial interpolation methods can be found in the literature, such as natural neighbour interpolation (Dinis et al. 2009), inverse functions of distance (Pons and Ninyerola 2008), multiple linear regression (Daly et al. 1994), splines (McKenney et al. 2008) or kriging (Ruiz-Arias et al. 2011). The results of different studies, which compare deterministic and stochastic methods for the interpolation of environmental variables, show that the kriging method presents considerable advantages over the deterministic interpolation procedures (Luo et al. 2008). Such methods are based on the analysis of statistical properties, such as the data distribution and spatial correlation between the measured points among sites, providing reliable estimates for homogeneous terrains with similar climatic characteristics.

In the framework of the above, the present study utilizes geostatistics combined with model-estimated solar radiation data at several meteorological stations across the Greek territory by providing large-scale global solar radiation/energy. More precisely, the present work relies on collected synoptic data values from 39 meteorological stations belonging to the Hellenic National Meteorological Service (HNMS) during a 15-year period. The meteorological data include 3-hourly values of air temperature, relative humidity, barometric pressure and daily values of sunshine duration. By using linear interpolation on the 3-hourly values, an hourly database is generated. The corresponding database is amended with hourly values of global solar radiation on horizontal plane calculated by MRM. Finally, a solar map is developed by using spatial interpolated kriged data derived from solar radiation values at the 39 different locations across the country. A solar energy map so created aims to serve basic solar resource information and provide a general view of the distribution of solar radiation over the country.

METHODOLOGY

Fifteen (15) years of synoptic meteorological data were used, covering the period between 1985 and 1999. The measurements were obtained from 39 meteorological stations of the HNMS network evenly dispersed around Greece (see Figure 1).

Figure 1: Location of the 39 meteorological stations used in the study

The obtained meteorological data include 3-hourly values of air temperature, relative humidity and barometric pressure along with daily values of sunshine duration. It should be noted that the data underwent a further quality control through cleaning and gap-filling, in order to remove unwanted or false values and fill-in potentially corrupted or erroneous data points. More specifically, in order to detect and exclude erroneous data, a quality-control routine was applied, based on the physical range of the parameters and the maximum time-step variation (Psiloglou and Kambezidis 2007). By using linear interpolation on the 3-hourly values, an hourly database was generated.

The MRM model (version 5) was engaged, in order to generate solar radiation values for the 39 meteorological stations. According to the model, the direct-beam component of solar radiation normal to a horizontal plane at the earth's surface, under clear sky and natural atmosphere, is the extra-terrestrial radiation at the top of the atmosphere modified by absorption and scattering from its various constituents. Thus, during cloudless periods, the direct-beam radiation, I_b, received on a horizontal surface can be expressed as:

$$I_b = I_{ex} \cdot \cos\theta_z \cdot T_w \cdot T_r \cdot T_o \cdot T_{mg} \cdot T_a \quad (1)$$

where θ_z is the solar zenith angle, I_{ex} is the normal incidence extra-terrestrial solar radiation on the n_i-th day of the year; the T terms are the broadband transmittance functions for the absorption of water vapor (T_w), uniformly-mixed gases $(CO_2, CO, N_2O, CH_4 \text{ and } O_2)$ (T_{mg}), ozone (T_o), and total extinction (scattering and absorption by molecules and aerosols in the atmosphere)$(T_r, T_a, \text{respectively})$.

The diffuse sky radiation under clear-sky conditions is assumed to be made up of a portion of singly scattered by the atmospheric constituents (molecules and aerosol particles) direct beam radiation, I_{ds}, plus a multiple scattering component, I_{dm} (Psiloglou et al. 2000):

$$I_{ds} = I_{ex} \cdot \cos\theta_z \cdot T_w \cdot T_{mg} \cdot T_o \cdot T_{aa} \cdot 0.5 \cdot (1 - T_{as} \cdot T_r) \quad (2)$$

where T_{aa} is the aerosol transmittance function due to absorption only and T_{as} the aerosol transmittance due to scattering alone.

The total solar radiation received under clear-sky conditions on horizontal plane at the earth surface is the sum of the direct-beam and diffuse components, i.e.:

$$I_g = I_b + I_d \quad (3)$$

The corresponding direct-beam solar radiation under cloudy skies, I_{cb}, can be obtained by:

$$I_{cb} = I_b \cdot T_c \quad (4)$$

where T_c is the cloud transmittance.

Accordingly, the diffuse radiation at ground level under cloudy skies, I_{cd}, is the sum of the I_{cds} and I_{cdm} components. The singly-scattered portion of the diffuse radiation in the presence of clouds, I_{cds}, is computed by Barbaro et al. (1979):

$$I_{cds} = I_{ds} \cdot T_c + k^* \cdot (1 - T_c) \cdot (I_b + I_{ds}) \quad (5)$$

where k^* is an empirical transmission coefficient, whose value is a function of latitude and is obtained from Berland and Danilchenko (1961). The ground-reflected, atmospheric and cloud backscattered diffuse term, I_{cdm}, is modelled as in clear-sky conditions:

$$I_{cdm} = \frac{(I_{cb} + I_{cds})(a_g \cdot a_{cs})}{1 - a_g \cdot a_{cs}} \quad (6)$$

where a_g is the surface albedo and a_{cs} is the albedo of the cloudy sky.

Finally, the total solar radiation received under cloudy-sky conditions (partly or overcast) on horizontal surface is the sum of the horizontal direct-beam and diffuse components, i.e.:

$$I_{ct} = I_{cb} + I_{cd} \quad (7)$$

The obtained 15-year hourly solar database was used to develop a TMY for each of the 39 locations. A TMY is a dataset of hourly values of solar radiation and meteorological parameters composed of selected months from individual years, concatenated to form a complete year. A TMY represents the climatic conditions, typical over a long period at a location. For the generation of the 39 TMYs, the Sandia method was used (Hall et al. 1978) as modified by Pissimanis et al. (1988) and Argiriou et al. (1999). The Sandia method is an established empirical methodology for selecting individual months from different years over an available period, based on the Filkestein-Schafer (FS) statistics of 14 daily indices, namely maximum, minimum, mean and range of air temperature, relative humidity and barometric pressure and daily direct-beam and global solar energy. The weighted sum of FS statistics is calculated by using weighting factors for each daily index (Table 1).

Table 1: Weighting factors used for the FS statistics

Parameter	**Daily index**	**Weighting factor**
Air temperature	*Maximum*	3
	Minimum	3
	Mean	9
	Range	3
Relative humidity	*Maximum*	3
	Minimum	3
	Mean	9
	Range	3
Barometric pressure	*Maximum*	5
	Minimum	3
	Mean	3
	Range	3
Global radiation	*Daily sum*	25
Direct radiation	*Daily sum*	25
Sum		**100**

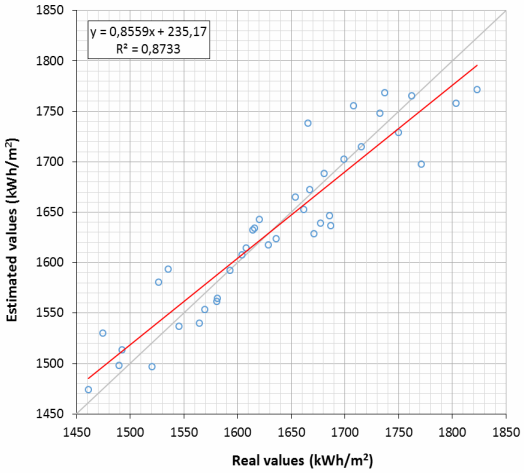

Figure 2: Comparison of estimated and real annual energy values for the 39 locations under investigation in Greece

and real values is very good as the coefficient of determination (R^2) exceeds 87%.

Based on the above methodology, an updated solar energy map was developed along with the corresponding predicted errors (Figure 3).

Figure 3 presents the global solar energy variation throughout the Greek region divided in 9 solar zones. The locations of the meteorological stations are coloured, based on their real annual solar energy value. According to the results, the annual solar energy in Greece ranges between 1450 and 1820 kWh/m^2, with southern areas possessing higher values of solar energy. The mean error of the estimated vs the real values is 1.94 kWh/m^2, which is relatively low.

The hourly solar radiation data of the 39 TMYs were used, in order to calculate the annual global solar energy obtained on horizontal plane. After testing several spatial interpolation methods, the Empirical Bayesian Kriging (EBK) was proved the most accurate for creating the Greek solar map. Fig. 2 presents a scatter plot of the estimated annual solar energy by EBK at the location of the 39 meteorological stations versus the real values as they were calculated by the TMYs. As indicated in the graph, the correlation between estimated

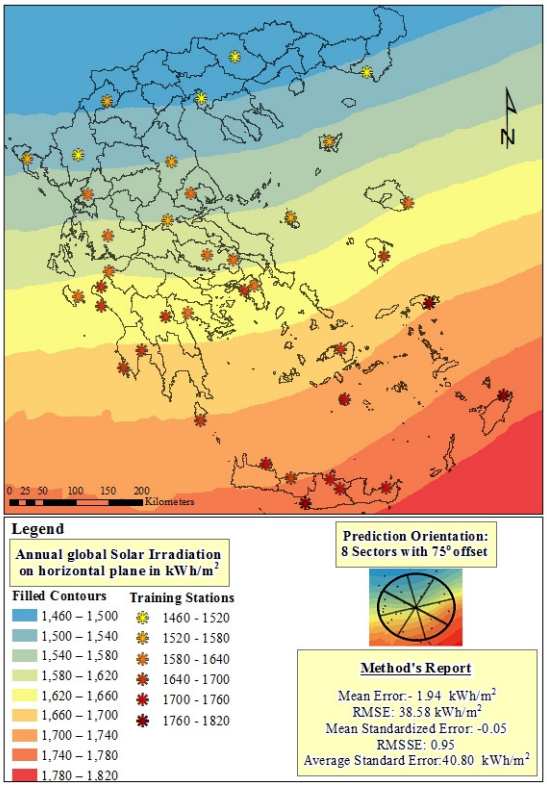

Fig. 3: Solar map of Greece based on the EBK method

CONCLUSIONS

The possession of up-to-date and accurate solar radiation data plays a key role in energy-resource assessment of solar power systems. Given the low density and limited number of solar radiation measuring stations, the use of solar radiation models is imperative. The present work presented an integrated procedure, which was used in order to develop an updated Greek solar map based on the solar radiation data estimated by the Meteorological Radiation Model at 39 meteorological stations belonging to the Hellenic National Meteorological Service network. The solar energy map so created provides solar resource information for any location over the country.

REFERENCES

Argiriou, A., Lykoudis, S., Kontoyiannidis, S., Balaras, C.A., Asimakopoulos, D.N., Petrakis, M. and Kassomenos, P., 1999, "Comparison of methodologies for TMY generation using 20 years data for Athens, Greece.", Solar Energy, Vol.66(1), pp.33–45.

Barbaro, S. B., Coppolino, S., Leone, C., and Sinagra, E., 1979, "An atmospheric model for computing direct and diffuse solar radiation", Sol. Energy, Vol.22, pp.225–228.

Berland, T. G. and Danilchenko, V. Y., 1961, "The continental distribution of solar radiation", Gidrometeoizdat, Leningrad.

Daly, C., Neilson, R.P. and Phillips, D.L., 1994, "A statistical-topographic model for mapping climatological precipitation over mountainous terrain", Applied Meteorology, Vol.33, pp.140–158.

Dinis, L.M., Jorge, R.M. and Belinha, J., 2009, "The natural neighbour radial point interpolation method: dynamic applications." Engineering Computations, Vol. 26, pp.911–949.

González, J., Serrano E. and Wiesenberg, R., 2010, "DNI forecasting using coupled WRF and MRM, enhanced with a neural network for CSP applications", Proc. Int. Conf. SolarPACES, Perpignan, France.

Gueymard, C.A., 2012, "Clear-sky irradiance predictions for solar resource mapping and large-scale applications: Improved validation methodology and detailed performance analysis of 18 broadband radiative models.", Solar Energy, Vol.86, pp.2145-2169.

Hall, I.J., Prairie, R.R., Anderson, H.E. and Boes, E.C., 1978, "Generation of a typical meteorological year", Annual Meeting of the American Section of the ISES.

Kambezidis, H.D., Adamopoulos, A.D. and Sakellariou, N.K., 1999, "The Meteorological Radiation Model", Int. Conf. ISES Solar World Congress, Jerusalem, Israel.

Luo, W., Taylor, M.C. and Parker, S.R., 2008, "A comparison of spatial interpolation methods to estimate continuous wind speed surfaces using irregularly distributed data from England and Wales", Climatology, Vol.28, pp.947–959.

Maxwell, E.L., 1998, "METSTAT – The solar radiation model used in the production of the National Solar Radiation Data Base (NSRDB)", Solar Energy, Vol.62, pp.263–279.

McKenney, D.W., Pelland, S., Poissant, Y., Morris, R., Hutchinson, M., Papadopol, P., Lawrence, K. and Campbell, K., 2008, "Spatial insolation models for photovoltaic energy in Canada", Solar Energy, Vol.82, pp.1049–1061.

Muneer, T, Younes, S. and Munawwar, S., 2007, "Discourses on solar radiation modelling", Renewable and Sustainable Energy Reviews, Vol.11, pp.551–602.

Museruka, C. and Mutabazi, A., 2007, "Assessment of global radiation over Rwanda." Proc. Int. Conf. on clean electrical power. Capri.

Page, J., Albuisson, M., and Wald L., 2001, "European solar radiation atlas: a valuable digital tool", Solar Energy, Vol.71, pp.81–83.

Pissimanis, D., Karras, G., Notaridou, V. and Gavra, K., 1988, "The generation of a 'typical meteorological year' for the city of Athens", Solar Energy, Vol.40(5), pp.405–411.

Pons, X. and Ninyerola, M., 2008, "Mapping a topographic global solar radiation model implemented in a GIS and refined with ground data", Climatology, Vol. 28, pp.1821–1834.

Psiloglou, B. E., Santamouris, M., and Asimakopoulos, D. N., 2000, "Atmospheric broadband model for computation of solar radiation at the Earth's surface. Application to Mediterranean climate", Pure Appl. Geophys., Vol.157, pp.829–860.

Psiloglou, B.E. and Kambezidis, H.D., 2007, "Performance of the meteorological radiation model during the solar eclipse of 29 March 2006", Atmospheric Chemistry and Physics, Vol.7, pp.6047–6059.

Ruiz-Arias, J.A., Pozo-Vazquez, D., Santos-Alamillos, F.J., Lara-Fanego, V. and Tovar-Pescador, J., 2011, "A topographic geostatistical approach for mapping monthly mean values of daily global solar radiation: A case study in southern Spain", Agricultural and Forest Meteorology, Vol.151, pp.1812-1822.

Cosmic Ray Intensity and Solar Activity Variations Possible Effects on the Rainfall in Turkey and Azerbaijan and Caspian Sea Level Changes

Famil Mustafa[1], *Ali Kilcik*[2], *Elchin Babayev*[1], *Atila Ozguc*[3]

[1] Shamakhy Astrophysical Observatory named after Nasiraddin Tusi, ANAS
[2] Department of Physics, Faculty of Science, Akdeniz University, Antalya, Turkey
[3] Kandilli Observatory and E.R.I., Bogazici University, Cengelkoy, Istanbul, Turkey
E-mail: famil_m@yahoo.com

ABSTRACT

The possible effects of cosmic ray intensity and solar activity variations on the rainfall over Turkey and Azerbaijan (middle-latitude Turkey - Caucasus/Caspian Sea region) and Caspian Sea level changes are investigated. Rainfall data for Turkey and Azerbaijan as climate parameter and sunspot number and cosmic ray intensity data as space weather indicators are used. Considered rainfall period was from January 1975 to the end of December 2008 meanwhile Caspian Sea level data were from 1900 to 2000. Multi-Taper Frequency Spectrum method (MTM) is applied to obtain the cyclic behavior of considered parameters. The most pronounced power peaks found by MTM were 1.2, 2.1-2.2 and 3.6-3.9 years (significance level > 99.9 %) which were reported earlier for some solar and cosmic ray activity indicators. Correlation analysis was also used in this study. Results did not reveal a remarkable correlation between rainfall and solar activity. It is concluded that in comparison to solar activity, cosmic rays have more significant effect on rainfall and sea level changes in studied regions and considered period. Cosmic ray intensity variations and solar wind changes caused effects could be considered as one of possible bridges in study of solar-climate relationships.

INTRODUCTION

Among the most debated questions in climate change are that of Sun-climate and cosmic ray-climate variability, which have attracted the attention of scientists for years (Kirkby, 2007; Dorman, 2009). Over the last years diverse reconstructions of past climate change have revealed some associations with cosmic ray variations recorded in cosmogenic isotope archives, providing persuasive evidence for solar or cosmic ray forcing of the climate. Sun-climate variability question is likely to remain open until a physical mechanism is established meanwhile observations suggest that cloud cover may be influenced by cosmic rays, which are modulated by the solar wind and, on longer time scales, by the geomagnetic field, so on.

Our recent study (Kilcik et al., 2008) shows that investigation of Sun–climate relationship on local scale may give better possibilities for understanding of the problem than global scale. The study of possible effects of cosmic ray intensity and solar activity variations on the rainfall over local regions could give interesting results.

The Caspian Sea is of exceptional interest to scientists because of its history of fluctuations in both area and depth, which offer clues to the complex geological and climatic evolution of the region. The Caspian Sea not only is an economical source but also a climatic regulator of the area. During many years there have been considerable fluctuations of the sea level.

One of the more fascinating aspects of the study of the Caspian Sea, however, is the study of long-term fluctuations over the decades and centuries gathered from archaeological, geographical, heliogeophysical and historical evidence. Long-term and seasonal fluctuations of the Caspian Sea level are considered to be mainly the result of fluctuations of components of its water balance. But possible role of space weather/climate influence through different mechanisms should not be neglected (i.e., Solov'eva in 2004 considered dependence of Caspian Sea level oscillations on the solar activity).

AIMS of STUDY

In this paper we made attempts to study possible effects of cosmic ray (CR) intensity and solar activity (SA) variations effects on the rainfall over two middle latitude located neighbor countries (Turkey and Azerbaijan) and Caspian Sea level changes. Long-period climate (precipitation and sea levels) data as well as relevant space weather parameters were used and modern mathematical methods were applied.

DATA AND METHODS

Rainfall data over Turkey and Azerbaijan are taken from Turkish State Meteorological Service, National Hydrometeorological Department of the Ministry of Ecology and Natural Resources of the Republic of Azerbaijan and NOAA's Satellite and Information Service (NESDIS), NNDC CDO. Monthly mean of rainfall cover 72 stations in Turkey. Azerbaijani rainfall data come from three main regions spread on latitude and longitude of this comparatively small country (Ganja, Lenkeran and Zagatala). Rainfall and cosmic ray data used in this study refer to the period 1975-2008. This study uses also Caspian Sea level changes data (1900-2000) taken from 5 stations around this largest inland sea. Sea level data were provided by the Institute of Geography, Azerbaijan National Academy of Sciences. The cosmic ray (CR) data is taken from the NOAA's National Geophysical Data Center (NGDC).

To remove monthly and seasonal changes, all griddled monthly data were smoothed with 12 month running average and anomalies of these smoothed data were calculated.

Following correlation and spectral analyses methods were applied in our study:

1. **Partial correlation analyses** (Pearson correlation method). We used yearly data from 1975 to 2008 for the "CR – Rainfall" correlations. This time period covers three solar cycles (21, 22 and 23). For the "CR – Caspian Sea level" correlations analysis we used only two cyclic data (1975 – 1997) due to lack of part of data for 23rd cycle. All cyclic correlations calculated for each cycle and data sets separately. The partial correlation analysis results are given in the Table 1.
2. **Spectral analysis** (period analysis). There has been used the Multi-Taper method (MTM) of spectral analysis, developed by Thomson (1982), to analyze periodical changes. This method reduces the variance of spectral estimates by using a set of tapers. In our study we used three sinusoidal tapers. For the period analyses monthly data sets were used. Our significance test is carried out with respect to red noise, since the rainfall and sea level records, have larger power at lower frequencies. All harmonic signals have been obtained by using of 90% confidence level.

RESULTS

In this study we have applied correlation and MTM spectral analysis methods to find (a) correlations between Turkey and Azerbaijan rainfall, Caspian Sea level changes and cosmic ray intensity variations; and (b) to build power spectrum which provides continuous temporal evolution of the entire range of periods.

Table 1. The partial correlation analyses results

	Cycle 21	Cycle 22	Cycle 23
CR - Azerbaijan rainfall	-0.47	-0.58	-0.46
CR -Turkey rainfall	-0.04	0.54	
CR – Caspian Sea Level	-0.50	0.17	

The correlation analyses results are given in Table 1. These are:

- Azerbaijani rainfall data show comparatively significant negative correlations with cosmic ray intensity data for all considered solar cycles;
- Turkey rainfall data show positive correlations only for solar cycle 22.
- Caspian Sea level data (when considering the period of 1975-2000) show comparatively significant negative correlation for solar cycle 21.

- Turkey and Azerbaijan rainfall data sets show different behaviors in respect to solar activity variations.

Correlation analysis of surface air temperature over Azerbaijan for cycles 21, 22 and 23 showed anti-correlation (-0.2, -0.08 and -0.42). It should be noted that correlation between Azerbaijani temperature and Caspian Sea level changes was 0.42 meanwhile "rainfall – sea level" correlation coefficient was – 0.73.

Power spectrum analysis reveals that:

- CR data show well-known periodicities such as 1.7, 2.2, 2.9, 1.1, 1.5, 10.7 years, etc., which are also revealed in solar activity variations;
- 1.2 years periodicity exists in all data sets used in this study (well seen in Azerbaijani rainfall and Caspian Sea level changes data with high CI);
- 3.7 years periodicity found in CR data also was revealed as in quasi forms in Turkey rainfall data (3.6 years) and Caspian Sea level changes data (3.9 years) meanwhile 2.2 years periodicity found in CR data also exists in both Azerbaijani (2.1 years) and Turkey rainfall data;
- 2.9 years periodicity found in CR data was revealed in all climate data.

DISCUSSIONS

Fig.1. shows that there is high level anti-correlation between CR and SSN. This well-known fact reveled also in our analyses, enables to consider CR intensity variations as one of possible bridges in Sun-climate relationship. Detailed analysis of Fig.1 shows that Azerbaijani and Turkey rainfall trends are not similar (not-coinciding) and there are even some periods (i.e., 1981-1983), when they show opposite trends. The time interval 1981-1983 corresponds to El Chichon volcanic activity (1981) period, and this interesting fact doubts that volcanic activity can have negative / positive effects on rainfall anomalies. In 1991 – 1995 there was another strong volcanic activity (Pinatubo) and both rainfall curves show a decreasing trend. The effects of these two big volcanic activities on incoming solar radiation are shown in Fig. 3.

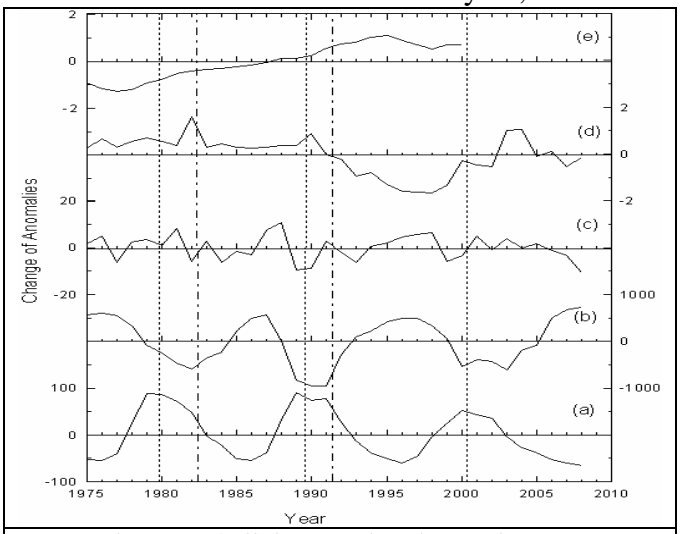

Fig.1. Changes of all data used in this study:
a) Sunspot number,
b) Cosmic ray intensity,
c) Rainfall over Turkey,
d) Rainfall over Azerbaijan,
e) Caspian

The other interesting period is 1991-2002; there is a strong deep in the Azerbaijani rainfall data for this period (our correlation analysis also indicates this fact). Comparison of climate and CR data and correlation analyses show different results which depend on climate data. These differences may arise from other factors, such as different absorbing aerosol concentrations in the atmosphere, pressure / altitude differences of the data stations, isolation of the regions etc.

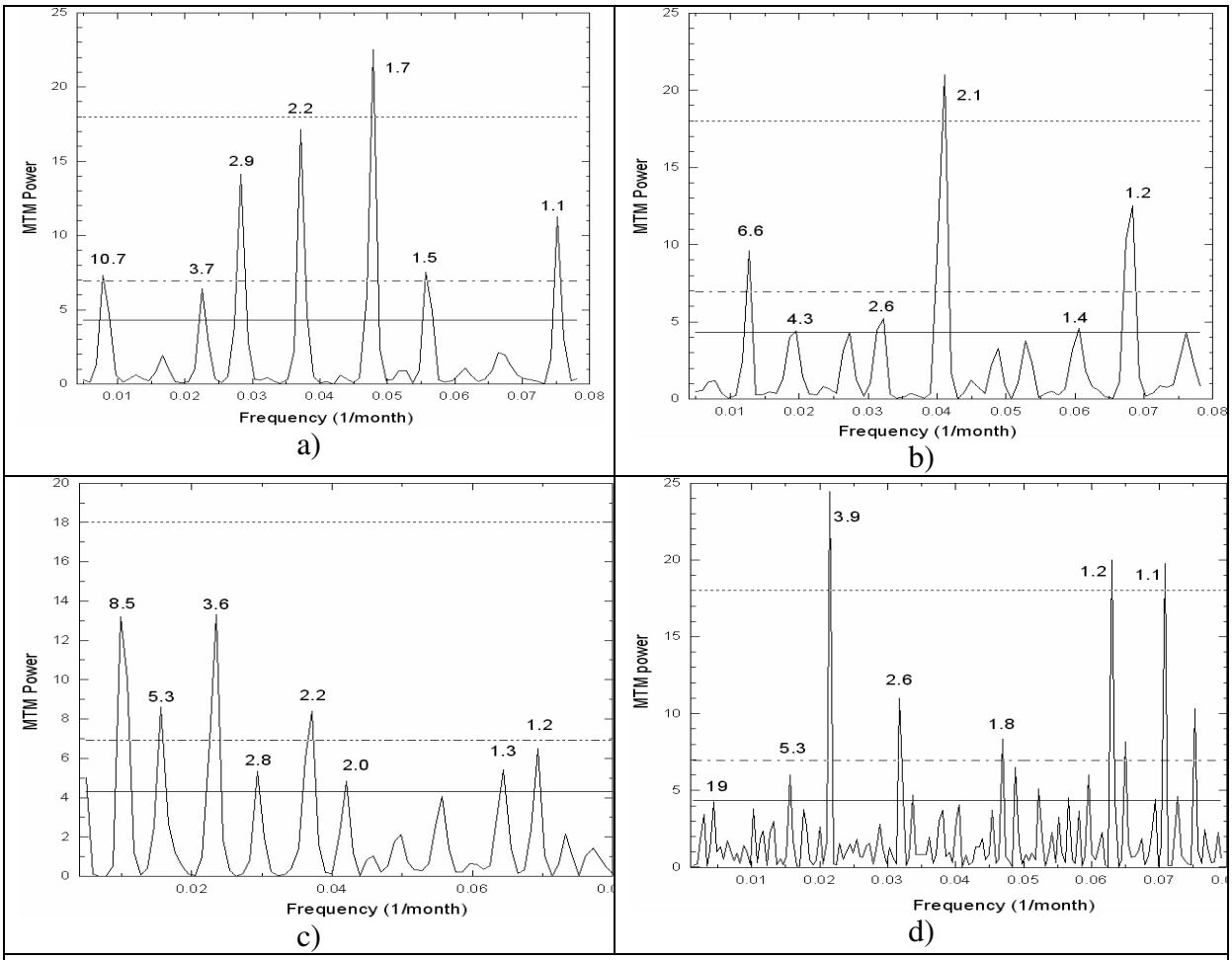

Fig.2. Power spectrums calculated for all considered data sets: a) CR, b) Rainfall of Turkey c) Rainfall of Azerbaijan, d) Caspian Sea level changes.

Kilcik (2005), Kilcik et al (2008) reported that the Sun – climate relation should be investigated on local scale due to these dependencies of Sun - climate system. As we already mentioned, periodicities found in our spectral analysis (see Fig. 2.) with high CI level, are displayed in many solar, geophysical phenomena, in IMF medium so on. Below we provide most interesting facts related to our study. The primary cause of the solar modulation of cosmic rays is not the level of sunspot activity, but the varying strength of the solar wind. 1.1, 1.3, 3.3, 5.5 year periods were found in the spectrum of solar wind velocity (1964-2003) (Nayar, 2006). The 1.3 year period is related to the variation in the rotation rate at the bottom of the solar convection zone (Howe et al., 2000). 1.1- and 2.4-year periods alongside with others were found in the power spectrum of sunspot numbers data during 1964 to 2003 meanwhile 5.5 year was seen in power spectrum of geomagnetic activity index Ap (Nayar, 2006). 3.9 year (very high CI) periodicity is quite close to the period 3.7-4 years, found either in geomagnetic activity or solar wind variations. A strong 1.3 year variation in solar wind speed occurs concurrently at different heliocentric distances around the ecliptic. The power in 1.3 year periods is found to follow the total number of sunspots and both vary approximately in phase. Krivova and Solanki (2002) found significant power at all multiplets of 1.3 year up to 10.4 year, which is nearly equal to the period of the solar cycle.

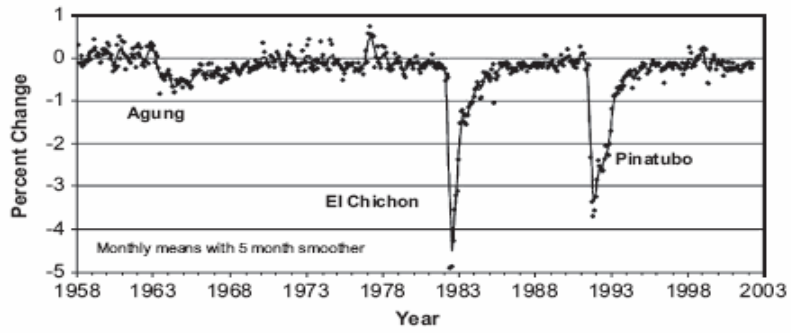

Fig.3. Net solar radiation measured at Mauna Loa Observatory, relative to 1958, showing the effects of major volcanic eruptions. Annual variations are due to the transport of Asian dust and air pollution to Hawaii. Figure is taken from Earth System Research Laboratory's web page (http:// www.esrl.noaa.gov/gmd/about/climate.html).

It should be noted that quasi-biennial oscillations (from ~1.5 to ~3.0 years) in various active events in the Sun are the second most powerful variation after the 11-year cycle (Ivanov et al, 2000).

CONCLUSIONS

Based on results of our preliminary study we conclude that:

- CR intensity variations can be considered as one of possible bridges in study of solar-climate relationships;
- There is an evidence that changes in CR intensity have effects on rainfall levels over Turkey and Azerbaijan as well as Caspian Sea level (latter could be due to rainfall effects on Volga river's flow level into the sea). Although this remains unclear yet, we also suggest that cloud cover may be influenced by cosmic rays, which are modulated by the solar wind and, on longer time scales, by the geomagnetic field and by the galactic environment of the Earth;
- Revealed in climate and sea level changes data periodicities (within 2-4 years interval) are well pronounced in solar wind and cosmic ray activity variations;
- We conclude that solar wind effects through different physical mechanisms (i.e., caused by high speed streams from coronal holes or fast CMEs-driven disturbances resulting in geomagnetic activity, Forbush decreases so on) could be considered one of major players in interpretation of results in space weather - climate relations' studies;
- Solar cycle 22 must be studied separately which generated a low number of flares in respect to its predecessor; correlation analyses show different (from other considered cycles 21 and 23, showing coinciding results) results namely for cycle 22;
- 1.2 year periodicity which is quite close to 1.3 year well-established periodicity seems to be one of important periods in solar-cosmic-ray-climate relationship;
- There was preliminarily found some correlation between sea level and total solar irradiance as well as were revealed (Fourier analysis) some signatures of Bruckner (~35 years) climatic cycle, but these questions must be studied in details and carefully;
- Mechanisms for the amplification of solar and cosmic ray forcing are not well established: despite the increasing evidence of its importance, "Sun - climate variability" link is likely to remain as open question; It is possible that solar activity variations during pre-industrial times were one of major causes of climate change. The Caspian Sea level changes (especially rising trend since 1978) may arise from the increase of greenhouse gases (GHG) concentration and/or oil pollution; Precipitation changes in the Volga River drainage basin also must be considered in analysis taking into account their possible forcing by solar activity and rainfall;
- Effect of volcanic activity on rainfall must be studied together with space weather influence;

- We should not focus only one single physical mechanism, i.e., space weather effects. There might be several possible physical mechanisms related to space weather changes that can operate together in determining the state and dynamics of climate on Earth. I.e., variations in ultraviolet and solar-induced changes in ozone (O3) may have a small effect on radiative forcing but additionally may affect climate through changing the distribution of solar heating and thus indirectly through a dynamical response;
- Further studies must be continued either on global or local scales taking into account all possible mechanisms (geographical, geological, ecological, heliogeophysical so on).

ACKNOWLEDGEMENTS

The CR data used in this study are taken from NGDC web page. We acknowledge the National Hydrometeorological Department of the Ministry of Ecology and Natural Resources of the Republic of Azerbaijan and NOAA Satellite and Information Service, NESDIS, NNDC CDO for rainfall data as well as Prof. Ramiz Mammadov (Azerbaijan) for the Caspian Sea level changes data.

REFERENCES

[1] Dorman L.I. The Role of Space Weather and Cosmic Ray Effects in Climate Change (Chapter 3). In: Climate Change: Observed Impacts on Planet Earth, ISBN: 978-0-444- 3301-2, Trevor M. Letcher (ed.), Elsevier, 2009, pp.43-76.

[2] Howe R., J. Christensen-Dalsgaard, F. Hill, R. W. Komm, R. M. Larsen, J. Schou, M. J. Thompson and J. Toomre, "Dynamic variations at the base of the solar convection zone", Science, **287**, 456-460, 2000.

[3] Ivanov E.V., V.N. Obridko, and B.D. Shelting, Quasi-Biennial Oscillations of the Solar Magnetic Fields, Proc. 10th European Solar Physics Meeting", Solar Variability: From Core to Outer Frontiers", ESA **SP-506**, 847-850, 2000.

[4] Kilcik, A. Regional Sun–climate interaction. JASTP,**67**, 1573–1579. 2005

[5] Kilcik, A., Ozguc, A., Rozelot, J.P., and Yesilyurt, S., Possible traces of solar activity effect on the surface air temperature of Turkey, JASTP **70**, 1669–1677, 2008.

[6] Kirkby Jasper. Cosmic rays and climate. Surveys in Geophysics, **28**, 333-375, 2007

[7] Kirova N. A. and S. K. Solanki, "The 1.3-year and 156-day periodicities in sunspot data: Wavelet analysis suggests a common origin", A & A**, 394**, 701-706, 2002.

[8] Nayar Prabhakaran S.R. Periodicities in solar activity and their signature in the terrestrial environment. In: Proceedings of the ILWS Workshop, Goa, India: February 19-24, 2006, Edited by N. Gopalswamy and A. Bhattacharyya, "Solar Influence on the Heliosphere and Earth's Environment: Recent Progress and Prospects", 2006,170-177.

[9] Solov'eva N.N. Study of dependence of Caspian Sea level oscillations on the solar activity, S.-Petersburg, RGGMU Press, 2004, 70 pages (in Russian).

[10] Thomson, D.J., 1982. Spectrum estimation and harmonic analysis. IEEE Proceedings **70**, 1055–1096.

Estimation of Solar Activity Influence on Vertical Extent of Sprites

Peter Tonev

Space Research & Technology Institute, Bulgarian Academy of Sciences
E-mail: ptonev@bas.bg

Abstract.

Sprites in their lower portion (below 60 - 65 km) consist of downward propagating positive streamers which cause chemical disturbances (mainly of NO_x and O_3 constituents) in the lower mesosphere and upper stratosphere. A single sprite occupies thousands of cubic kilometers in the middle atmosphere. The total rate of sprites over the globe is estimated to be 1-3 per minute. The influence of 11-year solar activity (SA) variations on sprites' vertical extension, and thus, on their effects on chemical balance below 60 km is studied. For this goal, the altitude of termination of the sprite positive streamers is estimated as function of solar activity level by otherwise equal conditions. 11-year variations of this altitude can take place due to sensitivity of conductivity, and thus, of the sprite-driving electric fields, to SA. The streamer driving quasi-static electric fields below 60 km are evaluated by modeling during solar minimum and maximum, respectively by modeling based on the continuity equation for the Maxwell's current. The computations show that during solar minimum sprites due to +CG lightning of large charge moment change reach a lower altitude than during solar maximum; for weaker sprites the difference can be reversed, but smaller. The difference in lower sprite boundary determined by SA changes varies from several hundred meters to almost 1 km depending on the flash parameters and on conductivity in clouds.

Introduction

Red sprites are transient luminous events which occur in the height interval from 90 down to 40 km above nighttime thunderstorms. They are driven by quasi-static (QS) electric fields generated in this region typically after a positive cloud-ground (+CG) lightning discharge. Below ~65 km (in its mature portion) a sprite is essentially a net of positive streamers which propagate downwards with velocity in the range ~2×10^6 - ~2×10^7 m/s and are multiplied by branching. Sprites are widely studied as a factor of disturbances in chemical balance in strato-mesosphere (Arnone et al., 2008; Hiraki et al., 2008). The problems is considered about ability of sprites to be a link between solar activity (SA) and the chemical state of strato-mesosphere (at least, in specific regions on the Earth). Our arguments are: 1) In the sprite region from ~ 90 down to ~ 40 km, the factors for ionization and formation of conductivity are sensitive to the solar activity, hence, the post-lighting electric fields and sprite parameters can be also affected by SA; 2) A sprite consists of thousands of streamers which cause (especially below 60 km) chemical perturbations concerning NO_x and O_3 for hours and another small constituents (Hiraki et al., 2008; Arnone et al., 2008); 3) The global frequency of visible sprites estimated from satellite data is 1 - 3 per minute, and large part of sprites remain unobservable. In specific regions at middle geomagnetic latitudes where the GCR flux is the main ionization factor and the sprite activity is large (Great Plains in USA, South Africa, South America, etc.) sprites possibly disturb atmospheric chemistry balance permanently, and the 11-year variations of their chemical effects may be of importance.

If the vertical extent of sprites is controlled by the SA level, then significant 11-year changes in strato-mesospheric chemistry in these specific regions can take place during a solar cycle. Once created, the downward positive streamers of a sprite reach a termination height z_T which depends on the applied post-lightning QS electric field E so that:

$$E(z_T) = E_{cr+}(z_T), \qquad (1)$$

Here $E_{cr+}(z) = 4.4\times10^5 N(z)/N_0$ V/m is the threshold electric field of propagation of a positive streamer; N(z) is the density of neutral atmosphere at altitude z, $N_0 = N(z=0)$. Since the electric field $E(z)$ decreases with lowering of the altitude z of a streamer faster than E_{cr+}, Expr. (1) ensures support of streamer propagation at any height $z > z_T$ since $E(z) > E_{cr+}(z)$. We hypothesize that the streamer termination height z_T depends on SA changes since the streamer driving electric field E depends on conductivity σ, which is a function of SA as noted above.

The electric fields driving sprites

The distribution of the QS fields **E** generated by a +CG lightning discharge which produces a sprite depends on the flash parameters and on the night-time conductivity profile $\sigma(z)$. The distribution of the QS electric field **E** after a +CG lightning discharge is obtained by a 2D model (Tonev and Velinov, 2007) in cylindrical coordinates (r,φ,z) where z is the altitude and r is the radial distance from the charge removed by the flash. The continuity equation for the Maxwell's current is solved, $\nabla\cdot\mathbf{j}_M = 0$, where $\mathbf{j}_M = \mathbf{j}_C + \mathbf{j}_D$; $\mathbf{j}_C = \sigma\mathbf{E}$ and $\mathbf{j}_D = \varepsilon_0\partial\mathbf{E}/\partial t$ are the conduction and the displacement currents. The results obtained by Tonev and Velinov (2007) (their Fig.2) are for $E(z,t) = \mathbf{E}$ $(r=0, z, t)$ at sprite altitudes $40 \le z \le 90$ km. The conductivity is assumed to be not influenced by the electric field **E**. This is valid at altitudes considered (below 60 km) since the nighttime electron conductivity is negligible.

An important property of the electric field $E(z,t)$ at any altitude $z \le 60$ km where the relaxation time $\tau_R(z) = \varepsilon_0/\sigma(z)$ exceeds the lightning discharge time τ_L (typically τ_L is up to few milliseconds) is that the time peak $E_{peak}(z)$ reached by $E(z,t)$ persists approximately during the time interval $[\tau_L, \tau_R(z)]$. The inception time and velocity of the positive streamers of a sprite ensure that these streamers 'catch' the peak electric field E_{peak} at all altitudes below 60 km. Hence, the applied electric field at altitude z included in condition (1) is $E_{peak}(z)$.

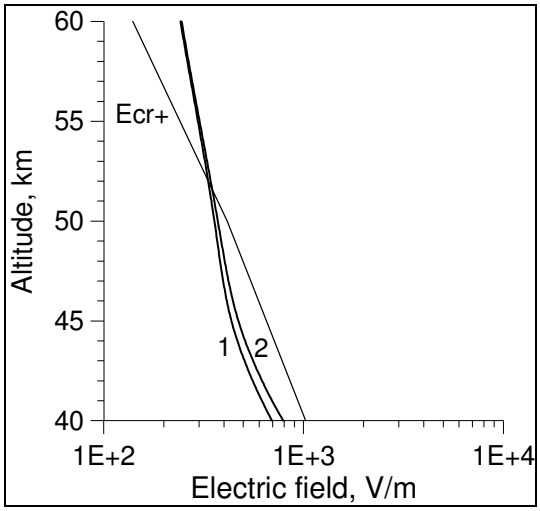

Figure. Peak QS electric field E_{peak} as function of altitude by maximum (curve 1) and minimum (2) solar activity generated by +CG lightning discharges from height 10 km by initial charge 100 C removed in time τ_L=1 ms. The thin line is for the threshold field E_{cr+} needed for propagation of a positive streamer.

The Figure shows the results for the height profiles of the peak QS electric field $E_{peak}(z)$ generated by the same parameters as in of the sprite-producing +CG lightning discharge and atmospheric conductivity profiles corresponding to solar minimum and solar maximum. Both profiles of E_{peak} are compared with the profile of E_{cr+}. The termination height z_T is obtained from condition (1) in each case. During solar minimum the termination height z_{Tmin} is by 0.4 km lower than that (z_{Tmax}) during solar maximum, due to change of E_{peak} by ~2%. This shows that even very small changes in E_{peak} (here they are due to SA change) can lead to significant

change of the termination height $\Delta z_T = z_{T\,max} - z_{T\,min}$, since the scale-heights of E_{cr+} and E_{peak} are close. The results obtained further are for a representative set comprising relevant intervals of variation of the parameters responsible for sprites.

Estimation of change of termination height

The change $\Delta z_T = z_{Tmax} - z_{Tmin}$ of termination height by transition from minimum to maximum SA by otherwise equal conditions (which concern the causative flash and conductivity) is obtained as follows:

$$\Delta z_T = \ln (C_E)\ H_E\ H_{Ecr} / (H_E - H_{Ecr}) \qquad (2)$$

Here H_E and H_{Ecr} are the scale-heights corresponding to the profiles of the electric fields $E_{peak}(z)$ and $E_{cr+}(z)$. H_{Ecr} is equal of the scale-height of N (between 40 and 60 km $H_{ecr} \sim -7.8$ km). H_E is represented by the expression $H_E(z) = [\ d \ln (E_{peak}(z) / \underline{dz})\ ]^{-1}$. $C_E(z)$ is the ratio between E_{peak} values at altitude z obtained by maximum and minimum SA, $C_E = E_{max}/E_{min}$ where E_{max} and E_{min} are the peak QS electric fields by maximum and by minimum SA. To determine C_E in Expr.(2), E_{peak} is estimated by different parameters of the causative +CG lightning discharge and conductivity profile. At an altitude z below 60 km the peak electric field E_{peak} does not depend on the actual lightning current waveform; it depends only on the initial charge Q_0 removed by lightning and on its altitude z_Q. We thus can assume that the charge decreases exponentially in time, $Q(t) = Q_0 \exp(-t/\tau_L)$. The 'profile' E_{peak} ($z \le 60$ km) is obtained as function of the lightning discharge parameters Q_0 and z_Q and of the average scale height h_σ of the conductivity between altitudes z_Q (height of the cloud charge Q_0) and z, $h_\sigma = (z - z_Q)/\ln[\sigma(z)/\sigma(z_Q)]$. Below ~60 km E_{peak} can be approximated in the form:

$$E_{peak} = Q_0\, P(\zeta_Q, \zeta_L, \zeta) / h_\sigma^2$$

where $\zeta = z/h_s$, $\zeta_Q = z_Q/h_s$, $\zeta_L = z_L/h_s$ are the dimensionless parameters. Below 60 km:

$$E_{peak}(\zeta_Q, \zeta) = Q_0\, C_R(z)\, P_0(\zeta_Q) \exp[z/(h_\sigma H_P)] / h_s^2 \qquad (3)$$

Here

$P_0(\zeta_Q) = 0.1547\zeta_Q^3 - 0.160\zeta_Q^2 + 2.345\zeta_Q$; $H_P(z_Q) = -0.04\zeta_Q^3 + 0.1022\zeta_Q^2 - 0.1065\zeta_Q + 2.272$

$C_R(z)$ is a correction coefficient which takes into account the influence of the conductivity profile and electric field below the height z_Q of the change:

$$C_R(z) = [R_e(0, z_Q)\, R(z_Q, Z_I)] / [R(0 < z < z_Q)\, R_e(z_Q < z < Z_U)],$$

$R[z_1, z_2]$ is the columnar electric resistance in the interval $[z_1, z_2]$ computed for the actual conductivity profile, and $R_e[z_1, z_2]$ is the one computed by exponential approximation of the same profile. It is derived from Expr.(3) that $H_E = h_\sigma H_P$. Typically, $h_\sigma \sim 4 - 6.5$ km, and $H_P \sim 3.4 - 3.6$ by absolute value, i.e. $|H_E| \sim 17 - 20$ km. It follows from (3) that the change of the SA level from SA minimum to maximum can lead to an increase or to decrease of the termination height depending on the sign of the difference $h_{\sigma max} H_{Pmax} - h_{\sigma min} H_{Pmin}$

Results and conclusions

For a representative estimation of z_T and $\Delta z_T = z_{max} - z_{min}$ due to transition from minimum to maximum SA eight cases are considered by varying the charge's altitude z_Q ($z_Q = 8$ km and 10 km), the total charge Q_0 removed by lightning ($Q_0 = 75$ C and 100 C), and the coefficient C_σ of reduction of conductivity in cloud ($C_\sigma = 0.2$ and 0.1, McGorman and Rust, 1998). The conductivity profiles $\sigma_{min}(z)$ and $\sigma_{max}(z)$ are obtained by respective modification of the basic profile $\sigma(z)$ obtained by measurements in a rocket experiment above a nighttime thunderstorm on Wallops Island (37.8°N, 75.5°W) at altitudes 18 - 70 km (Holzworth et al., 1985). The results for z_{min}, z_{max} and Δz_T for each case are given in the Table.

Table. Streamer termination heights z_{Tmax} and z_{Tmin}, and Δz_T by different model parameters

C_σ	z_Q, km	Q_0, C	z_{Tmax}, km	z_{Tmin}, km	Δz_T, km
0.2	8	75	56.1	56.3	–0.2
		100	49.5	49.6	–0.1
	10	75	51.8	51.5	0.3
		100	45.8	45.2	0.6
0.1	8	75	55.3	55.6	–0.3
		100	48.8	50.0	–0.2
	10	75	51.1	50.6	0.5
		100	45.0	44.2	0.8

In cases of higher located and larger charge Q_0 the streamers of a sprite reach lower altitudes by minimum solar activity (the vertical sprite extension is larger) than by maximum SA. The change of termination height Δz_T in considered cases reaches 0.8 km By the decrease of charge height and magnitude (by weaker sprites) the effect of variation of SA on the termination height diminishes and reverses its sign: during maximum SA the streamer termination height is slightly lower (few hundreds of meter) that that during minimum SA. The obtained results show that the suggested link between solar activity and the chemistry balance in lower mesosphere and upper stratosphere realized by sprites is not effective; a minor effect is possible only in regions at middle and higher geomagnetic altitudes, yet of large sprite activity.

References:

Arnone, E., A. Kero, et al. (2008), Seeking sprite-induced signatures in remotely sensed middle atmosphere NO2, *Geophys. Res. Lett.*, 35, L05807, doi:10.1029/2007GL031791.

Chen A.B., C.-L. Kuo, et al., (2008). Global distributions and occurrence rates of transient luminous events *J. Geophys. Res.*, 113, A08306, doi:10.1029/2008JA013101.

Hiraki, Y., Y. Kasai, H. Fukunishi, 2008. Chemistry of sprite discharges through ion-neutral reactions, *Atmos. Chem. Phys.*, 8, 3919–3928.

Holzworth, R.H., Kelley, M.C., et al. (1985). Electrical measurements in the atmosphere and the ionosphere over an active thunderstorm. 2.Direct current electric fields and conductivity. *J. Geophys. Res.*, **90**, 9824-9837 .

Li, J., and S. A. Cummer (2009), Measurement of sprite streamer acceleration and deceleration, *Geophys. Res. Lett.*, 36, L10812, doi:10.1029/2009GL037581.

Tonev P.T., P.I.Y. Velinov (2007). Atmosphere–ionosphere vertical electric coupling above thunderstorms of different intensity, *J. Atmos. Solar-Terr. Phys.*, **69**, 2007, 1203-1212.

MacGorman, D. R. and W. D. Rust, Electrical Structure of Thunderstorms, Oxford University Press, 1998, 432 p.

Coherent structures in the Es layer and neutral middle atmosphere

Zbyšek Mošna, Petra Koucka Knížová, Kateřina Potužníková

Department of Aeronomy, Institute of Atmospheric Physics, ASCR, Prague, Czech Republic
E-mail: zbn@ufa.cas.cz

Abstract.

The present paper shows results from the campaign performed during geomagnetically quiet period from June 1 to August 31, 2009. Within time-series of stratospheric and mesospheric temperatures at pressure levels 10 hPa to 0.1 hPa, mesospheric winds measured in Collm, Germany, and the sporadic E-layer parameters foEs and hEs measured at the Pruhonice station we detected specific coherent wave-bursts in planetary wave domain. Permanent wave-like activity is observed in all analyzed data sets. However, number of wave-like structures persistent in large range of height from the stratosphere to lower ionosphere is limited. The only coherent modes that are detected on consequent levels of the atmosphere are those corresponding to eigenmodes of planetary waves.

Introduction

Sporadic E layers (Es) are thin sheets of enhanced electron and metallic ion concentration located in the ionospheric E region. The critical frequency foEs (maximum plasma frequency of the layer) often exceeds the critical frequency of the E, or even F layer. The Es layer formation have been explained as a result of wind shear induced ionization transport (Whitehead, 1989; Axford, 1963). Vertical plasma drift leading to the ion convergence is controlled mainly by the zonal and meridional winds, when westward (northward) winds induce a downward, and eastward (southward) winds induce upward motion of the ions. The Es parameters foEs and hEs follow a regular daily pattern (Fig. 1) which is controlled mainly by wind shears in the lower thermosphere (Axford (1963); Whitehead (1989)). Further, they are driven by a longer-lasting neutral wave activity in the stratosphere and mesosphere. Review of Es behavior can be found in Haldoupis (2011).

Tidal and planetary waves

Mesosphere and Lower Thermosphere region (MLT) are significantly influenced by atmospheric waves. Well known and pronounced are diurnal solar tides and their harmonics (semidiurnal and terdiurnal tides). Planetary waves (PW) are large scale oscillations in the atmosphere usually with eigen-periods 2, 4, 5, 10, and 16 days (Forbes, 1995). They are responsible for a large part of energy transport between atmosphere regions in horizontal and vertical direction. They are forced in the troposphere by the topography, synoptic situation, or

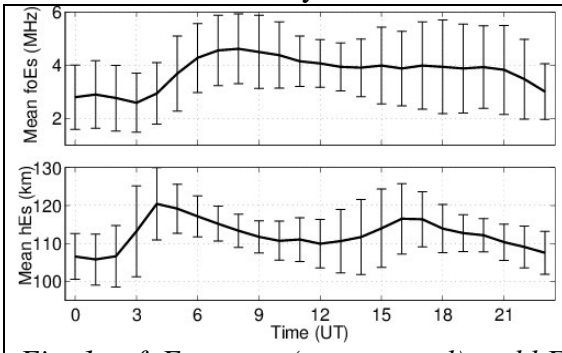

Fig. 1. – foEs means (upper panel) and hEs means (bottom panel) from summer 2009 measurement at Pruhonice. Vertical lines denote one standard deviation.

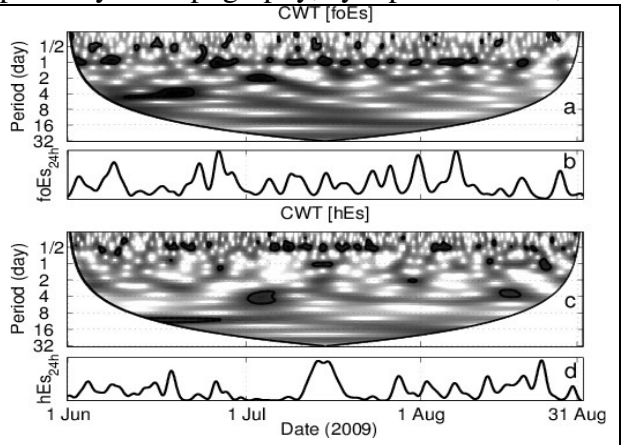

Fig. 2 - CWT of foEs (a) and hEs (c). Panels (b) and (d) show integrated power content at periods 23-25 h.

temperature differences between the sea and continents. Nonlinear efects in the terdiurnal tides excitation were proposed by (Jacobi and Fytterer, 2012). The amplitudes and vertical wavelengths of the terdiurnal tide depend strongly on season, latitude, and altitude. Arras et al. (2009) within GPS radio occultation data detected semidiurnal tidal response in the Es layer. Fytterer et al. (2014) used GPS observations and found that the migrating terdiurnal tides influence the Es formation at lower and midlatitudes at heights above 100 km. The effect of PW to the Es region was explained by acting of diurnal and semidiurnal tides modulated by the PW. Sauli and Bourdillon (2008) described tidal and planetary wave periodicity in the foEs and hEs (height of the Es layer) data. They attributed variability of diurnal mode to the Doppler-shift caused by 5 day planetary wave. Mosna and Koucka Knizova (2012) studied diurnal and planetary wave influence on the Es region represented by the foEs and hEs parameters. They found both coherent oscillations at diurnal period (and its harmonics) in the Es data and temperature data at the 10 hPa pressure level (approximately 30 km) at periods close to planetary eigen-periods by means of wavelet coherence.

Data and Method

We used critical frequencies foEs and heights hEs of the Es layers from June 1 to August 31, 2009. The ionospheric measurement was performed at the station Pruhonice (50°N, 15°E, LT = UT+1H) using the digisonde DPS-4. Es layer was almost permanently present. Time resolution of the measured and manually processed ionospheric data was 15 minutes, however we used 3h resolution for the analysis from time corresponding to wind and temperature data. The summer 2009 was generally of low geomagnetic activity. The neutral atmosphere data are represented by the temperature at pressure levels at 10 hPa, 5 hPa, 1 hPa, and 0.1 hPa corresponding roughly to 32 km, 37 km, 48 km, and 65 km, respectively. The temperatures are derived from the MERRA reanalysis for the grid point located at 50°N 15°E corresponding to the Pruhonice station and have 3 hour time resolution. The wind activity was described by means of prevailing meridional and zonal wind velocity (mean night velocity) measured at Collm, Germany (51.3°N, 13.0°E) using VHF meteor radar (Jacobi, 2012) at 82, 85, 88, 91, and 94 km. For description of wave activity in the data and detection of coherent structures we use methods of continuous wavelet transform and wavelet coherence applied in paper of (Mosna and Koucka Knizova (2012), Chapter 3. Method). Extension to the atmospheric applications can be found in (Torrence and Compo, 1998; Grinsted et al., 2004). To keep this paper consistent with the four above cited papers, we use the following acronyms CWT (Continuous Wavelet Transform) and WTC (Wavelet Transform Coherence). WTC shows how coherent the cross wavelet transform is in time period space. The wavelet coherence can be understood as localized correlation coefficient in time- frequency space. All plots showing CWT and WTC results are normalized to maximum value for all data or pairs of data (unitless representation).

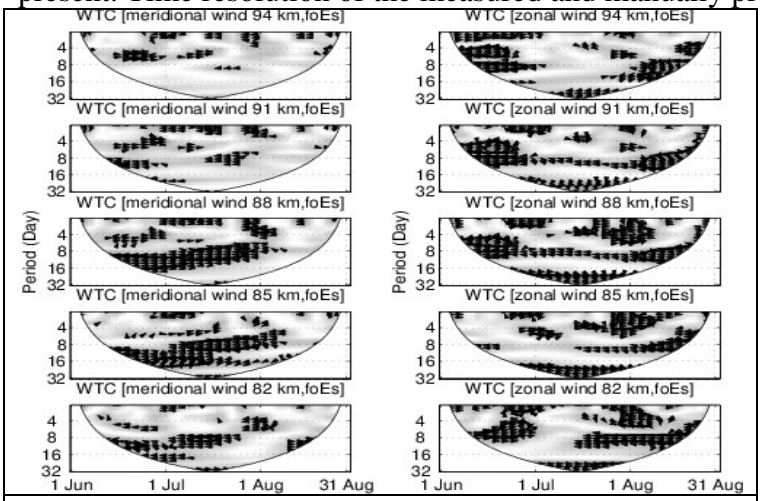

Fig. 3 - Wavelet coherence between meridional wind and foEs (left panels) and zonal wind and foEs (right panels) at different height levels.

Results and discussion

The sporadic E layers are controlled mostly by the diurnal tide which becomes dominant below 120 km, whereas the 12 h periodicity in Es is caused by the Descending Intermediate Layers (DILs) which are initiated by semidiurnal tides in the upper E region and move downward acting as parenting process for Es in the lower E region. Regarding shorter periods, published evidence about tide-like variations in sporadic E, e.g. 8 and 6 h periodicities, is rather limited (Haldoupis and Pancheva, 2006).

Continuous wavelet transform (CWT)

CWT of the sporadic E data reveals most dominant and stable periodicity at the tidal domain (Fig. 2). Pronounced terdiurnal, semidiurnal, and diurnal periods are present in both foEs and hEs data. The most prominent period in the foEs data is diurnal period, the most dominant period in the hEs data is the semidiurnal period. Further peaks are located at a wide band equal or above 2 days (2-3, 5, 10-16 days, Fig. 2 panels a and c). CWT of temperature data shows significant oscillations corresponding to the semidiurnal and diurnal domains. In temperature data at 0.1 hPa and 1 hPa, the semidiurnal period dominates over the diurnal period. Persistent wave-like domains are further located to the 2 day oscillation (0.1 hPa, 1 hPa, and 0.1 hPa), 3-4 day oscillation (10 hPa), 5 day oscillation (all temperature data) and 10 day oscillation (all temperature data, very strong for 1 and 5 hPa and with a prolonged period towards 16 days for 10 hPa). CWT of zonal and meridional wind data shows dominant periods at 2, 3-5, and 8 days. Zonal wind data show high power content at a band above 16 days and about 4-7 days peak in the middle of June at heights 88-94 km. Increased power in meridional winds at periods 8-10 days is present in the middle of July at heights 82-88 km.

Wavelet coherence (WTC)

WTC of temperature data and Es data intensifies at periods corresponding to semidiurnal, and diurnal waves. In planetary wave domain were detected oscillations at period 2 days and 5 days (all pairs of Es data and T except 10 hPa level). Bursts of common oscillations were localized at about 10 and 16 day period and wide bands of period above 16 days were present in WTC [T(0.1hPa),foEs] and WTC [T(1hPa,foEs)]. Wavelet coherence was further performed on both zonal and meridional wind data and Es parameters. 7-9 day periodicity was observed in all pairs wind vs. Es parameters. Meridional wind and foEs exhibit coherent 5 day periodicity for all height levels (Fig. 3, left panels). Meridional wind and hEs (not shown here) have coherent structures at 3-4 days and 7-8 days (heights 82 - 91 km). While some time-period domains vary with height levels of the neutral atmosphere data, there are several domains which are stable over whole or large vertical span. Coherent wave bursts can be found in all data pairs WTC [T,foEs] and WTC [T,hEs] at all pressure heights. Only those coherent structures which are present in at least three consequent height (pressure) levels are selected. These structures correspond to periods close to eigen modes of the PW. They seem to propagate upwards to the Es region where they influence/modify both height of the Es layer and maximum concentration of the Es layer.

Conclusion

We used stratosphere and mesosphere temperature data and mesosphere wind data as representatives of the neutral atmosphere, and critical frequency and height foEs and hEs representing ionospheric Es layer. Various areas of high coherence between neutral atmosphere and Es parameters exist in the whole studied vertical profile. However, only limited dominant periods detected in temperature and wind data coherent with the Es data were persistent along the vertical profile. Hence, we are able to detect them on several height (pressure) levels. These periods (2, 5, 9-10, and 15 day) correspond to the planetary eigen-modes. It confirms close relationship between planetary wave activity and sporadic E

properties and agrees with results proposed in Pancheva et al. (2003); Voiculescu et al. (2000); Mosna and Koucka Knizova (2012).

Acknowledgement: Authors acknowledge providing Collm meteor radar wind data by Prof. C. Jacobi of the Institute for Meteorology, University of Leipzig. This work was supported by Grant P210/12/2440, Grant of Ministry of Education, Youth and Sport (LG 13042) and Grant 16-24688S of the Grant Agency of the Czech Republic.

References

Arras, C., Jacobi, C., Wickert, J., 2009. Semidiurnal tidal signature in sporadic E occurrence rates derived from GPS radio occultation measurements at higher midlatitudes. In: Annales geophysicae. Vol. 27. Copernicus GmbH, pp. 2555-2563.

Axford, W. I., 1963. The formation and vertical movement of dense ionized layers in the ionosphere due to neutral wind shears. Journal of Geophysical Research 68 (3), 769-779.

Forbes, J. M., 1995. Tidal and planetary waves. The upper mesosphere and lower thermosphere: a review of experiment and theory, 67-87.

Fytterer, T., Arras, C., Homann, P., Jacobi, C., 2014. Global distribution of the migrating terdiurnal tide seen in sporadic e occurrence frequencies obtained from gps radio occultations. Earth, Planets and Space 66 (1), 1-9.

Grinsted, A., Moore, J. C., Jevrejeva, S., 2004. Application of the cross wavelet transform and wavelet coherence to geophysical time series. Nonlinear processes in geophysics 11 (5/6), 561-566.

Haldoupis, C., 2011. A tutorial review on sporadic E layers. In: Aeronomy of the Earth's Atmosphere and Ionosphere. Springer, pp. 381-394.

Haldoupis, C., Pancheva, D., 2002. Planetary waves and midlatitude sporadic E layers: Strong experimental evidence for a close relationship. Journal of Geophysical Research: Space Physics (1978-2012) 107 (A6), SIA-3.

Jacobi, C., 2012. 6 year mean prevailing winds and tides measured by vhfmeteor radar over collm (51.3n, 13.0e). Journal of Atmospheric and Solar-Terrestrial Physics 78, 8-18.

Jacobi, C., Fytterer, T., 2012. The 8-h tide in the mesosphere and lowerthermosphere over Collm (51.3N; 13.0E), 2004-2011. Advances in Radio Science 10 (22), 265-270.

Lastovicka, J., 2006. Forcing of the ionosphere by waves from below. Journal of Atmospheric and Solar-Terrestrial Physics 68 (3), 479-497.

Mosna, Z., Koucka Knizova, P., 2012. Analysis of wave-like oscillations in parameters of sporadic E layer and neutral atmosphere. Journal of Atmospheric and Solar-Terrestrial Physics 90, 172-178.

Pancheva, D., Haldoupis, C., Meek, C., Manson, A., Mitchell, N., 2003. Evidence of a role for modulated atmospheric tides in the dependence of sporadic E layers on planetary waves. Journal of Geophysical Research: Space Physics (1978-2012) 108 (A5).

Sauli, P., Bourdillon, A., 2008. Height and critical frequency variations s of the sporadic-E layer at midlatitudes. Journal of Atmospheric and Solar-Terrestrial Physics 70 (15), 1904-1910.

Torrence, C., Compo, G. P., 1998. A practical guide to wavelet analysis. Bulletin of the American Meteorological Society 79 (1), 61-78.

Voiculescu, M., Haldoupis, C., Pancheva, D., Ignat, M., Schlegel, K., Shalimov, S., 2000. More evidence for a planetary wave link with midlatitude E region coherent backscatter and sporadic E layers. In: Annales Geophysicae, 18, 1182-1196.

Whitehead, J., 1989. Recent work on mid-latitude and equatorial sporadic-E. Journal of Atmospheric and Terrestrial Physics 51 (5), 401-424.

Annual Tree Rings Widths and the "Sun-Climate" Relationship

Boris Komitov[1], *Peter Duchlev*[1], *Daniela Kirilova*[1], *Georgi Byandov*[2], *Nadya Kiskinova*[2]

[1]Institure of Astronomy and NAO - Rozhen, Bulgarian Academy of Sciences, Bulgaria,
[2]Astronomical Observatory "Yuri Gagarin", Stara Zagora, Bulgaria
E-mail: b_komitov@sz.inetg.bg

1. Introduction

The annual tree rings widths are ones of the good proxies for the climate changes as well as for the "Sun-climate" relationships and solar and geomagnetic activity in the past (Fritz et al., 1976; Rasspopov et al., 2008). The aim of this work is the presentation of results obtained from the measurements of annual rings widths of 44 tree samples, taken mainly from the mountain part of Bulgarian territory. There are 32 beech (Fagus), 11 oak (Quercus robur) and 4 pine (Pinus) samples (see Komitov et al., 2014a). The results in the light of the possible scenarios for solar activity and climate changes during the next few decades are discussed.

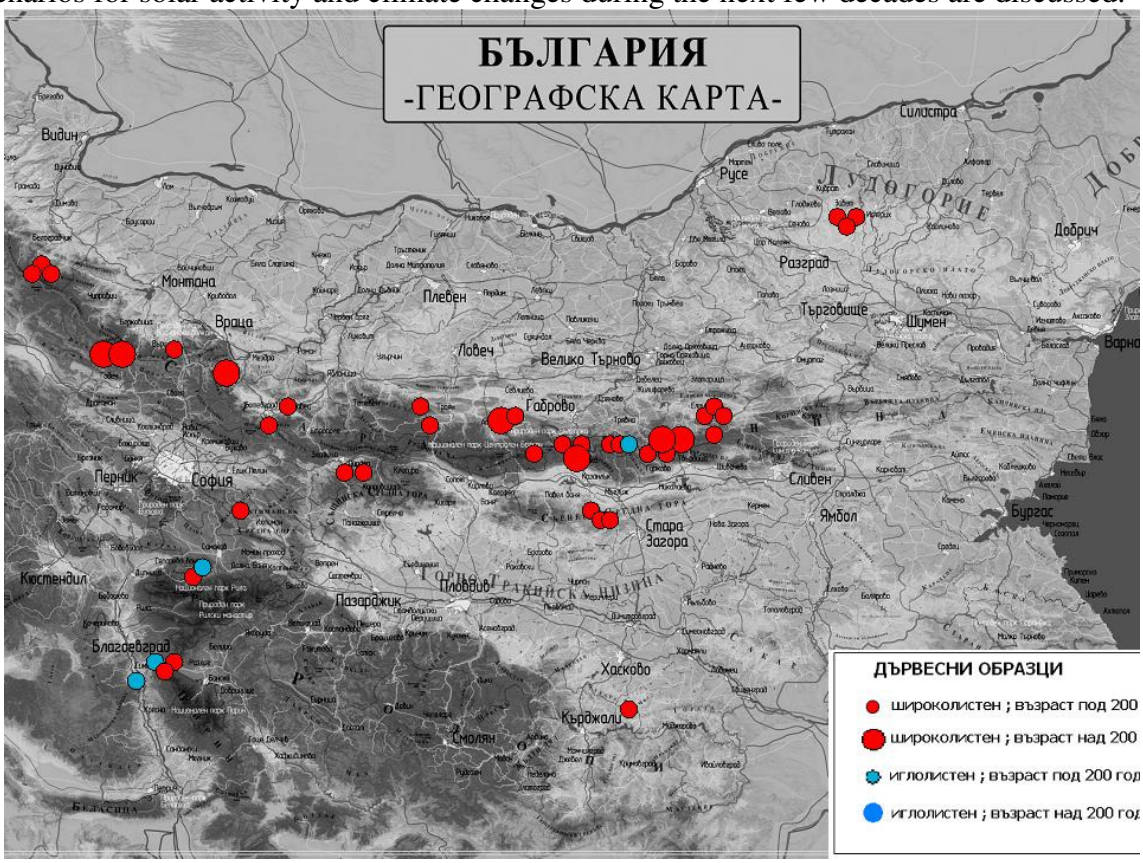

Fig. 1 The tree samples sites (red circles – beech and oak, blue circles - pine). The samples are signed by large circles.

2. Data and methods

From 1 to 8 radial profiles (depending on the quality of surface structure) of annual tree rings widths for each sample are measured. On this basis for each sample an averaged and smoothed by 5 years the radial profile (time series) has been obtained. These time series for existing in them of statistically significant trends and cycles has been investigated. The T-R periodogramm procedure for time series analysis (Komitov 1986, 1997) is used. On the basis of these results kinematical models of annual tree rings widths time series for the growth of two beech samples (Gurkovo-01 and Rositsa-01) were built. The latter are extrapolated for the next few decades. A climatic calibrations, based on instrumental data for rains and temperatures in near placed meteorological stations has been made for these time series.

That's why predictions about the possible climatic changes in Bulgaria into the warm season (May October) as well as for the solar and geomagnetic activity are possible. The full description of used methods and quantities is given in the study of Komitov et al. (2014b).

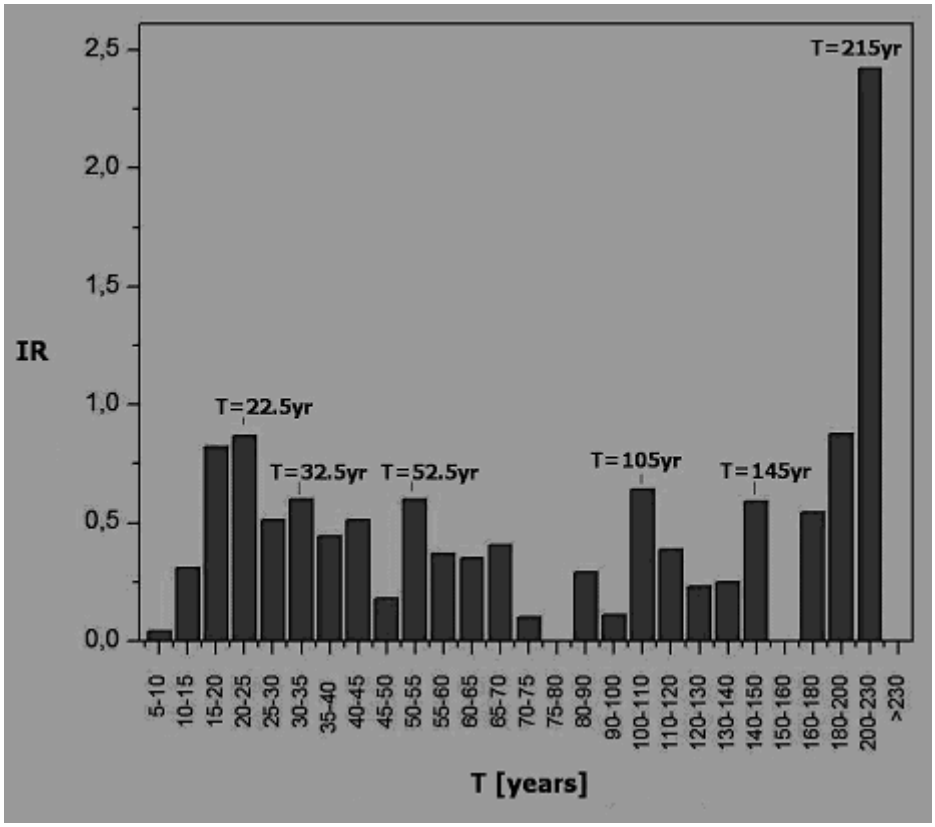

Fig. 2 The "index of expression" distribution (see Komitov et al, 2014a) IR for statistically significant cycles in the range 2 < T < 250 years

3. Results and analysis

A. On the base of the all 44 tree rings widths time series analysis it has been found that the best expressed oscillation in the sub centurial range is by length of ~ 22 years and also corresponds well to the solar magnetic 22yr (Hale) cycle. The above mentioned cycle is essentially better expressed if only the samples from South Eastern Bulgaria are taken into account.

B. There are also certain traces of cycles by length T of ~ 32.5, 52.5, 105, and 145 years.

C. For 6 of the all 7 oldest (age over 200 years) tree samples a presence of quasi sinusoidal trend –"hypercycle" with duration of $T \approx 215$ yr is detected too. The last one is in a good coincidence by phase with the solar 200-210 yr cycle, which is detected in almost all indirect ("historical") solar activity data series for "cosmogenic" isotopes (^{14}C and ^{10}Be), as well as in messages about aurora in Ancient and Middle Ages (Damon and Sonett, 1991; Dergachev and Chistyakov, 1993; Damon et al, 1997; Schove, 1955, 1983).

D. For the 7 all oldest (age over 200 years) samples a well – expressed minimum in annual rings width between 1795 and 1830 AD is also detected. It corresponds for generally dry summers during the start and end of so called solar "Dalton minimum". To our opinion traces of temporary increasing of tree rings widths in the course of sunspot cycle No 6 (1810 – 1823 AD) and near to the "Year without Summer" (1816 AD) are visible in different degree in all of these 7 longest time series.

E. The extrapolation of the annual rings width series kinematical model of our first tree sample (Gurkovo-01) (which was taken in 1983 AD) as an "epignosis" test has been used

for the epoch after 1980 and up to 2012 AD. A continuous epoch of dry and warm summers with short temporary breaking near to 2002-2005 AD has been predicted. As it is shown from the real instrumental meteorological data during the period 1980- 2013 AD the coincidence between this prediction and the real climate dynamics is very good.

F. The extrapolation of kinematical model for the sample Rositsa-01 about the epoch 2013 up to 2045 AD indicate for cooler and wet summers in Central North Bulgaria during the next tree decades. The corresponding tendencies should be very slow from 2013 to 2030 AD and with small 20-22 yr cycle contribution. It is an indication for weak solar cycles No 24 and 25. According to the model an essentially sharpen rainfall increasing should be expected after 2030 AD. It could be related to a very pecular structure of the pair solar cycles No 26 and 27.

REFERENCES

Damon, P. E. and Sonett, C. P., 1991, in *The Sun in Time*, eds.Sonett., C. P., Giampapa, M. S.

Damon, P., Periestykh, A., and Meese, D., 1997, 10Be/g:Production vs Accummulation in Recording the Schwabe and Hale Cycles, preprint (presented in 18th IAGA Assembly, Aug.1997, Uppsala)

Dergachev, V. A. and Chistyakov, V. F., 1993, *Izvestiya FTI*, 112. (in Russian)

Frittz, H., 1976, Tree Rings and Climate, Subsidiary of Harcourt Brace Jovanovich Publisher, London, New York, San Francisco.

Komitov, B., 1986, *Soln. Dannye Byull.* No 5, 73-78. (in Russian)

Komitov, B., 1997, *Bulg. Geophys. J.* 23, 74-82.

Komitov B., Duchlev, P., Kirilova, D., Bonev, T., Byandov, G., Kiskinova, N., Petrov, N., Nikolov, P., Tsvetkov Ts. and Stoycheva, A., 2014a, Catalog of tree samples, taken in 2013 AD in territory of Bulgaria , Alpha Visia, St. Zagora, Bulgaria. (in Bulgarian)

Komitov, B., Duchlev, P., Kirilova, D., Byandov, G. and Kiskinova, N., 2014b, The "Sun-Climate" connection and annual tree rings, Alpha Visia, St. Zagora, Bulgaria. (in Bulgarian)

Křivský, L. and Pejml, K.,1988, Solar activity, aurorae and climate in Central Europe in the last 1000 years, Bul.Astron. Inst. Chechosl. Acad. Sci., No75.

Rasspopov, O.M., Dergachev, V.A., Esper, J., Kozyreva, O., Frank, D., Ogurtsov, M., Kolstrom, T., Shao, X., 2008, *Palaeogeography, Palaeoclimatology, Palaeoecology* 259,16.

Schove, D. J., 1955, *J. Geophys. Res.* 60, 127.

Schove, D. J., 1983, *Sunspot Cycles* (Stroudsburg: Hutchinson Ross, Pennsylvania.)

Tropospheric systems influence on the ionospheric plasma

Koucká Knížová, P., Mošna, Z., Kouba, D., Potužníková, K., Boška, J.

Institute of Atmospheric Physics Czech Academy of Sciences, Prague, Czech Republic
E-mail: pkn@ufa.cas.cz

Abstract.

Correlation of long time series of the critical frequencies from European stations of vertical sounding is analysed with respect to latitudinal and longitudinal difference and surface distance of stations. Coefficients are high for raw data, subtracted mean courses but for fluctuations around mean as well. At the surface distance exceeding 1000km and/ or about 10 degrees of latitudinal difference between stations, the correlation coefficient of fluctuations decrease rapidly. As a possible source of the common influence on scale 1000km/10 degree we propose tropospheric systems that are known to be an important source of atmospheric waves in a broad period range. Large tropospheric mesoscale systems have typically up to 2000 km in diameter.

Introduction.

The most important factors that affect ionosphere are related solar and geomagnetic activity. However, the influence of the lower atmosphere through thermospheric chemistry and dynamics cannot be neglected. Within regions with collision dominated plasma (D and E regions) the influence is stronger than in the above laying regions F1 and F2.

Atmospheric waves propagating upward from the source region play an important role (see for instance Yigit and Medvedev, 2015). Their energy tends to be conserved and consequently the amplitude grows due to the decreasing atmospheric density. It has been proven experimentally that some atmospheric waves are able to penetrate up to the F2 layer height (Altadill et al., 2004; Boska and Sauli, 2001; Forbes and Leveroni, 1992; Forbes et al., 2000; Lastovicka and Sauli, 1999; Pancheva et al., 1994; Radicella et al., 2009; Sauli and Boska, 2001; among others).

Atmospheric waves.

Meteorological processes in the lower-lying layers, affect the ionosphere predominantly through the upward propagating waves and their modifications and modulations. Origin of the atmospheric waves is in periodic heating and cooling of the Earth atmosphere and surface and/or dynamics. Atmospheric waves propagate into the ionosphere mostly directly but the planetary waves can propagate upwards to the F region heights only indirectly, via various potential ways like modulation of the upward propagating tides. A review of the ionosphere forcing from lower laying atmosphere is provided by Lastovicka (2006). Troposphere is the most important region from where the atmospheric waves propagate upward. As the most important tropospheric sources of atmospheric waves especially gravity waves, topography, convection and wind shear (Fritts and Nastrom, 1992; Nastrom and Fritts, 1992) and jet stream (Fritts and Luo, 1992; Luo and Fritts, 1992) are identified.

Data.

For our analysis we use critical frequency (foF2) in the F2 around noon (mean value out of 10LT-14LT) from 15 European stations. These stations are following Arkhangels, Dourbes, Kaliningrad, Kiev, Lannion, Leningrad, Lycsele, Moscow, Paris, Poitiers, Pruhonice, Rome, Sodankyla, South Uist and Uppsala. Each time series cover at least one solar cycle, both periods of low and high solar activity

Method.

As in the paper Roux et al. (2012) time series of foF2 were split into long term and short term fluctuations and further analysed. The correlation coefficients were computed for all pairs of stations for original (raw) data, means, and fluctuations. Further, for all data the Continuous Wavelet Transform (CWT) and Wavelet Coherence (WTC) are computed. Detail description of wavelets can be found in Mallat (1998), Torrence and Compo (1998), Grinsted et al. (2004).

Results – Pearson correlation.

As in Roux et al. (2012) the correlation coefficients are high for all raw data, means and fluctuation derived from the foF2 series. Correlation coefficients of fluctuations are located into interval (0.2; 0.8). The highest correlation coefficients (close to 0.8) could be found only for latitudinal difference up to 5 degrees. For larger distances exceeding 5 degrees all the correlations decrease rapidly. In case of longitudinal dependency of the correlation coefficients, the highest values are up to the difference 10 degrees. Then the correlation coefficients decrease. The latitudinal decrease of correlation coefficient is faster than longitudinal. The same holds for correlations of raw data and trends.

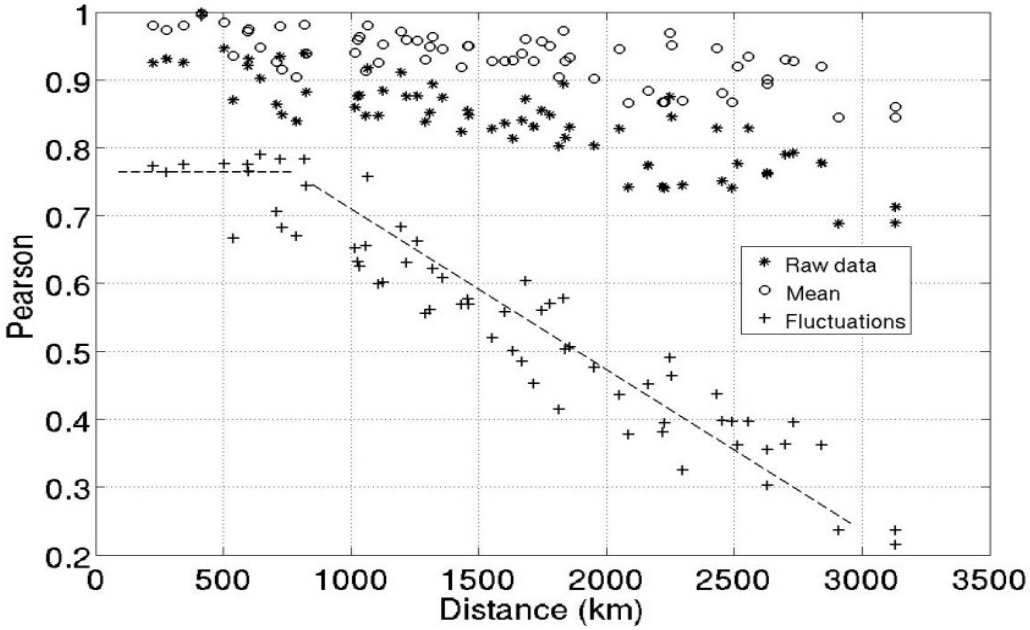

Figure 1. Correlation coefficient dependence on the surface distance.

On the plot of correlation coefficients with respect to actual surface (Fig.1.) the above described behaviour is even more significant. There is an evident change of the behaviour around distance 1000km. Supreme values (exceeding 0.7) of correlation are detected up to distance 1200 km. It holds for raw, mean and fluctuation correlations. Behaviour is best pronounced on fluctuations.

Results - Wavelet Transform Coherence.

Figure 2 shows an example of the WTC computed for pairs of stations Pruhonice-Rome (upper panel) and Pruhonice-Sodankyla (middle panel) on time scales between 4 and 64 days. Latitudinal differences of the stations are 7 degrees and 17 degrees, respectively. Surface distance of Pruhonice and Rome is 920 km, and Pruhonice and Sodankyla the distanceis 2050 km.

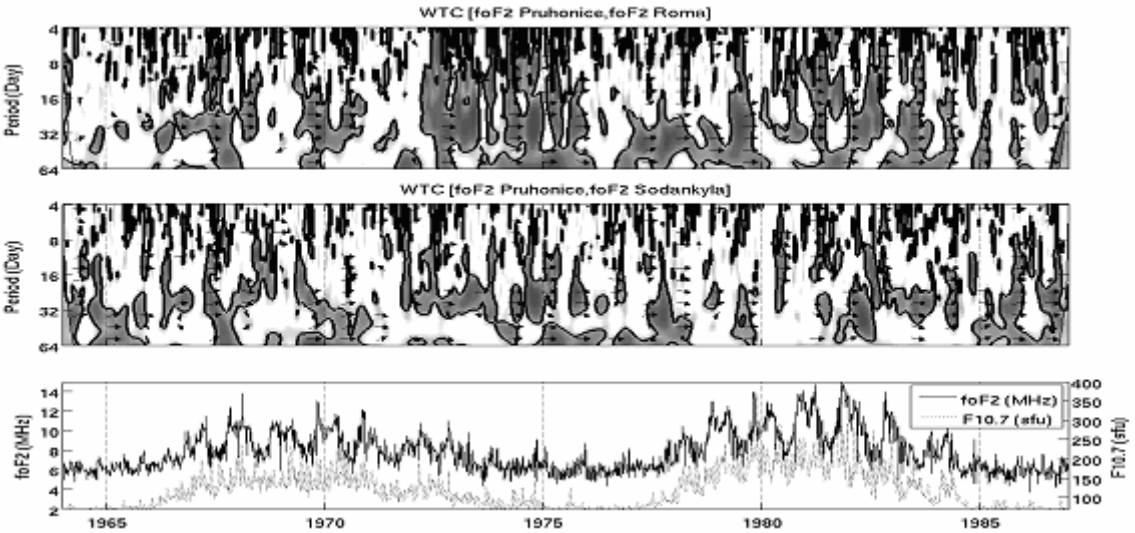

Figure 2. Wavelet Transform Coherence of time series of foF2 for pairs of stations Pruhonice-Rome and Pruhonice-Sodankyla.

On the bottom plot, foF2 from the Pruhonice and solar flux f10.7, are plotted together. On both WTC spectra there are areas of high common power. High WTC close to 27-day period is well seen on both spectra. WTC (Pruhonice, Rome) shows larger areas of coherency than WTC (Pruhonice, Sodankyla). WTC varies with the solar cycle. The largest areas of common coherent oscillations can be found on the descending phase of solar cycle (1973-1978).

Tropospheric mesoscale systems.

Lower atmospheric processes occur on wide range of spatial and temporal scales. The tropospheric phenomena are classified according to time and space scales in Orlanski (1975). Mesoscale processes represent motions of the order up to 2000 km on the horizontal scale and several days on the time scale. Hurricanes and frontal systems are representative phenomena of such processes.

Europe is influenced by various types of weather air-mass. The air circulation over Europe has a seasonal rhythm, which reflects the influence of the Arctic, polar and tropical air masses. It is dominated by western flow at the surface and also in the upper atmosphere. The cyclogenic processes strongly interact with significant orography, specifically the Alps and Pyrenees mountains (Kaspar and Muller, 2010). The most typical features of European weather is great variability (Bluestein, 1993; Hidore et al., 2009).

Conclusion.

On the plots of correlation coefficients we show an important change of behaviour at 1000 km surface and/or longitudinal distance 10 degrees. Up to the 1000 km surface and/or longitudinal distance 10 degrees the correlation coefficients are extremely high for raw, mean and even for fluctuations. Then they rapidly decrease. WTC of station pairs show areas of common high coherency within the analysed time range especially for periods of solar minima for time scales below 2 months. Higher power is found for closer pair of stations. The atmospheric waves of tropospheric and stratospheric origin may be responsible for this effect.

Acknowledgement: This paper has been supported by the Grant Agency of the Czech Republic (15-24688S) and Ministry of Education, Youth and Sports (LG13042).

References

Altadill, D., Apostolov, E.M., Boska, J., et al. Lastovicka, J., Sauli, P., 2004. Planetary and gravity wave signatures in the F-region ionosphere with impact on radio propagation predictions and variability. Ann Geophys, 47, 2-3, S, 1109-1119.

Bluestein, H. B., 1993. Synoptic-Dynamic Meteorology in Midlatitudes: Volume II: Observations and Theory of Weather Systems. ISBN-13: 978-0195062687 ISBN-10: 019506268X

Boska, J., Sauli, P., 2001. Observations of gravity waves of meteorological origin in the F-region ionosphere. Phys. Chem. Earth, 26 , 6, 425-428.

Forbes, J.M., Palo, S.E., Zhang, X., 2000. Variability of the ionosphere. JASTP, 62, 685–693.

Forbes, J.M., and Leveroni, S., 1992. Quasi 16-day oscillation in the ionosphere. GRL, 19, 10, 981-984.

Fritts, D. C., and Luo, Z., 1992. Gravity wave excitation by geostrophic adjustment of the jet stream. Part I: Two-dimensional forcing. JAS, 49, 861-697.

Fritts, D.C., and Nastrom, G.D. ,1992. Sources of mesoscale variability of gravity waves, II, Frontal, Convective and Jet stream excitation, JAS, 49, 111-127.

Grinsted, A., Moore, J. C., Jevrejeva, S., 2004. Application of the cross wavelet transform and wavelet coherence to geophysical time series. NPG, 11, 561–566. http://www.glaciology.net/

Hidore, J. J., Oliver, J.E., Snow, M., Snow, R., 2009. Climatology: An Atmospheric Science (3rd Edition), ISBN-13: 978-0321602053 ISBN-10: 0321602056

Kaspar, M., Müller, M., 2010. Variants of synoptic-scale patterns inducing heavy rains in the Czech Republic. Phys. Chem. Earth 35, 477–483.

Lastovicka, J., 2006. Forcing of the ionosphere by waves from below. JASTP, 68, 3–5, 479-497.

Lastovicka, J., and Sauli, P., 1999. Are planetary wave type oscillations in the F2 region caused by planetary wave modulation of upward propagating tides? ASR, 24, I I, 1473-1476.

Luo, Z., and Fritts, D. C., 1992. Gravity wave excitation by geostrophic adjustment of the jet stream. Part II: Three-dimensional forcing. JAS, 50, 1, 104-115.

Mallat, S., 1998. A Wavelet Tour of Signal Processing. Academic Press, San Diego.

Nastrom, G.D., Fritts, D.C., 1992. Sources of mesoscale variability of gravity-waves. 1. Topographic excitation. JAS, 49, 2, 101-110.

Orlanski, I., 1975. A Rational Subdivision of Scales for Atmospheric Processes. BAMS, 56, 5, 527-530.

Pancheva, D., Alberca, L.F. , de la Morena, B.A., 1994. Simultaneous observation of the quasi-two day variations in the lower and upper ionosphere. JASTP, 56, 43–50.

Radicella, S.M., Sauli, P., Jakowski, N., Kouba, D, Portillo, A., Herraiz, M., Strangeways, H.J., Zernov, N., Gherm, V., 2009. Space Plasma Effects. Ann Geophys, 52, 3-4, 359-372.

Roux, S.G., Koucká Knížová, P., Mošna, Z., Abry, P., 2012. Ionosphere fluctuations and global indices: A scale dependent wavelet-based cross-correlation analysis. JASTP, 90-91, 186-197. DOI: 10.1016/j.jastp.2012.03.014

Sauli, P., Boska, J. 2001. Tropospheric events and possible related gravity wave activity effects on the ionosphere. JASTP, 63, 9, 945-950.

Torrence, C. and Compo, G. P., 1998. A practical guide to wavelet analysis, BAMS, 79, 61–78, http://paos.colorado.edu/research/wavelets/

Yiğit, E., and Medvedev, A. S., 2015. Internal wave coupling processes in Earth's atmosphere, ASR, 55, 983–1003, doi:10.1016/j.asr.2014.11.020.

The Atlantic multidecadal oscillation influence on temperatures and on structural changes

R. Werner[1], *D. Valev*[1], *D. Danov*[1], *V. Guineva*[1] *and A. Kirillov*[2]

[1] Space Research and Technology Institute (SRTI), BAS,
Stara Zagora Department, Stara Zagora, Bulgaria
[2] Polar Geophysical Institute (PGI), Apatity, Russia
E-mail: rolwer52@yahoo.co.uk

Abstract.

The cooling and the following warming periods in the Northern Hemisphere are very well captured by the statistic models taking in consideration the Atlantic multidecadal oscillation (AMO). It is found that the AMO temperature influence increases from South to North, which is related to the heat transfer from the tropics to the Northern Atlantic by the thermohaline circulation. It is demonstrated, that structural breaks of the Northern Hemisphere and global temperatures are connected with AMO. The AMO influence removed temperature series show only one significant break. The strong AMO influence on the Northern Hemisphere and global temperatures will reduce the temperature increase in the next decades but when the AMO index will begin rising again the warming rates will achieve values close to the obtained ones during the last decades or greater than them due to higher dioxide content.

1. Introduction

AMO represents changes of the Sea surface temperatures variability in the North Atlantic with periodicities of roughly 70 years (Enfield**,** 2010)**.** AMO shows significant climate impacts, as correlations with rainfalls over continental parts of USA (Enfield, 2001), over Sahel (Folland et al., 1986) and North-East Brasil (Folland et al., 2001). Relations to North American and European climate (Sutton and Hudson, 2005) and connection with river flows (Enfield, 2001) were found. Some studies have proved an AMO contribution to higher frequency of Atlantic hurricanes and their energy (Goldberg et al., 2001, Wang and Dong, 2010). A link with the variability of the termohaline circulation was demonstrated (Delworth and Mann, 2000).

In this paper temperature anomalies of the three most important climate centers: the Goddard Institute for Space Studies (GISS) at NASA, the National Climatic Data Center (NCDC) at NOAA, both of USA, and the Hadley Centre at the Met Office of UK which collaborates with the Climate Research, are analysed.

2. Regression analysis methods

By means of a simple multiple regression of the global and hemisphere combined land/ocean, land and ocean surface temperatures against the carbon dioxide (CO_2) (Hansen et al.,2004), AMO (Enfield et al., 2001), the Pacific decadal oscillation (PDO) (Zhang et al., 1997 and Mantua et al., 1997), the Total Solar Irradiance (TSI) (Wang, Lean and Sheeley, 2005), the Southern oscillation (SO) (Trenberth, 1984), and Atmospheric Optical Depth (AOD) (Sato, 1993) the annual surface temperatures were modeled (without feedbacks). Because of the saturation effect of the absorption by CO_2 a logarithmic relation of CO_2 was used and the mixing ratio was related to the pre-industrial CO_2 level of 280 ppmv. Structure changes in the temperature time series are studied based on piecewise regression model (Seidel and Lazante, 2004). The regression analyses were performed stepwise with backward elimination of the most non-significant term at every step and the model coefficients were tested at a significance level of 0.95, where the autocorrelation of the residuals was taken into account (Werner et al., 2015).

2.1. Combined land-ocean Global and hemispheric temperature analysis

By the regression the CO_2 concentration is obtained as the most significant impact factor on the temperatures, as a whole the regression coefficient is approximately 3.0 and doesn't show hemispheric dependencies.

The increase of CO_2 produced a warming of 0.75ºC during the period 1900-2011 and it is not appreciably influenced by the hemispheric land-ocean distribution differences. In contrast the influence of AMO, which is the second important factor, has significantly greater regression coefficients in the Northern Hemisphere (NH). The mean AMO amplitude in NH is of the order of 0.13ºC for all three used data sets. For the Southern Hemisphere (SH) an mean influence of 0.03ºC is found only for the GISS data. The SO temperature influences do not exceed an absolute value of about 0.1ºC. Weak temperature impacts are obtained for TSI. Significant influences are obtained only for the GISS and NCDC data sets from SH, where the temperature response is smaller than 0.15ºC, and the temperature response from solar maximum to solar minimum is not greater than 0.12ºC. It is very important to stress, that the multiple correlation coefficients obtained here for all models are very high. The lowest values but higher than 0.92 are obtained for the SH models where the AMO influence is low or not significant. However, the explained variance is also higher than 0.85. The best correlation of 0.965 corresponding to 93% explained temperature variance is found for GISS and NCDC global temperature anomalies model. For the HadCrut3 data the corresponding values are 0.954 and 91%, respectively.

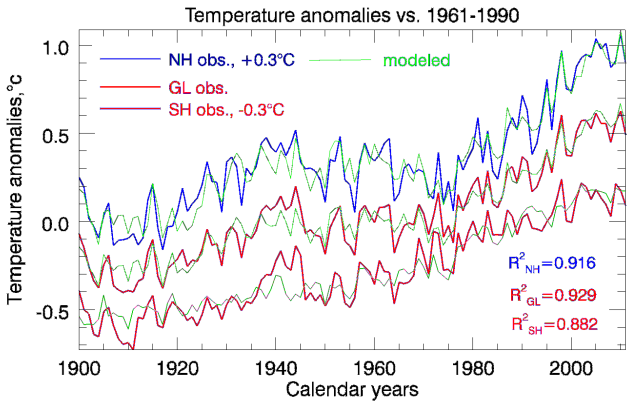

Fig.1. Observed global and hemisphere temperature anomalies by NCDC and the results of the modeled by regression temperature evolutions.

2.2. Analysis of the global temperatures separately over land and ocean

The obtained regression coefficients of the three used data sets do not show significant differences. The obtained CO_2 influences on the temperature anomalies over land are significantly greater, approximately two times, than the ones over the ocean by reason of feedback mechanisms. The increase of CO_2 produced a warming of approximately 0.6ºC and 1.2ºC over the oceans and the land, correspondingly, during the studied time period. For the AMO, SO and AOD influences no land/ocean differences are obvious.

2.3. Temperature forecast

AMO and the logarithmic term of CO_2 in the regression equations are the only long time terms. Our prognosis is based on a growth rate of 1.68 ppmv/year for CO_2, resulting from the linear regression for the last 30 years (1982-2011) and on the description of AMO by harmonic regression of first order with a period of 64 years and an amplitude of 0.208. Inserting the regression coefficients of the full regression model also for the expected values for the CO_2 content and the AMO index the prognosis ensemble mean temperatures are obtained for the forecast period 2012-2100.

Fig.2 presents the forecasts for the temperature evolution over land and ocean separately and for the combined land/ocean temperature obtained on the base of NCDC data set. The temperature over land from 1900 up to the end of our century will change approximately with 2.5°C. In contrast over the sea the temperature change will be only about 1.2°C, if the CO_2 concentration is going to increase with the same rate as it was observed in the last 30 years and if AMO is stable. In the next decades the warming rates will be smaller than the observed ones in the last 30 years due to the AMO influence, which will give us a chance to reduce the CO_2 emission in time.

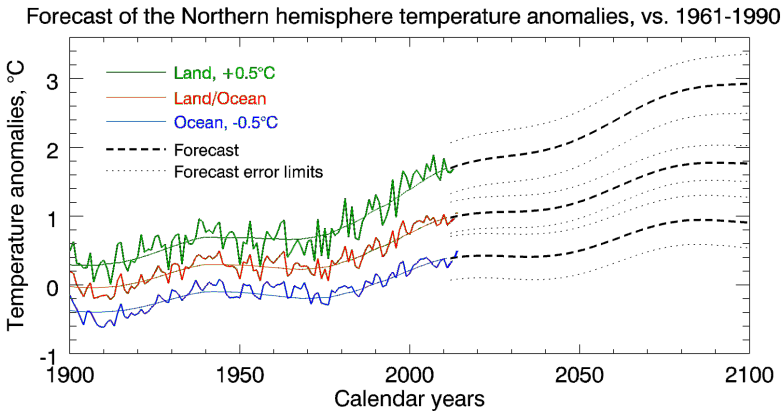

Fig.2. Observed global land, land/ocean and ocean NCDC temperature records and forecasts. The long term approximations are shown by thin continuous lines.

2.4. Temperature structural changes

The study of climate trends especially of the temperature trends taking into consideration possible structural changes is important for understanding the climate development itself and to find the correct answer whether the climate can be characterized by a stochastic trend or by a determined one. Here the global and hemisphere temperature anomalies are modeled by piecewise linear regression (see e.g. Green, 1993) to determine the break points in the temperature evolution, where a multitude of break point (BP) locations are simultaneously analyzed and the significances of slopes are tested. To choose the model the Schwarz-Bayesian Information Criterion (BIC) using the effective sample size (Seidel and Lazante, 2004) and the LWZ criterion (Liu et al., 1997) were used. The model with minimal criterion value was selected as the true model. In Fig.3 the studied here different observed global temperature time series and the resulting piece wise regression models for three BP's, where the LWZ criterion has minimal values are shown. To study the AMO influence on the structure changes from the temperature series the AMO influence was removed by subtracting the AMO temperature impact, obtained in the regression equations. The resulting temperature series were analysed by piecewise linear regression for structural changes. The results are shown in Fig.4.

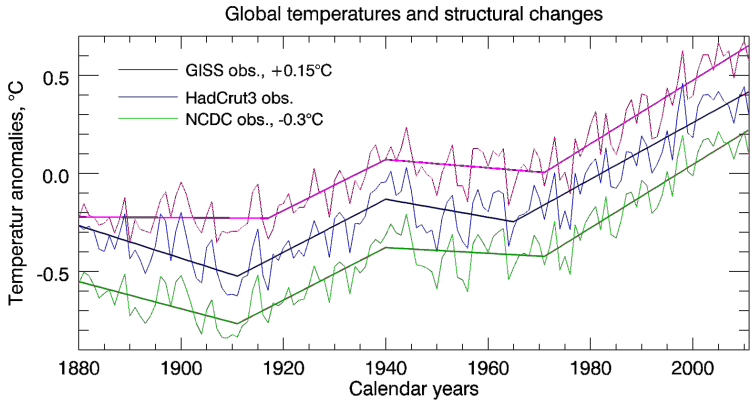

Fig.3. The global temperature anomalies by the three data sets. The thick lines show the structural models chosen by the LWZ criterion.

For the temperature series with removed AMO influences only one structural break point was found in every series. Hence, the break point structure for the original temperature series with three significant BP's is a result of the AMO temperature influence superimposed on the long time temperature evolution caused by CO_2. The single BP's in the AMO influence removed series corresponds to the third BP's found in the original temperature data, and they are shifted to earlier years, around 1960.

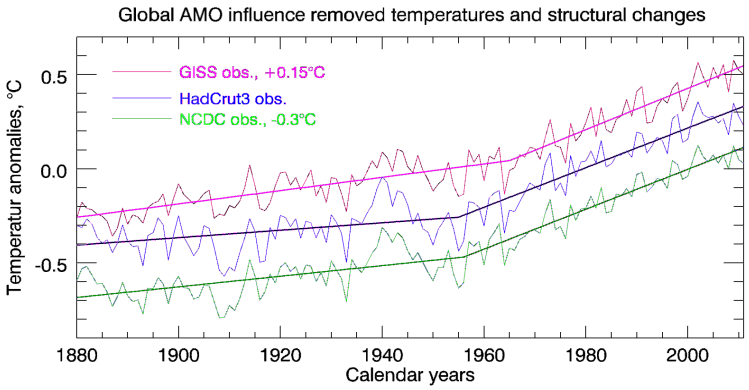

Fig.4. The same as in Fig 3 but for global temperature anomalies, where the AMO temperature influence was removed.

AMO influence on zonal temperatures

It was found that AMO has a strong influence only on the NH temperatures. To study the influences in more detail GISS zonal land temperatures were used, because of greater ocean temperature errors in the past. In Fig.5 the found dependences of the AMO temperature influence are presented. The AMO temperature influence increases from the Southern Subtropics to North. In the Antarctic zone and the Southern subtropic an anti-correlation to the zonal temperature is observed. The mean amplitude of the AMO index, used in the regressions, is about 0.2. The temperature influence of AMO on the Arctic temperature has a mean amplitude of 0.23°C, for example. The Latitude dependence of the AMO temperature influence is in accordance with the heat redistribution from South to North by an Artic Antarctic seesaw (Chylek et al., 2010).

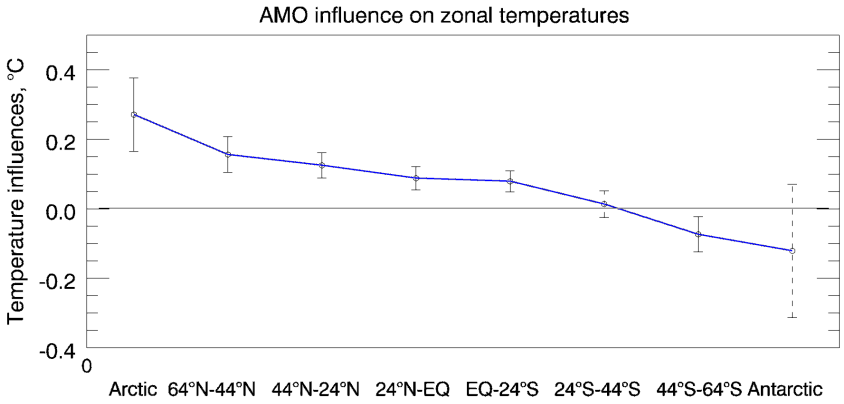

Fig.5. Latitude dependence of the AMO influence on the temperature, shown as dependences of the regression coefficients. For significant influences the error bars are presented by continuous line. In the case of non-significant influence the error bars passes and are drawn by dashed lines.

Conclusions

The found results demonstrated the important AMO influence on the temperature distribution and on the structural changes. The temperature oscillations generated by AMO have to be removed before the estimation of long time temperature trends.

References

The reference list of the cited in the text publications will be given on request.

Kinetics of electronically excited O2 molecules in the mixture of CO_2, CO, N_2, O_2 gases

Kirillov A.S. [1], *Werner R.* [2], *Guineva V.* [2]

[1] Polar Geophysical Institute of RAS, Apatity, Murmansk region, Russia
[2] Space Research and Technology Institute of BAS, Stara Zagora, Bulgaria
E-mail: rolwer52@yahoo.co.uk

Introduction

CO_2, CO, N_2, O_2 gases are the main components in the atmospheres of terrestrial planets. Electronically excited molecules play very important role in chemical kinetics of a mixture of atmospheric gases. It has been proposed by Toumi [1993], Siskind et al. [1993], Prasad [1997] that the interaction of $O_2(b^1\Sigma_g^+)$ with H_2 and N_2O molecules may significantly influence the chemistry of the stratosphere and upper troposphere of the Earth as a source of odd-hydrogen (HO_x) or odd-nitrogen (NO_x).

$O_2(b^1\Sigma_g^+)$ molecules are effectively produced in the atmosphere of the Earth at altitudes between 80 and 110 km. Three-body collisions

$$O + O + M \rightarrow O_2^* + M \qquad (1)$$

are main production mechanism of electronically excited molecular oxygen at the altitudes of the nightglow in the atmosphere of the Earth [Slanger and Copeland, 2003]. Spontaneous radiative transitions from the $b^1\Sigma_g^+$ state to the ground $X^3\Sigma_g^-$ state lead to emissions of Atmospheric bands in the nightglow of the atmosphere.

$$O_2(b^1\Sigma_g^+,v) \rightarrow O_2(X^3\Sigma_g^-,v') + h\nu_{Atm} \ . \qquad (2)$$

A study of excitation, quenching, and energy transfer processes in the oxygen nightglow on Venus and Mars by Krasnopolsky [2011] has considered altitude profiles of $[O_2(b^1\Sigma_g^+)]$ in atmospheres of the planets. The study was based on the observed nightglow intensities and vertical profiles, measured reaction rate coefficients, and photochemical models of the nighttime atmospheres of the Venus and Mars. Krasnopolsky [2011] has analysed mainly the kinetics of $O_2(b^1\Sigma_g^+,v=0)$, but detailed study of $O_2(b^1\Sigma_g^+,v\geq0)$ needs a set of the quenching constants for collisions with molecules of main gases in atmospheres of the planets.

The quenching rate coefficients

We apply the Rosen-Zener approximation to calculate the removal rates of O_2^* in inelastic collisions with CO_2, CO, N_2, O_2 molecules [Kirillov, 2004a,b]. The quenching rates of the $b^1\Sigma_g^+,v$=1-15 state by O_2 molecules are calculated with the consideration of intermolecular (EE-processes) transfers of electronic excitation [Kirillov, 2012]

$$O_2(b^1\Sigma_g^+,v) + O_2(X^3\Sigma_g^-,v=0) \rightarrow O_2(X^3\Sigma_g^-,v') + O_2(a^1\Delta_g,b^1\Sigma_g^+;v'') \ . \qquad (3)$$

Also we consider EV-processes of removal in the collisions with N_2, CO, CO_2, O_2 molecules

$$O_2(b^1\Sigma_g^+,v) + N_2(X^1\Sigma_g^+,v=0) \rightarrow O_2(a^1\Delta_g,v') + N_2(X^1\Sigma_g^+,v=1) \ , \qquad (4)$$

$$O_2(b^1\Sigma_g^+,v) + CO(X^1\Sigma^+,v=0) \rightarrow O_2(a^1\Delta_g,v') + CO(X^1\Sigma^+,v=1), \qquad (5)$$

$$O_2(b^1\Sigma_g^+,v) + CO_2(X^1\Sigma_g^+,0,0,0) \rightarrow O_2(a^1\Delta_g,v') + CO_2(X^1\Sigma_g^+,1,0,1) \ , \qquad (6)$$

$$O_2(b^1\Sigma_g^+,v) + O_2(X^3\Sigma_g^-,v=0) \rightarrow O_2(a^1\Delta_g,v') + O_2(X^3\Sigma_g^-,v=1). \qquad (7)$$

Here there are the transitions of electronically excited O_2^* molecules in another excited state with vibrational excitation of the ground state of target molecules. Moreover, we take into account the processes of VV-processes of energy exchange in the collisions with carbon dioxide molecules

$$O_2(b^1\Sigma_g^+,v) + CO_2(X^1\Sigma_g^+,0,0,0) \rightarrow O_2(b^1\Sigma_g^+,v\text{-}1) + CO_2(X^1\Sigma_g^+,1,0,0) \; . \qquad (8)$$

The process (8) means that the $O_2(b^1\Sigma_g^+,v)$ molecule losses one vibrational quantum of the $b^1\Sigma_g^+$ state and the energy transforms in vibrational quantum of symmetric stretch mode of CO_2 molecule.

The calculated quenching rate coefficients for the $b^1\Sigma_g^+,v$=1-15 state in the collisions (3-8) with O_2, N_2, CO, CO_2 molecules are presented in Fig.1. The calculations have shown that the quenching is very efficient in the collisions with O_2 molecules for high vibrational levels of this singlet state. More effective quenching by carbon dioxide molecules is seen for lower vibrational states of the $b^1\Sigma_g^+$ state.

The calculated quenching rate coefficients of electronically excited O_2 molecules are used in the simulations of vibrational populations of O_2 electronic states in the mixture of gases.

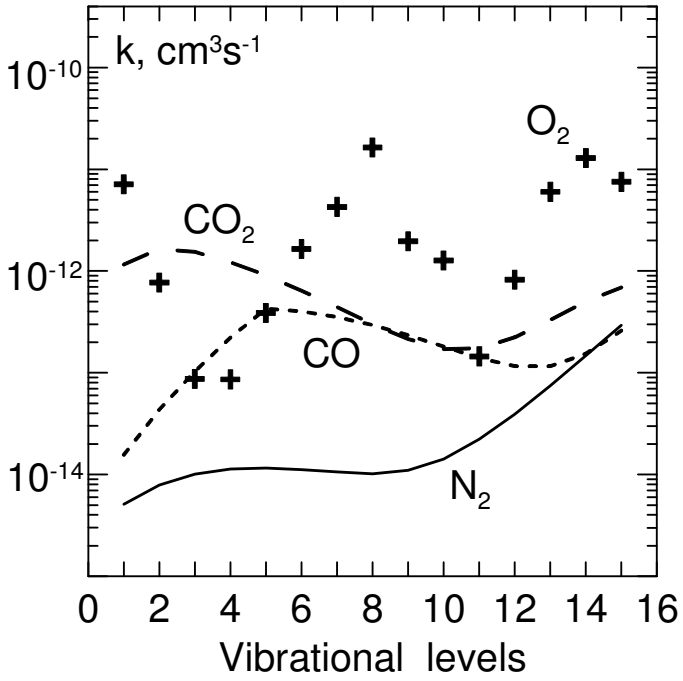

Fig.1. *The calculated quenching rate coefficients for the* $b^1\Sigma_g^+,v$=1-15 *state in the collisions with* O_2, N_2, CO, CO_2 *molecules (crosses; solid, short-dashed, long-dashed lines, respectively).*

Vibrational populations of O2(b1Σg+) in the mixture

It is suggested that three-body collisions (1) are the production mechanism of initially excited O_2. Vibrational populations of singlet oxygen are calculated at mixture pressures of 10^{-1}-10^0 Pa. The removal rates are taken according to the data presented in Fig.1.

The calculated vibrational populations of singlet $b^1\Sigma_g^+,v$=1-15 state of molecular oxygen in the mixture of O_2^* with the gases N_2, CO, CO_2 at pressures of 10^{-1}-10^0 Pa are shown in Fig.2. Also the experimental data of populations estimated from spectrometric observations from Keck-I telescope [Slanger et al., 2000] are presented in Fig.2. Slanger et al. [2000] have observed the intenities of Atmospheric bands (2) emitted from fifteen vibrational levels of the singlet state in the nightglow of the Earth.

It is seen from this figure that the behaviour of the populations in the cases of N_2-O_2 and CO-O_2 mixtures are similar. The principal influence of carbon dioxide molecules is seen in the case of CO_2-O_2 mixture. This mixture is an analogue of Venus and Mars atmosphere at the altitudes of the nightglow. It is seen from Fig.2 that there is an increase of relative populations of highest vibrational levels in comparison with ones of lowest levels. The difference in the behaviour of the populations for the mixtures can be explained by the removal rates presented in Fig.1.

The results of the calculations can be applied in the study of electronic kinetics of O_2^* at the altitudes of nightglows in the atmospheres of terrestrial planets and in active mediums of laboratory discharges and lasers.

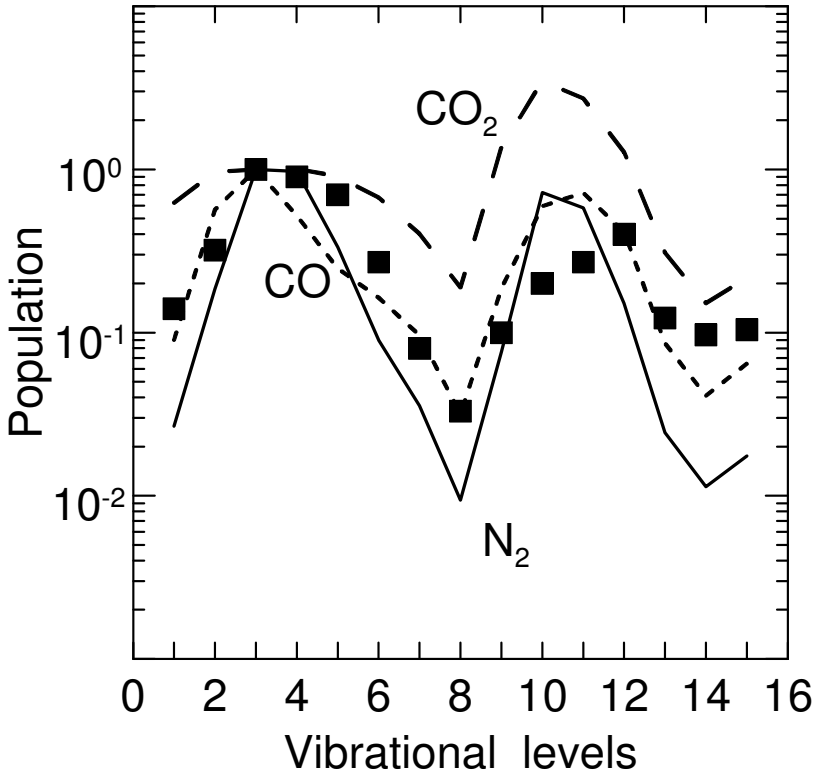

Fig.2. The calculated vibrational populations of singlet $b^1\Sigma_g^+$,v=1-15 state of molecular oxygen in the mixture of O_2^* with the gases N_2 (solid line), CO (short-dashed line), CO_2 (long-dashed line); experimental data by Slanger et al . [2000] – squares.

Conclusions

The main results of this presentation are as follows.

1. Applying the Rosen-Zener approximation we have calculated the removal rates of $O_2(b^1\Sigma_g^+,v)$ in inelastic collisions with CO_2, CO, N_2, O_2 molecules. The calculation has taken into account EE (3), EV (4-7) and VV (8) electron energy transfer processes.

2. Using the calculated removal rate constants we have simulated vibrational populations of singlet $b^1\Sigma_g^+$,v=1-15 state of molecular oxygen in the mixture of O_2^* with the gases N_2, CO, CO_2 at pressures of 10^{-1}-10^0 Pa. The results of the calculation show the principal dependence of the populations on the kind of admixture gas. The dependence can be explained by peculiarities of removal rates of $O_2(b^1\Sigma_g^+)$ in inelastic collisions with another molecules.

References

Kirillov A.S. Application of Landau-Zener and Rosen-Zener approximations to calculate rates of electron energy transfer processes. // Adv. Space Res., 2004a, v.33, p.993–997.

Kirillov A.S. Calculation of rate coefficients of electron energy transfer processes for molecular nitrogen and molecular oxygen. // Adv. Space Res., 2004b, v.33, p.998–1004.

Kirillov A.S. Calculation of rate coefficients for the interaction of singlet and triplet vibrationally excited oxygen. // Quantum Electronics, 2012, v.42, p.653-658.

Krasnopolsky V.A. Excitation of the oxygen nightglow on the terrestrial planets. // Planet. Space Sci., 2011, v.59, p.754-766.

Prasad S.S. Potential atmospheric sources and sinks of nitrous oxide. 2. Possibilities from excited O_2, "embryonic" O_3, and optically pumped excited O_3. // J. Geophys. Res., 1997, v.102, p.21527-21536.

Siskind D.E., Summers M.E., Mlynczak M.G. An evaluation of $O_2(b^1\Sigma_g)$ as a possible source of OH and odd-nitrogen in the stratosphere and mesosphere. // Geophys. Res. Lett., 1993, v.20, p.2047-2050.

Slanger T.G. and Copeland R.A. Energetic oxygen in the upper atmosphere and the laboratory. // Chem. Rev., 2003, v.103, p.4731-4766.

Slanger T.G., Cosby P.C., Huestis D.L., Osterbrock D.E. Vibrational level distribution of $O_2(b^1\Sigma_g^+,v=0\text{-}15)$ in the mesosphere and lower thermosphere region. // J. Geophys. Res., 2000, v.105, p.20557-20564.

Toumi R. A potential new source of OH and odd-nitrogen in the atmosphere. // Geophys. Res. Lett., 1993, v.20, p.25-28.

Geomagnetic activity influence on the season variations of myocardial infarction in subauroral (Yakutia) and low latitudes (Bulgaria)

S.N. Samsonov[1], *N.G. Kleimenova*[2,3], *P.G. Petrova*[4]
[1]*Shafer Institute of Cosmophysical Research and Aeronomy, Siberian Branch, Russian Academy of Sciences, Yakutsk, Russia*
[2]*Schmidt Institute of Physics of the Earth, Russian Academy of Sciences, Moscow, Russia*
[3]*Space Research Institute, Russian Academy of Sciences, Moscow, Russia*
[4]*Medical Institute at Ammosov North_Eastern Federal University, Yakutsk, Russia*

Abstract

The problem of possible influence of the solar and geomagnetic activity on the human health has been discussed during the last decades. It was established that the heart and cardiovascular system could be the main targets of this negative action. Here we present the results of the comparison of the seasonal variations of the emergency medical calls for myocardial infarction in Yakutsk (subauroral geomagnetic latitudes) with planetary geomagnetic activity near maximum (1992) and minimum (1998) solar activity and found their good agreement. However, the seasonal behaviour of deaths from myocardial infarctions at low latitudes (Bulgaria) exhibited significant differences. In Bulgaria, the maximum of infarctions was in winter without a strong correlation with magnetic activity, but controlled by Pc1 geomagnetic pulsations at periods of about 0.5–2.0 Hz. In Yakutsk, there are several maxima coincided with increase of geomagnetic activity. We suppose that, in subauroral latitudes, unlike low latitudes, a major role in the increase in the number of infarctions is played those magnetic storms which demonstrate strongest disturbances (substorms) in local (i.e. in Yakutsk) night. Typically, substorms are accompanied by irregular 0.3-4.0 Hz geomagnetic Pi1 pulsations quickly decreasing with latitude and therefore seldom observing at low latitudes. We suppose that Pi1 at subauroral latitudes like Pc1at low ones could be biotropic.

Introduction

A huge number of publications describing the influence of the solar and geomagnetic activity on the human health have appeared over last decades. Very many authors have accepted geomagnetic storms and solar flares as an important factor of hazard. It was found (e.g., Breus et al., 1995; Baevsky et al., 1997) that the main targets of the solar and geomagnetic activity influence are the heart and the cardio-vascular system.

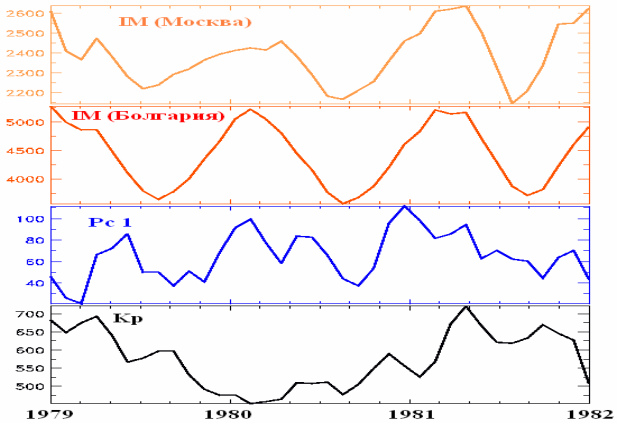

Fig.1. Infarctions (Moscow), mortality (Bulgaria), Pc1 pulsations and geomagnetic activity/

Some authors (e.g., Kleimenova and Troitskaya, 1992; Kleimenova et al., 2007) supported that geomagnetic pulsations could be one of central biotropic "agents" of magnetic storms. It was found (Kleimenova et al., 2007) the seasonal variations of the Moscow ambulance call numbers, related to diseases of the cardio-vascular system are characterized by the same seasonal regularity as it was shown by Ivanova et al. (2002) for the infarction mortality in Bulgaria. Namely, it was the profound summer minimum and the winter time maximum (Fig. 1). Very good correlation between Moscow and Bulgaria data is seen. However, they demonstrate very poor correlation with planetary geomagnetic activity.

Results of analyzing medical data

We studied the number of calls for the emergency medical care (EMC) related to myocardial infarctions in Yakutsk (subauroral geomagnetic latitudes) near the maximum (1992) and minimum (1998) of solar activity (Fig.2) and found their good correlation. The number of EMC was higher near the solar maximum than near the solar minimum.

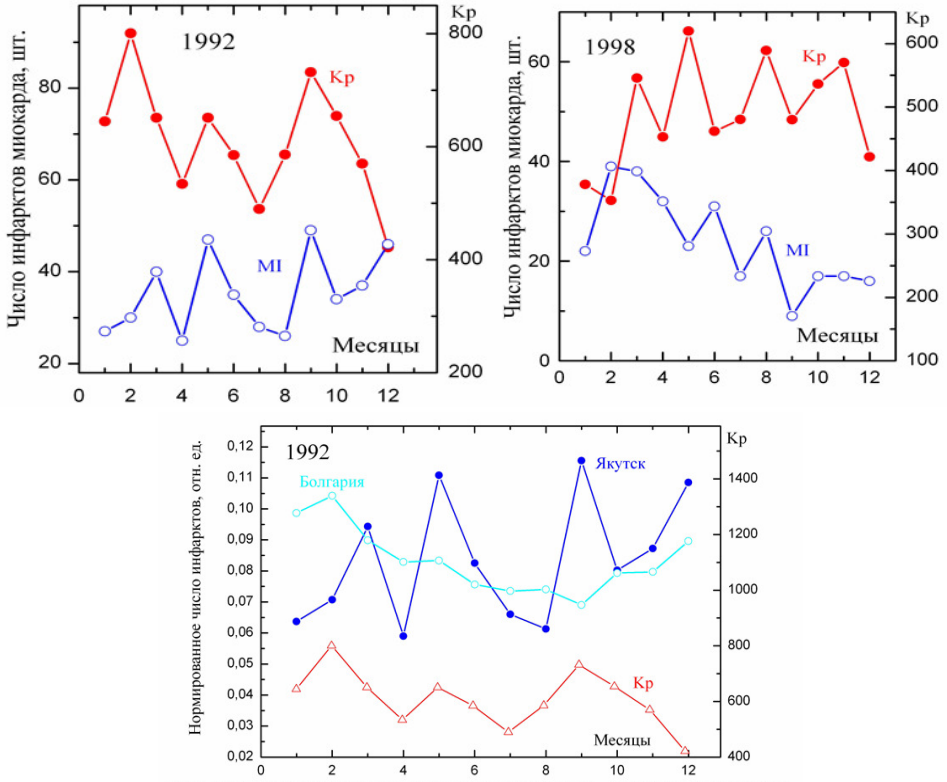

Рис.2. Сопоставление одновременных медицинских данных - общей смертности от ИМ в Болгарии в 1992 г., числа вызовов СМП в г.Якутске по поводу ИМ и Кр-индекса

Fig. 2. The season distribution of the EMC number in Yakutsk (1992 and 1998) and their comparison with infarction mortality in Bulgaria (bottom plot).

It is seen that subauroral (Yakutsk) and low-latitude data does not correlate. In Bulgaria, the maximum of myocardial infarction was registered in winter and the minimum in summer, however, in Yakutsk there are several maxima coinciding with sharp and significant increases of planetary geomagnetic disturbances.

It is known, that with increasing planetary magnetic activity, the substorm development shifts from auroral to subauroral latitudes (so to Yakutsk latitude as well). The substorms could be important factors to medical study because they are typically accompanied by intensive Pi1 geomagnetic pulsations at the similar to Pi1 periods which could be biotropic (e.g. Kleimenova et al., 2007). A typical substorm and simultaneous subauroral Pi1 pulsations are shown in Fig. 3.

Discussion

We suggest that summer minimum of the cardio-vascular system disease could be due to availability of some physiological factors making human organisms stronger in summer than in winter. One possible reason of the infarction seasonal effects could be the seasonal variations of the pineal gland hormone (melatonin) production. The melatonin is well known as a multifunctional key regulator of the circadian rhythms.

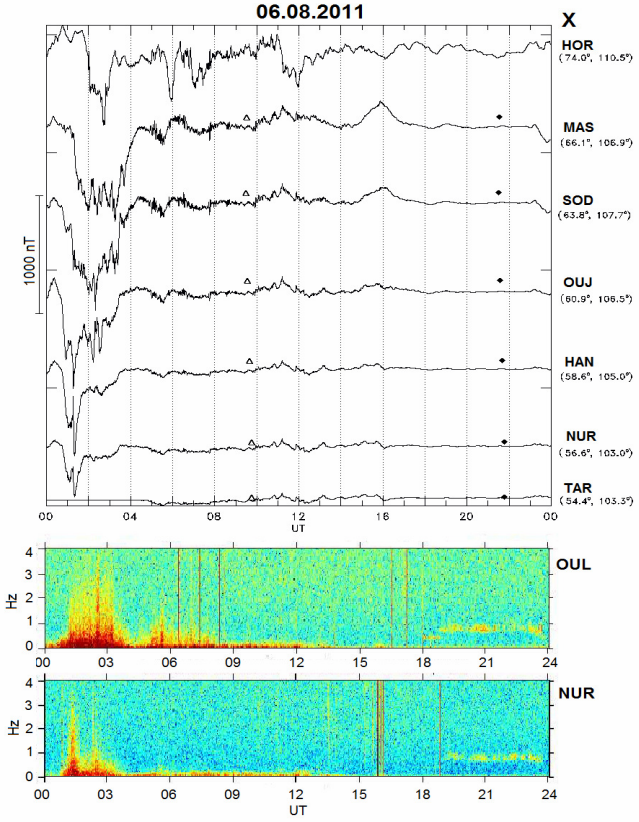

Fig.3. Magnetospheric sudstorm at different stations of IMAGE meridian chain and Pi1 irregular geomagnetic pulsations; the station geomagnetic coordinates are shown in the right.

A seasonal desynchronization of the circadian rhythms connected with the variation of the melatonin production due to long darkness periods in the winter leads to an instability of biological systems and an increase of their sensitivity to effects of other external factors. The melatonin suppressing of both day and night productions was observed during geomagnetic storms (Rapoport et al, 1995). It means, not only the solar luminosity can change the melatonin production, it has to be some other factor (or factors) related to magnetic storm.

One of such negative important factor could be the Pc1 and Pi1 geomagnetic pulsations at frequencies comparable with the human heart beat. Due to that, these pulsations can affect a human cardiovascular system.

Really, it was shown (e.g. Savitz et al., 1999) that low frequency electromagnetic pulses or oscillations can be responsible for biotropic effects. It has been shown that heart cells can became spontaneously synchronized or suddenly suppress their rhythmic oscillations under an influence of some very weak disturbances, for instance, electric impulses at the narrow range of the periods (0.18 - 0.21 s). The phase singularity in the heart rhythm following such impulse action can lead to the heart fibrillation, resulting in sudden death from arhythmia and myocardial infarction.

Summary

A comparison of seasonal distribution of the EMC related to infarction at subauroral latitudes (Yakutsk) with a simultaneous seasonal change of infarction deaths at low latitudes (Bulgaria) showed their significant difference. In Bulgaria, the maximum of myocardial infarction was registered in winter, however, in Yakutsk there are several maxima coinciding with significant increases of planetary geomagnetic activity. We assume that at subauroral latitudes, unlike low latitudes, a great role in aggravations of infarctions plays the enhancement of local geomagnetic activity, namely, the night magnetospheric substorms associated with strong magnetic planetary activity, because substorms are always accompanied by irregular geomagnetic Pi1 pulsations with similar to biotropic Pc1 periods (0.5–5.0) Hz. The Pi1 pulsations can be biotropic, as well as quasi-sinusoidal geomagnetic Pc1 pulsations.

Thus, in subauroral latitudes, could be biotropic both types of geomagnetic pulsations (Fig.4): the night and early morning irregular Pi1 pulsations during the disturbed periods (Kp=2-3) and Pc1 pulsations during the quiet periods after geomagnetic disturbances.

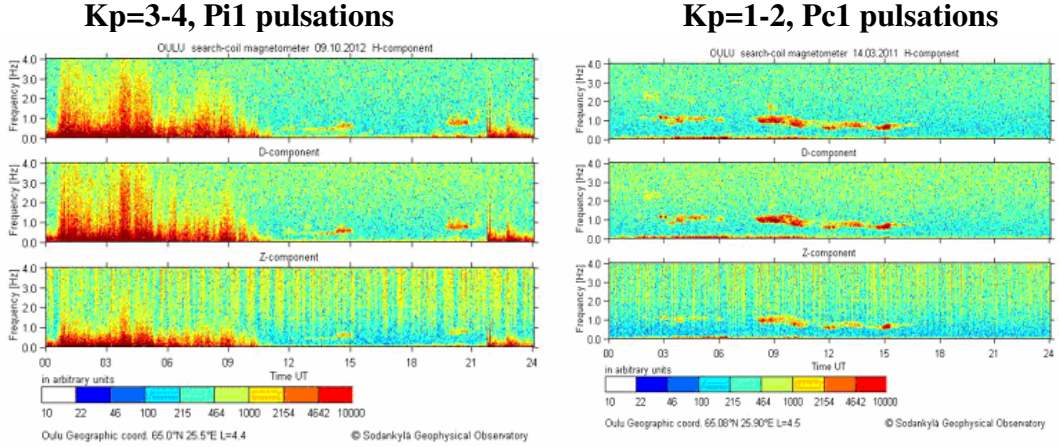

Fig. 4. Spectrograms of Pi1 and Pc1 geomagbnetic pulsations.

References

Breus, T., Cornelissen, G., Halberg, F., and Levitin, A.E., Temporal associations of life with solar and geophysical activity, Annales Geophysicae 13, 1211–1222, 1995.

Baevsky, R.M., Petrov, V.M., Cornélissen, G., Halberg, F., Orth-Gomer, K., Åkerstedt, T., Otsuka, K., Breus, T., Siegelova, J., Dusek, and J., Fiser, B., Meta-analyzed heart rate variability, exposure to geomagnetic storms, and the risk of ischemic heart disease, Scripta medica 70, 199-204, 1997.

Kleimenova, N.G., and Troitskaya, V.A.,. Geomagnetic pulsations as one of the ecological factors of the environment, Biophysics 37(3), 429-338, 1992.

Kleimenova, N.G., Kozyreva, O.V., Breus, T.K., and Rapoport S.I., Pc1 geomagnetic pulsations as a potential hazard of the myocardial infarction, J. Atmos. Space. Terr. Phys. 69 (14), 1759-1764. 2007.

Ivanova, P., Kleimenova, N.G., and Gamburtsev, A.G., Myocardial infarction mortality in Bulgaria, Atlas of the time variations in natural, anthropogenic, and social processes. Moscow, Yanus-K, 3, 561-563, 2002.

Savitz, D.A., Liao, D.P., Sastre, A., Kleichner, R.C., and Kavet, R., Magnetic field exposure and cardiovascular disease mortality among electric utility workers. American Journal of Epidemiology 149, 135–142, 1999.

Rapoport, S.I., Bolshakova, T.D., Malinovskaya, N.K., and Breus, T.K., Magnetic storms as a stress-factor. Biophysics 43(4), 632-639, 1995.

The relative role of space weather factors in Chizhevsky-Velkhover effect

Gromozova E.[1], *Rudenchik E.*[2], *Ragulskaya M.* [2], *Obridko V.* [2], *Hramova E.*[2]

[1] Institute of Microbiology and Virology of the NASU, Ukraina; [2] IZMIRAN, Russia
E-mail: ra_mary@mail.ru

INTRODUCTION.

The Astrobiological Chizhevsky–Velkhover effect occupies a special place among biological effects, concerned with solar activity. It's about the color change of structure elements (volyutin granules) of bacterium sells at staining by methylene blue solution (metachromasia reaction). Today the volyutin granules, consisting of inorganic polyphosphate, were observed at procaryotes, lower eukaryotes, at protozoa, and as phosphatic pellets in platelets of higher organisms (including human).

According to the discoverers, volyutin granules color change depends on solar activity. But since 1934 new data about structure of solar-earth relations were observed, and the solar dynamics changed. Cosmic weather factors having the dominating influence on etalon sell structures in 2000 – 2013 are discussed in the report.

MATERIALS and METHODS

Daily monitoring of staining of volyutin pellets of yeast Saccharomyces cerevisiae and Rhodococcus erytrhopolis from Ukrainian Microorganism Collection D.K. Zabolotny Institute of Microbiology and Virology of the NASU by methylene blue was carried out in 2000 – 2013. (E.Gromozova at all). Yeasts were cultivated on a solid medium (wort-agar) in glass tubes with cotton-gauze in a thermostat at 28oC during 24 h. Every day during the passages of cells onto fresh medium, a part of cells was resuspended in a drop of distilled water directly on the microscopy glass slide surface to form a monolayer. After drying in open air at room temperature, cells were fixed over the lab burner flame and stained with methylene blue by Leffler.Levels of metachromasia were marked: MTC=1, if no metachromatic reaction was observed (volutin granules stained in the blue color); MTC=2, if in the color of the volutin granules saturated violet color was predominant; and MTC=3, if the color of the volutin granules was red. Visual analysis was confirmed by microscopy observation using bright-field method and lens×100/1.30. Digital images of observed cells were captured with Carl Zeiss Primo Star microscope equipment with a digital camera Canon PowerSho A460 and Zeiss AxioVision image analysis microscope software [E. Gromozova,1]. Statistical treatment of the monitoring data was carried out by Solar-Terrestrial Physics department of Pushkov Institute of Terrestrial Magnetism, Ionosphere and Radio Wave Propagation, RAS.

RESULTS and DISCUSSION

Metachromasia dynamics of volyutin pellets of yeast ***Saccharomyces cerevisiae*** sells in 2002-2012 is on fig.1. From the end of 2004 to the middle 2006 the average quantity of events MTC=3 in 2 months is "0,1" instead of "5" in 2000-2003 and "21" in 2007-2012.

Anomalous dynamics of different biological systems was discussed in [2]. We suppose, that the observed charge of dynamics of different levels of organization biological objects corresponds to the adaptative response of biosphere on nonstandard geophysical singularities of 23-24 cycles of solar activity. Probably the observed process is a return of the biosphere reconstruction in anticipation of long solar activity decrease up to 4-5 next cycles[V. Obridko,2; V. Ishkov, 3].

Cosmic weather factors, able to impact considerably on the etalon sell structures, can be classified in 3 groups: terrestrial, solar, galactic. From the first group we take the ap–index of geomagnetical field variations; from the second one – solar radio waves F10,7 intensity; from

the third one – galaxy cosmic rays variations. We build the statistical distributions for chosen factors in random days and in the days with the relevant type of metachromasia.

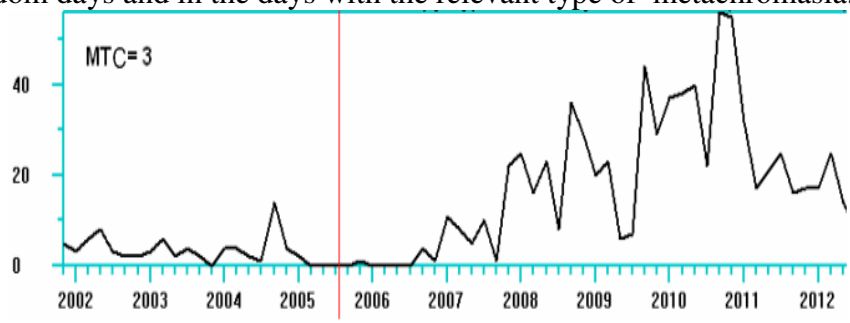

Fig.1. Average quantity of events MTC=3 in 2 months

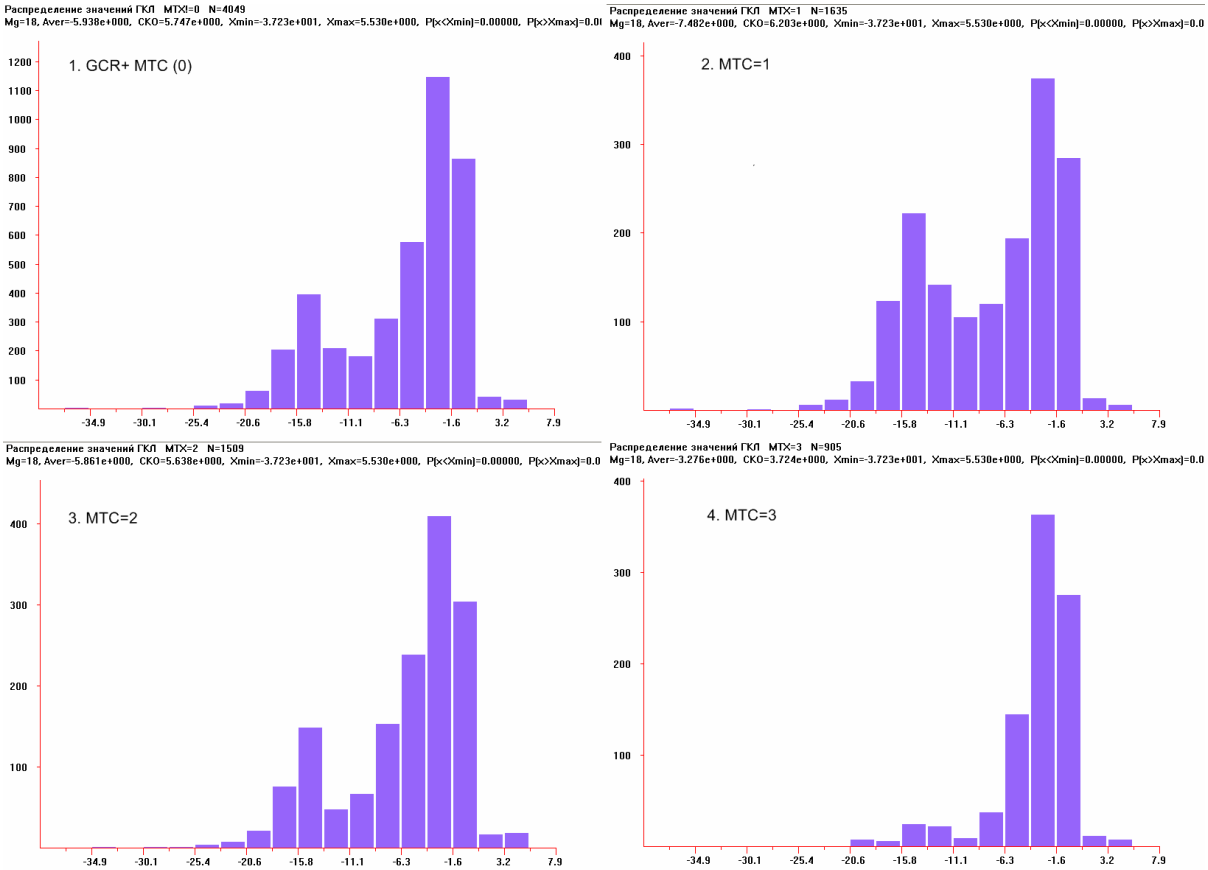

Fig. 2: Bar chart of distribution of galaxy cosmic rays intensity. 1) At Y-axis – quantity of days in the set interval of galaxy cosmic rays intensity. 2,3,4) At Y-axis - quantity of days in the set interval of galaxy cosmic rays intensity, when the metachromasia reaction of 1,2 and 3 types was accordingly observed.

RESULTS of the ANALYSIS:

1. Total statistical distribution for ap–index and MTC= (1,2,3) is random within measurement error.
2. Total statistical distribution for solar radio waves F10,7 intensity is random with MTC (1,2). Weak dependence is observed for solar radio waves F10,7 intensity with MTC= 3.
3. Distributions of galaxy cosmic rays variations in all days in 2000 – 2013 and in days, when MTC $\neq 0$ are equal within measurement error.
4. Distribution of galaxy cosmic rays variations in days with MTC =(1,2) is quite equal to the total distribution. The picture appears if one builds the distribution with random

sample of days, so the MTC= (1,2) can be considered independent from galaxy cosmic rays variations.

5. Distribution of the MTC =3 considerably depends of galaxy cosmic rays intensity variations (fig.2); it means that galaxy cosmic rays intensity variations are the main biotropical agent of the cosmic weather for sell structures.

This conclusion is confirmed by the results of E. Gromozova experiments (2010) on the shielding of the bio-objects. The metachromasy reaction of volutine granules of yeast ***Saccharomyces cerevisiae*** under shielding with the aid of different materials was studied. High likeness in a dynamics of MTC reaction with the control (non-shielded) amples was registered at cells under the permalloy, lead of a 0.1 cm thick with a permalloy layer, and steal. The likeness is much weaker at the cells shielded by the lead of a 0.55 cm thick and by the paraffin, and is about zero for the samples shielded by the water. Dynamics of MTC reaction keeps a high correlation with the control exactly for such types of screens that attenuate essential parts of electric and magnetic natural fields. It allows to presume that natural electromagnetic fields has no a major importance in the influence on the MTC reaction [3].

CONCLUSIONS

Galaxy cosmic rays intensity variations insert the main contribution on the sell structures in Chizhevsky–Velkhover effect, substantially – for MTC=3. The solar factors insert less contribution. The contribution of geomagnetic fields is indistinguishable from random.

Literature

[1] Gromozova E., Voychuk S.I., Vishnevsky V., RagulskayaM., Grigor'ev P. Cosmic rays as bio-regulator of deep time terrestrial ecosystems // Sun and Geosphere. – 2012. – 7(2). – P:117-120.

[2] Obridko V., Ragulskaya M., Rudenchik E., Khabarova O., Hramova E., Solar activity 23-24 cycles and structure of biomedical monitoring data, Tekhnologii zhivykh sistem (Technologies of live systems, ISSN 2070-0997), 2014, 11(3), 12-22, DOI: 10.13140/2.1.2980.4167

[3] Ye.N. Gromozova, N.I. Bogatina, N.V. Bryuzginova, T.L. Kachu, S.I. Voychuk, N.V. Sheykina,P.Ye. Grigoryev . Intensity of metachromatic reaction in volutine granules in ***Saccharomyces cerevisiae*** under the shielding by different materials. // Питання біоіндикації та екології. –Запоріжжя: ЗНУ, 2010. – Вип. 15, № 2. – С. 232–244.

Development of the GPS TEC fluctuations at the high latitude ionosphere during geomagnetic storm

Shagimuratov I.[1], *Chernouss S.*[2], *Efishov I.*[1], *Cherniak I.*[1], *Zakharenkova I.*[1],*Tepenitsyna N.*[1].

[1] WD IZMIRAN, Kaliningrad, Russia;
[2] Polar Geophysical Institute, Appatity, Russia.
E-mail: shagimuratov@mail.ru

Abstract

We report the result of investigations of GNSS signal phase fluctuations occurrence during the geomagnetic storm on October 2, 2013. During this space weather event the intense phase fluctuations have been registered by the permanent GNSS stations not only in the auroral and subauroral regions but even at the midlatitude stations. In combination with the optical and geomagnetic measurements this fact confirms the equaward expansion of the auroral oval.

Index Terms—ionosphere, GNSS, fluctuations.

Introduction

A trans-ionospheric radio wave propagating through the electron density irregularities may experience phase and amplitude fluctuations. Such fluctuations occur due to irregularities with different scales that present in the polar ionosphere. The ionospheric irregularities can be structured with latitude and their intensity vary at the subauroral, auroral, polar and cusp regions. In accordance with this, the fluctuation activity varies considerably with latitude and space weather's conditions. Strong TEC fluctuations can complicate phase ambiguity resolution and to increase the number of undetected and uncorrected cycle slips and loss of signal lock in GPS navigation and positioning errors [1, 2].

The low frequency GPS phase fluctuations occur due to electron density changes along the radio wave path, or the total electron content (TEC) changes. The information about TEC fluctuations may be obtained using the regular GPS observations provided by the International GPS Service (IGS). The worldwide dense network of the GPS stations is very useful for permanent monitoring of the spatial distribution of the ionospheric irregularities on a global scale [3, 4].

In this report GPS measurements of global IGS network were used to study the storm time occurrence of phase fluctuations (TEC changes) in the high latitude ionosphere during October 2, 2013 storm.

Data and geomagnetic conditions

The TEC measurements for individual satellite passes served as raw data. As a measure of fluctuations activity the rate of TEC (ROT, in the unit of TECU/min, 1 TECU=1016 electron/m2) at 1 min interval was used (5). As measure intensity fluctuations index ROTI was used (6).

$$ROTI = \sqrt{\langle ROT^2 \rangle - \langle ROT \rangle^2}$$

During the main phase of the storm we used magnetometer measurments provided by the chain of the Scandinavian network

The storm was rather moderate with the main phase started on October 2,2013 after midnight. Figure 1presents the geomagnetic conditions for September 30 - October 4, 2013.

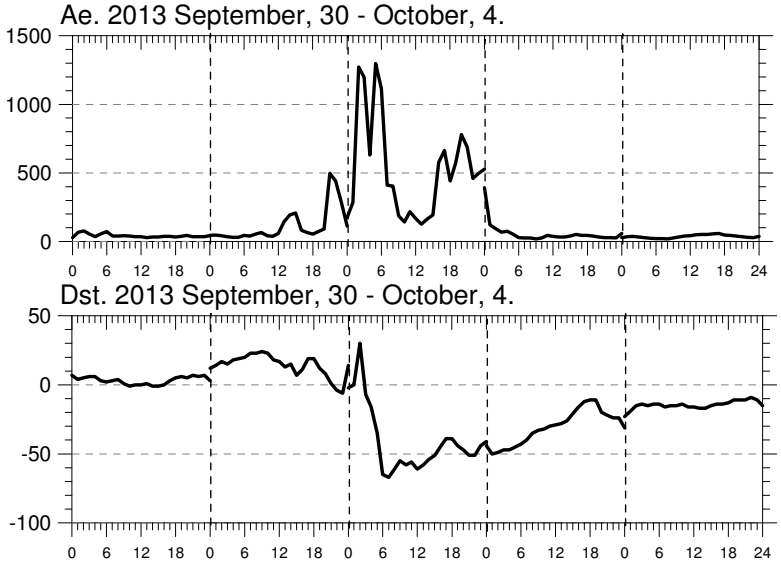

Fig1. Ae and Dst variations for September 30 - October 4, 2013.

Results

Occurrence of the TEC fluctuations can be clearly observed in the temporal variations of the dual frequency carrier phase along satellite passes. For example, the TEC variations, observed at auroral KIRO and midllatitude Kaliningrad stations for quiet and disturbed conditions are presented at Figure 2. The figure demonstrates the rates of TEC changes (ROT) along all satellite passes over 24 hour interval. At Kaliningrad stations for quiet day the fluctuations activity was very low. During geomagnetic disturbed day the intensity of fluctuations was detected in the satellite pass of PRN 14 around 05 UT.

Detailled picture of the fluctuations for PRN 14 at Kaliningrad stations for quiet and disturbed days is presented in Figure 3. The satellite trajectory in the ionosphere (cross line) is also shown on the picture.

The intensive TEC fluctuations during storm day were localized at latitudes 57-58°N when magnetic bays were occurred on magnetogram of the Scandinavian network in time interval 05-06 UT (Fig.4.).

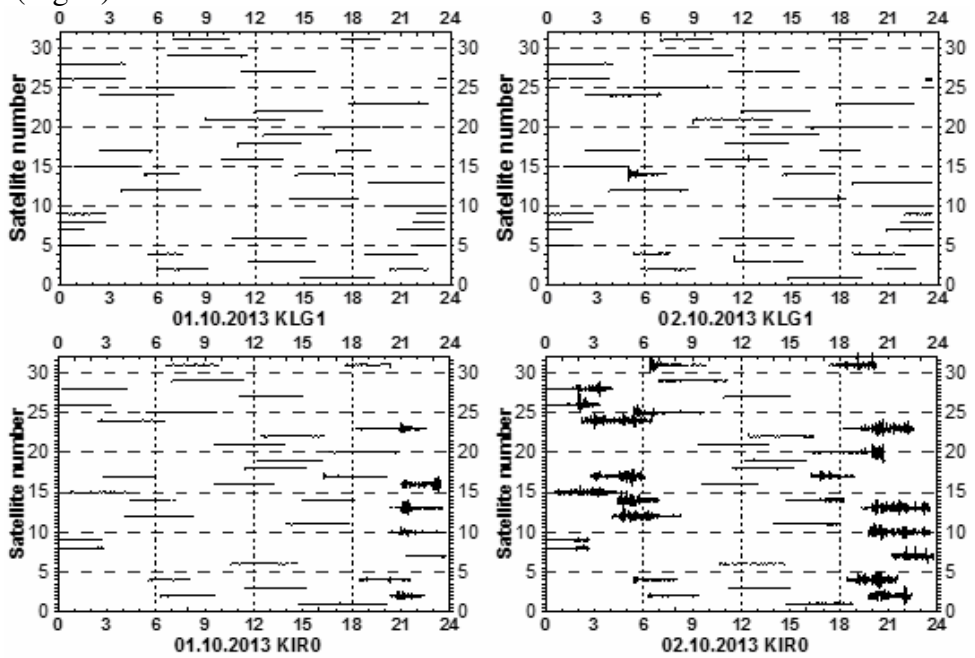

Fig.2.Development of TEC fluctuations at midlatitude Kaliningrad and Kiruna stations for quiet (1 October) and disturbed (2 October) days.

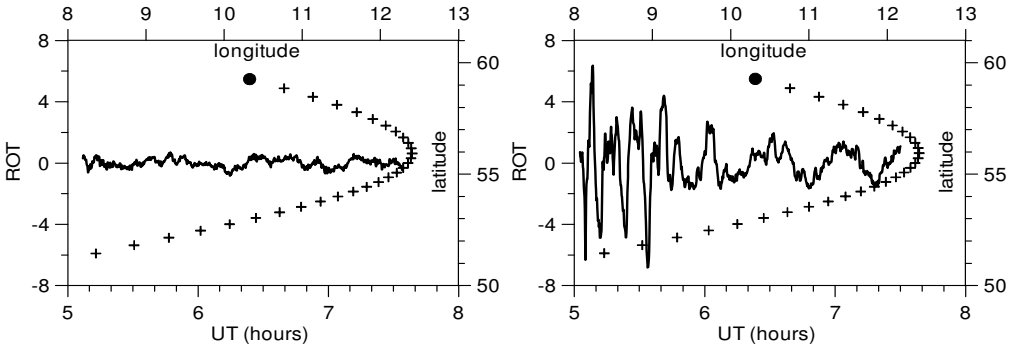

Fig. 3. TEC fluctuations along satellite pass of PRN14 at Kaliningrad station for quiet and disturbed days.

Fure 5. shows the ROT variations at different latitudes and keogram at the stations Lovozero and Sodaynkyul. Obviously, the time course of ROT coincide with the geomagnetic field at the Lovozero and Sodaynkyula stations, as well as with the variations of the geomagnetic field X-component at different stations of Scandinavian network.

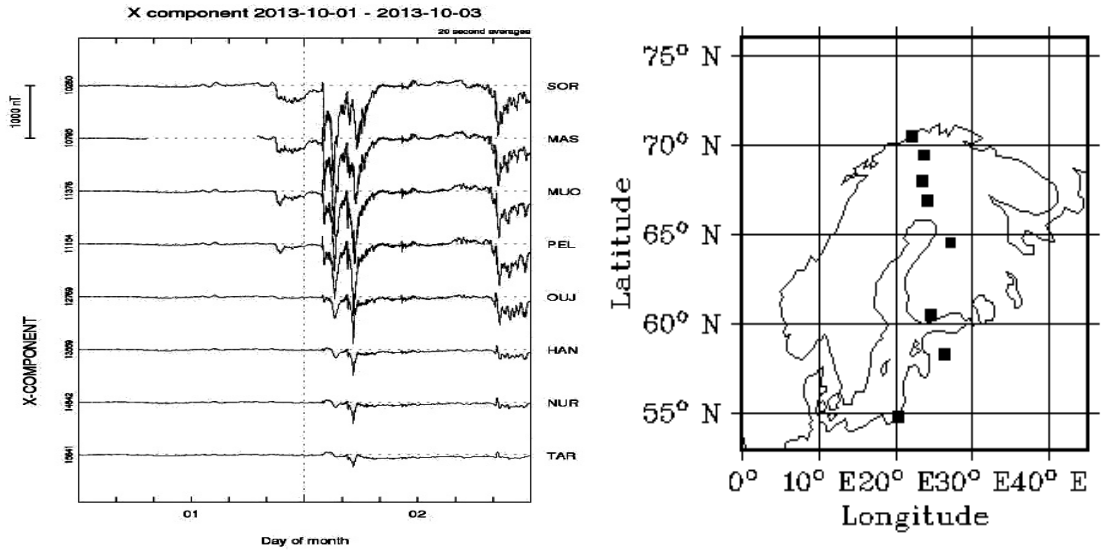

Fig.4. The variations of the geomagnetic field X-component at different stations (left panel) and map of Scandinavian network (right panel).

It appears that according to evidance of the maximum TEC variations as well as the pulsations of the geomagnetic field we can determine the source which affect a destruction of the navigation signal in the ionosphere in the presence of auroral disturbances. This is particularly noticeable in the intervals of the substorm intensification.

For example, a small perturbation around 01.10.2013 21:00 UT, localized in the polar region, had little effect on variations of ROT in Kaliningrad. On the other hand, the strong disturbance about 02/10/2013 05:00 UT as reflected in magnetic observations at the latitude of Kaliningrad and in the values of ROT on this point. This result suggests the possibility of a diagnostics and prognosis the conditions of the navigation signals receiving using measurements of geomagnetic field variations.

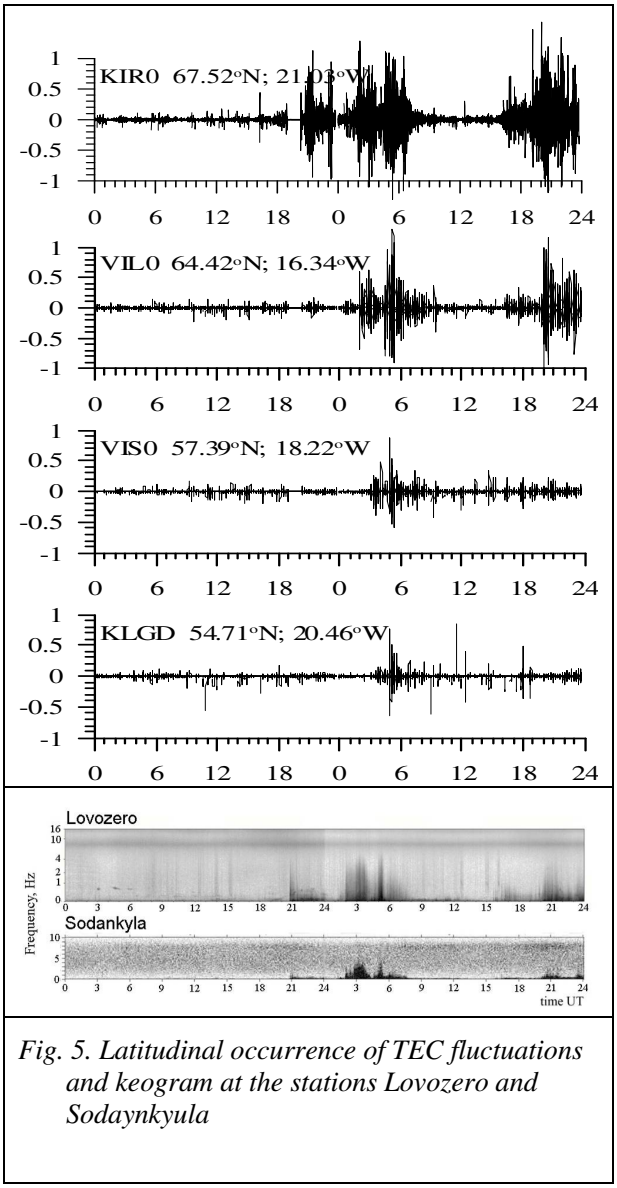

Fig. 5. Latitudinal occurrence of TEC fluctuations and keogram at the stations Lovozero and Sodaynkyula

Irregularity oval

Based on the daily GPS measurements from 130-150 selected stations, the images of spatial distribution TEC fluctuations (index ROTI) in CGC and MLT coordinates was formed. Similarly to the auroral oval, these images demonstrate the irregularity oval. The occurrence of the irregularity oval relates with the auroral oval, cusp and polar cap. The irregularity oval expands equatorward with increase of the magnetic activity.

As an example, Figure 6, presents the dynamics of the irregularity oval in dependece on geomagnetic activity. As seen at Figure 6, the activity and intensity of the TEC fluctuations relate weakly with the behouver of Kp and mostly depend on the auroral activity.

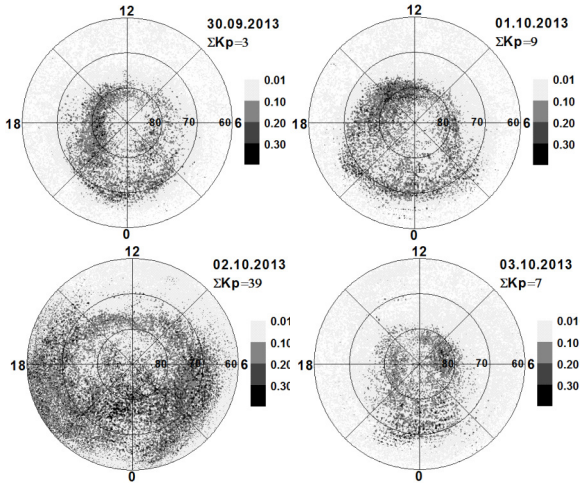

Fig. 6. Dynamics of the irregularity oval.

Conclusions

During October 2, 2013 geomagnetic storm the intense TEC fluctuations were observed at the auroral and subauroral ionosphere. Joint analysis of observed phase fluctuations of GPS signals, and fluctuations of the geomagnetic field demonstrated rather good agreement during intensification of the auroral activity. During the peaks of the aurora activity the intense GPS phase fluctuations were registered even at midlatitude station Kaliningrad. In combination with optical and geomagnetical measurements this fact confirms the equatorward expansion of the auroral oval. The analysis is shown that the irregularity oval is very sensitive to variations of the auroral activity and can be used as an indicator the space weather conditions.

ACKNOWLEDGMENT

We thank the Institutes who maintain the IMAGE Magnetometer Array, Grant RFBR 14-05-98820 r-sever-a. and grant of RFBR 14-07-00512.

REFERENCES

[1] B. Forte, S.Radicella, "Geomtrical control of scintillation indices What happens for GPS satellites" in Radio Science, vol. 39, 2004.

[2] S.A. Chernouss, N.V., Kalitenkov, "The dependence of GPS positioning deviation on auroral activity" in International Journal of Remote Sensing, vol. 32(1), 2011, pp. 3005-3017.

[3] Shagimuratov, I.I.. Efishov, N.Yu. Tepenitsyna, "Similarities and Differences of storm time occurrence of GPS phase fluctuations at northern and southern hemispheres" in Proceeding EuCAP 2009, 2009.

[4] Shagimuratov, A. Krankowski, I.I.. Efishov, Yu.V., Cherniak, P. Wielgosz, I.E. Zakharenkova, "High latitude TEC fluctuations and irregularity oval during geomagnetic storms" in Earth Planets Space, vol. 64(6), 2012, pp. 521-529.

[5] J. Aarons, GPS system phase fluctuations at auroral latitudes, Journal of Geophysical Research, 102, A8, 1997, pp. 17219-17231.

[6] X. Pi, A.J. Manucci, U.J. Lindqwister, C.M. Ho, Monitoring of global ionosheric irregularities using the worldwide GPS network, Geophysical Research Letters, 24, 1997, pp. 2283-2286.

GUV 2511 instrument installation in Stara Zagora and first results

R. Werner[1], *B. Petkov*[2], *A. Atanassov*[1], *D. Valev*[1], *V. Guineva*[1], *E. Roumenina*[1], *A. Kirillov*[3]

[1] Space Research and Technology Institute (SRTI), BAS, Sofia, Bulgaria
[2] Institute of Atmospheric Sciences and Climate (ISAC), CNR, Bologna, Italy
[3] Polar Geophysical Institute (PGI), Apatity, Russia
E-mail: rolwer52@yahoo.co.uk

Abstract.

In February 2015 a Ground-based Ultraviolet Radiometer (GUV) 2511 was installed in Stara Zagora. The GUV 2511 instrument is designed for measurements of the downwelling global irradiances at 305, 313, 320, 340, 380, 395 nm and of the irradiance in the visible range of 400-700 nm. The instrument allows obtaining of the total column ozone (TCO) in the atmosphere, the determination of the UV-index and the retrieval of cloud optical thickness. In the paper the first results of the measurements are presented and the methodology to derive TOC is described.

Introduction

Routinely total column ozone (TCO) observations began with the design of the Dobson-spectrometer in 1924 (see Dobson, 1968). After the International Geophysical Year 1957 a global network of ground-based ozone measurements was established mainly consisting of Dobson and Brewer spectrophotometers with a typical spectral resolution of approximately 1 nm. Stamnes et al. (1991) have shown that by the help of spectrometers with high resolution of about 0.5 nm TCO and the cloud transmission can be determined very accurately. In the 90-ties broadband filter instruments were developed to increase the global coverage of the measurements. Broadband instruments with only a few filters allow also determining of the biologically UV dose, the total ozone abundances, and the cloud optical depths (Dahlbeck, 1996).In February 2015 a Ground-based Ultraviolet Radiometer (GUV) 2511 was installed in Stara Zagora. The GUV 2511 instrument is designed for measurements of the downwelling global irradiances in six broadband channels and of the irradiance in the visible range from 400 to 700 nm. The instrument allows obtaining of the total column ozone (TCO) in the atmosphere, the determination of the UV-index and the retrieval of cloud optical thickness. In the paper the first results in respect of the measurements are presented and the methodology to derive TOC is described.

Methodology of TCO determination

By GUV instruments the global, the diffuse and the direct components of the downwelling irradiation are measured. The ratio of the irradiances at different wavelengths depends on the scattering properties of the air particles and molecules and also on the solar elevation, e.g. on the absorbing path length through the atmosphere. Therefore TCO cannot be determined directly by the observed irradiance ratios as it is possible for Dobson and Brewer spectrophotometers for direct solar measurements. To determine TCO from UVA/UVB ratios simulations by radiation transfer models including the UV spectral range are necessary. Here we used Tropospheric Ultraviolet and Visible (TUV) model, version 4.1., developed by Madronich (1993), where the Rayleigh scattering parameters were calculated through an improved algorithm for standard atmospheric conditions (Thomasi et al., 2005). The spectra were calculated for the Stara Zagora location (Lat=42.4°N, Long=25.6°E, alt = 0.43 km) for different TCO from 0 up to 700 DU with a step of 20 DU and zenith angels from 20° up to 90° with a step of 1°. A ground albedo of 0.05 was used as input parameter. The obtained spectra were multiplied with the relative filter response functions, approximated by a Gaussian with 10 nm Full Width at the Half-Maximum (FWHM). The irradiance ratios for

wavelengths 340 nm and 313 nm were calculated for the mentioned above TCO and zenith angles (Stamnes table, see Fig.1). The ozone content values are determined by interpolation of the calculated tables for the measured ratios and the zenith angles for the time moments, when the measurements were performed.

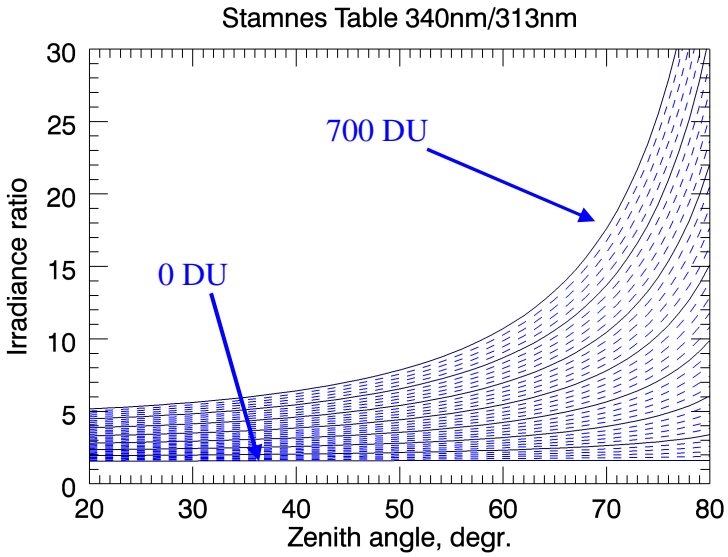

Fig.1. Calculated Stamnes table (ground albedo of 0.05) for Stara Zagora.

Brief description of GUV 2511 instrument

The GUV instrument measures the global irradiances at 305, 313, 320, 340, 380, 395 nm with a bandwidth of 10 nm FWHM as well as the Photosynthetically Available Radiation (PAR) irradiance in the visible spectral range from 400 to 700 nm. The 313 nm filter was added in the GUV 2511 type instrument unlike the previous GUV 511 type instrument to ensure ozone determinations at greater zenith angles (of about 80°) where the absorption at 305 nm is very high. The entrance instrument window consists of a teflon diffusor on a quarz base. A heater blanket placed in the instrument head stabilizes the photodiodes and filters at the temperature of 50°C. A portion of the heat is used to warm the diffuser and to keep it free from ice and snow. Melt water or rain on the diffuser and occluding ring is led outside by drain holes.

The instrument functioning is operated by a controller including the power management, the temperature control and the data transfer via the interface RS232.

The main advantage of the GUV instrument series is that they have not moving components. Moreover the measurements are carried out very fast.

GUV 2511 instrument installation

Fig.2. View of the GUV 2511 instrument on the roof of the observatory.

The GUV instrument was installed in February 2015 on the roof of the Stara Zagora observatory (Fig.2). The observatory is located at 3 km from the City Stara Zagora at an altitude of 430 m, about 250 m higher than the city. Near the observatory there aren't other high buildings, thus a free view to the sky is ensured. The instrument is connected with the computer via RS232 by a 50 m long cable. Fig.3 shows the instrument controller and the monitor displaying the measurement progress in the control room.

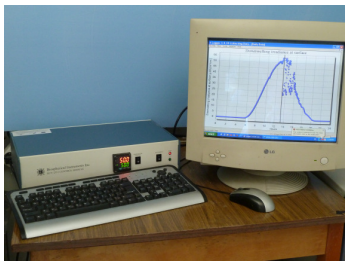

Fig.3. The instrument controller and the monitor in the control room.

Preliminary results

From February to May 2015 were carried out daily measurements with an integration time of 10 sec. with some interrupts for technical reasons. In Fig.4 an example is given

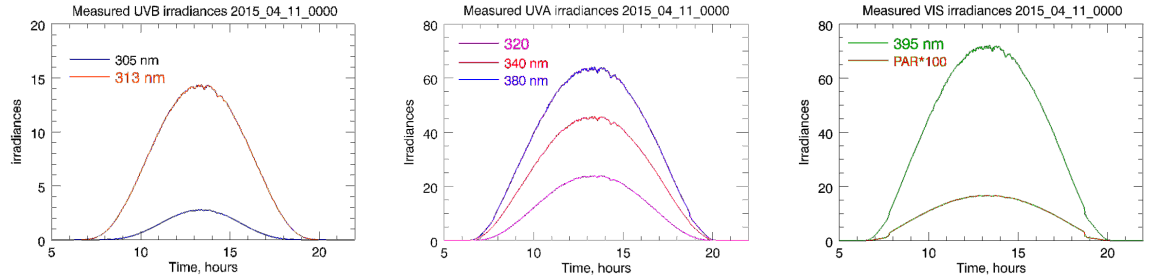

Fig.4. Measured irradiances (given in μmW/(cm^{2}nm) *by all GUV 2511 channels.*

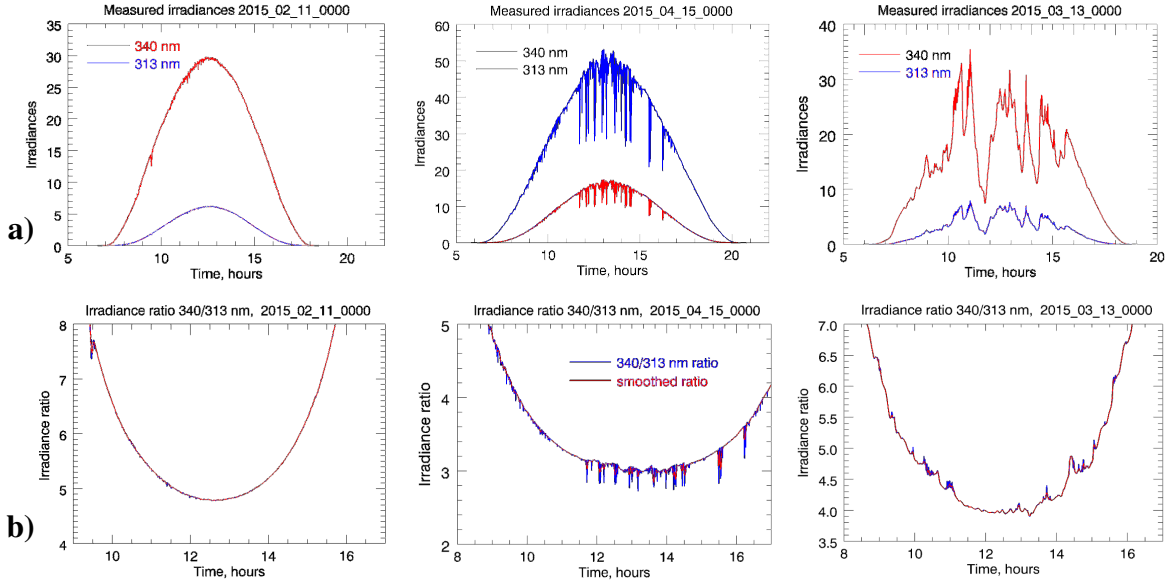

Fig.5. a) Measured irradiances, given in μmW/(cm^{2}nm)*, for days with different cloudiness and b) the irradiance rations (see text).*

for the measured irradiances in all GUV 2511 channels during a clear day (11 April 2015). The irradiance maxima are observed at noon about 12:30 Local time.

Fig.5a shows the observed irradiances during days with different cloudiness: for an almost clear day (left), for a day with fast changing of the solar disc cloud cover (middle) and for a day with large cloud fraction (right). Fig.5b presents the irradiances ratios for the same days. The obtained ratios are much more insensitive against changes of the overhead cloudiness in comparison with the observed irradiations. To reduce the cloudiness influence on the ratios even more, the ratios were additionally smoothed by a running boxcar over 13 values, e.g. over 130 sec., and the result is drawn by red lines in figures 5b.

The TCO densities for the obtained irradiance ratios retrieved by interpolation of the Stamnes table for the corresponding zenith angles are shown in Fig.6. For comparison the TOMS long time annual mean variations are shown, too (the blue line in Fig.6). It is evident, that our ozone data would be much better fitted if the TOMS data are shifted by approximately 20 DU downwards (the red line in Fig.6). Consequently our data values are about 20 DU lower. The main reason is that the location of the central filter wavelength and

the response function of the individual filters are not exactly known. However the variations of the individual daily values from the TOMS yearly mean are typical for ozone.

Conclusions

More detailed analyses about the filter choice and the determination of more accurate filter functions are necessary to improve the quality of the TCO data. The instrument has to be calibrated by the help of standard ozone spectrometers. However the preliminary results show, that in the future ozone data with high quality are to be expected for the Stara Zagora location.

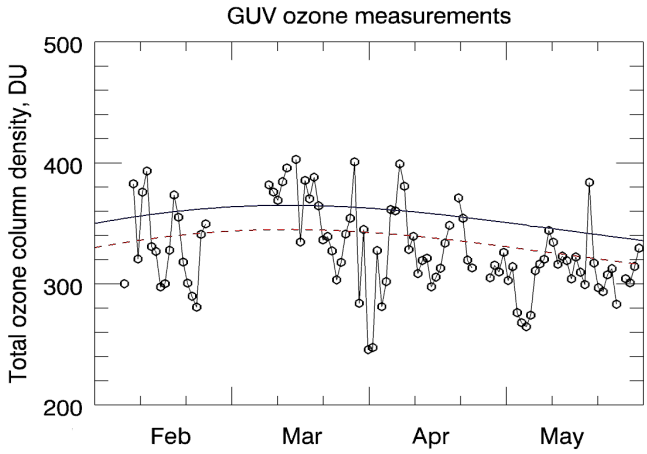

Fig.6. TCO for Stara Zagora determined for the observation period February-May 2015 (black line) and the TOMS annual means (thick and dashed line, see text).

Acknowledgements

The GUV instrument was provided by the project BG161PO003-1.2.04-0053 "Information Complex for Aerospace Monitoring of the Environment" (ICASME) implemented with the financial support of Operational Programme„Development of the Competitiveness of the Bulgarian Economy 2007-2013", co-financed by the European Regional Development Fund and the national budget of the Republic of Bulgaria

References

Dobson, G. M. B., Forty Years' Research on Atmospheric Ozone at Oxford: A History, Appl.Optics, 7(3), 387-405, 1968.

Stamnes, K., Slusser, J., Bowen, M., Derivation of total ozone abundances and cloud effects from spectral irradiance measurements, Appl. Optics, 30(30), 4418-4426, 1991.

Dahlbeck, A., Measurements of biologically effective UV doses, total ozone, and cloud effects with multichannel, moderate bandwidth filter instruments, Appl. Optics, 35(33), 6514-6521, 1996.

Madronich, S., UV radiation in the natural and perturbed atmosphere, in Environmental Effects of UV (Ultraviolet) Radiation, M. Tevini, ed., Lewis, Boca Raton,, 17–69, 1993.

Tomasi, C., Vitale, V., Petkov, B., Lupi, A., Cacciari, A., Improved algorithm for calculations of Rayleigh-scattering optical depth in standard atmospheres, Appl. Opt., 44**,** 3320–3341, 2005.

Petkov, B., Vitale, V., Tomasi, C., Bonafé, U., Scaglione, S., Flori, D., Santaguida, R., Gausa, M., Hansen, G., Colombo T., Narrowband filter radiometer for ground-based measurements of global ultraviolet solar irradiance and total ozone, Appl. Optics, 45(18), 4383-4395, 1996.